

# **Defects and Diffusion in Colloidal Crystals**

---

**Cover:** Simulation snapshot of a two-dimensional polycrystal before (front) and after (back) a small fraction of the particles has been made active for a while. Particles are color-coded according to their local orientation.

PhD thesis, Utrecht University, the Netherlands, September 2018.

ISBN: 978-90-393-7041-4

A digital version of this thesis is available at <http://www.colloid.nl/>

# Defects and Diffusion in Colloidal Crystals

---

## Defecten en Diffusie in Colloïdale Kristallen

(met een samenvatting in het Nederlands)

### Proefschrift

ter verkrijging van de graad van doctor aan de Universiteit Utrecht op gezag van de rector magnificus, prof. dr. H.R.B.M. Kummeling, ingevolge het besluit van het college voor promoties in het openbaar te verdedigen op woensdag 19 september 2018 des ochtends te 10.30 uur

door

Berend van der Meer

geboren op 17 februari 1991 te Veenendaal.

**Promotor:** Prof. dr. ir. M. Dijkstra  
**Copromotor:** Dr. L.C. Filion

# Contents

<b>1</b>	<b>Introduction</b>	<b>1</b>
1.1	Colloids	1
1.2	Colloidal phase behavior	1
1.3	Colloidal crystals and defects	2
1.4	Hard particles: a simple model system	3
1.5	Active colloids	5
1.6	Computer simulations	6
1.6.1	Monte Carlo simulations	6
1.6.2	Dynamics simulations	7
1.7	Thesis outline	9
<b>2</b>	<b>Diffusion and interactions of point defects in hard-sphere crystals</b>	<b>11</b>
2.1	Introduction	12
2.2	Model and Methods	12
2.2.1	Simulation details	12
2.2.2	Defect tracking	13
2.2.3	Initialization of point defects	13
2.3	Results	13
2.3.1	Diffusion coefficients of vacancies and interstitials	13
2.3.2	Free-energy barrier for vacancy diffusion	14
2.3.3	Interactions between point defects	16
2.3.4	Displacement field of point defects	17
2.4	Discussion and Conclusions	19
2.5	Acknowledgements	20
<b>3</b>	<b>Diffusion and interactions of interstitials in hard-sphere interstitial solid solutions</b>	<b>21</b>
3.1	Introduction	22
3.2	Model and Methods	23
3.3	Results	23
3.3.1	Diffusion of interstitial particles	23
3.3.2	Interactions between interstitials	33
3.3.3	Empirical relationship between the large-particle fluctuations and interstitial diffusivity	35
3.4	Discussion and Conclusions	36
3.5	Acknowledgements	38

<b>4</b>	<b>Antisite defects induce non-stoichiometry in the hard-sphere colloidal Laves phase</b>	<b>39</b>
4.1	Introduction	40
4.2	Model and Methods	41
4.2.1	Free energy of the MgZn <sub>2</sub> Laves phase	41
4.2.2	Free energy of the FCC crystals	42
4.2.3	Measuring the free energy associated with single defects	43
4.3	Results	45
4.4	Discussion and Conclusions	51
4.5	Acknowledgements	52
<b>5</b>	<b>Revealing a vacancy analogue of the crowdion interstitial in simple cubic crystals</b>	<b>53</b>
5.1	Introduction	54
5.2	Model and Methods	55
5.2.1	Simulation details	55
5.2.2	The tracking algorithm	55
5.3	Results	56
5.3.1	Particle displacements associated with point defects	56
5.3.2	Interactions between vacancies	60
5.3.3	Diffusion of vacancies	61
5.3.4	“Voidions” for a system with soft repulsive isotropic interactions	63
5.4	Discussion and Conclusions	64
5.5	Acknowledgements	64
<b>6</b>	<b>Formation of large two-dimensional single colloidal crystals by doping with active particles</b>	<b>65</b>
6.1	Introduction	66
6.2	Model and Methods	66
6.3	Results	69
6.4	Discussion and Conclusions	76
6.5	Acknowledgements	77
<b>7</b>	<b>Removing grain boundaries from three-dimensional colloidal crystals using active dopants</b>	<b>79</b>
7.1	Introduction	80
7.2	Model and Methods	80
7.2.1	Model	80
7.2.2	Formation of initial polycrystals	81
7.2.3	Fluid-crystal coexistence simulations	81
7.2.4	Cluster algorithm	82
7.3	Results	82
7.4	Discussion and Conclusions	88
7.5	Acknowledgements	89

<b>8 Predicting phase behaviour of mixtures of active spherical particles</b>	<b>91</b>
8.1 Introduction	92
8.2 Model and Methods	93
8.2.1 Model systems	93
8.2.2 Dynamics	94
8.2.3 The normal component of the local pressure tensor	94
8.2.4 Reservoir simulations	96
8.3 Results	98
8.3.1 Lennard-Jones active-passive mixture	98
8.3.2 Weeks-Chandler-Andersen active-active mixture	101
8.4 Discussion and Conclusions	105
8.5 Acknowledgements	106
<b>References</b>	<b>107</b>
<b>Summary</b>	<b>119</b>
<b>Samenvatting</b>	<b>123</b>
<b>Acknowledgements</b>	<b>127</b>
<b>About the author</b>	<b>129</b>
<b>List of Publications</b>	<b>130</b>



## Introduction

---

### 1.1 Colloids

Colloids are microscopic particles whose size ranges from a nanometer to several micrometers, that are dispersed in a solvent. We make use of colloids on a daily basis. For example butter, mayonnaise, toothpaste, latex paint, etc., all consist of colloidal particles. One striking characteristic of colloidal systems is that their constituent particles are in a constant state of random motion. This phenomenon is known as Brownian motion, and was named after Robert Brown who observed a random jiggling motion in 1827 while studying plant pollen suspended in water under his microscope [1]. He repeated the experiments with inorganic particles and observed the same vivid motions at which point he concluded that the motions were not induced by some life-giving force. Brown thus showed these random motions to be a general property of particles with microscopic dimensions that are suspended in a liquid. Unfortunately, he could not provide an explanation for the phenomenon he had observed.

Many decades later, in the early 20th century, Albert Einstein and William Sutherland would both, independently, provide a quantitative theory that explained Brownian motion [2, 3]. Specifically, they showed that the Brownian motion of colloidal particles could arise from incessant collisions with the fast-moving molecules of the solvent. Note that during this time the existence of atoms and molecules was still highly debated. In the years to follow, Jean Perrin studied experimentally the Brownian motion of colloidal particles in greater detail, allowing him to examine the expressions derived by Einstein and Sutherland [4, 5]. Perrin's experimental work on colloids contributed significantly to ending the scepticism about the existence of atoms and molecules, for which he was awarded the Nobel Prize in Physics in 1926.

### 1.2 Colloidal phase behavior

Due to their Brownian motion, colloids can spontaneously explore all space available to them, and as such they obey the laws of equilibrium statistical physics. As a consequence, colloids can self-assemble, i.e. organize themselves, into a wide range of phases, such as

gases, liquids, crystals, and even quasicrystals – just like atoms and molecules. Hence, to some extent colloids can be regarded as “big atoms” [6, 7].

As in atomic and molecular systems, the phase behaviour of a colloidal system is largely determined by the nature of the interactions between the particles. Recent advances in colloidal synthesis allow experimentalists to tune these interactions ever more precisely. Studying the phase behavior of these novel colloidal systems has two main purposes. First of all, by finely tuning the properties of the colloidal building blocks, one can tune, not only the functionality of the particle, but also the structure of the (crystal) phase they form. Such “programmable” particles with tailor-made interactions, are considered highly important for the development of advanced functional materials, where the complete structure of the material, from the atomic scale to the macroscale, will be important for its functioning. Secondly, and more along the lines of this thesis, colloidal systems can be directly observed on the single particle level in both real space and real time using microscopy. As a result, colloidal systems provide an ideal platform to address a range of fundamental questions about the nature of liquids, crystals and glasses.

### 1.3 Colloidal crystals and defects

In this thesis we will focus on crystalline phases formed by colloids, often referred to as “colloidal crystals”, and in particular on their crystallographic defects. Colloidal crystals are ordered, self-assembled solids comprised of colloidal particles that are arranged on a periodic lattice. The simplest repeating unit in the crystal is called a unit cell. Hence, this unit cell captures both the symmetry and structure of the lattice. However, real crystals almost always contain defects or irregularities from those ideal arrangements.

Even when the concentrations of these defects are low, they can significantly alter the mechanical and transport properties of the crystal. For example, even though particles in a crystal phase are typically orders of magnitude less mobile than those in a fluid, diffusion is still possible via the diffusion of defects, such as vacancies and interstitials. Therefore, understanding the motion of these defects is key to understanding transport processes in crystals, including particle hopping and other local rearrangements. Also, the mechanical response of crystalline solids is largely governed by the presence and diffusion of defects in the crystal lattice. Hence, understanding the formation and motions of these defects is essential to understanding mechanical instabilities such as creep, fracture and yielding.

The simplest type of crystal defect is a point defect [8, 9]. These defects are essentially restricted to a single lattice site and are zero-dimensional, which is to say that they have a finite extent in all three dimensions. Examples of point defects are vacancies, interstitials, and antisite defects. A vacancy can be created by removing a single particle from the lattice, thus leaving behind an empty lattice site [Figure 1.1(a)]. Alternatively, an interstitial can be created through adding an extra particle to the lattice [Figure 1.1(b)]. Note that this often involves significant distortions of the local lattice, as indicated by the lines in Figure 1.1(b). Diffusion processes within a crystalline solid typically involve these point defects. Namely, the diffusion of these defects inside the lattice allows particles to explore new lattice sites over time. Another type of point defect, specific to multicomponent crystals, are antisite defects. These occur when a particle of one species

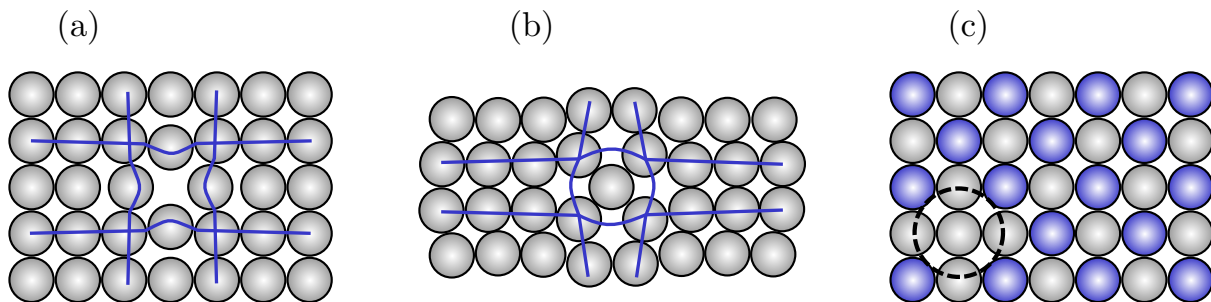


**Figure 1.1:** Schematic of different types of point defects. (a) A vacancy is created by removing a particle from the lattice. The particles in the vicinity of the vacancy center may relax a bit towards the center of the vacancy (blue lines). (b) An interstitial is created by adding an extra particle to the lattice. Interstitials typically generate significant distortions inside the lattice (blue lines). (c) In a binary crystal, an antisite defect is created by putting a particle of one species on a lattice site that is supposed to be occupied by a particle of the other species.

sits on a lattice site that is usually occupied by a particle of a different species. An example is shown in Figure 1.1(c).

More complicated defects that are extended in more than zero dimensions are also possible. Linear defects, often referred to as dislocations, are lines along which the regular ordering of particles changes abruptly [Figure 1.2]. The concept of a dislocation was “invented” in 1934, before their actual observation, by Taylor [10], Orowan [11] and Polanyi [12], in an attempt to explain the softness of metals [13, 14]. Namely, metals already start to deform plastically when subjected to forces much smaller than the cohesive forces responsible for holding the metal atoms together. These dislocations would only be observed experimentally many years after they were hypothesized to exist; first in bubble rafts [15], and later also directly in metals using electron microscopy techniques [16–18].

Yet another type of defect is a grain boundary. These are planar defects that correspond to the interface between crystal domains with different crystallographic orientations [Figure 1.2]. Real-life crystals are almost always polycrystalline in nature, which is to say that they consist of many crystal domains of different crystallographic orientations put together. The presence of these grain boundaries is well known to drastically alter the material properties compared to a single crystal, for instance increasing the hardness in metals [19–22].

## 1.4 Hard particles: a simple model system

In the last decades, colloidal hard-sphere suspensions have emerged as an archetypical model system for simple liquids and solids. Specifically, for two spherical particles of diameter  $\sigma$  the hard-core interaction potential is given by:

$$\beta U_{HS}(r) = \begin{cases} \infty, & r < \sigma \\ 0, & r \geq \sigma \end{cases}, \quad (1.1)$$

where  $r = |\mathbf{r}_i - \mathbf{r}_j|$  is the separation distance between two particles at positions  $\mathbf{r}_i$  and  $\mathbf{r}_j$ , respectively. This hard-core repulsion mimics the step repulsive interaction that

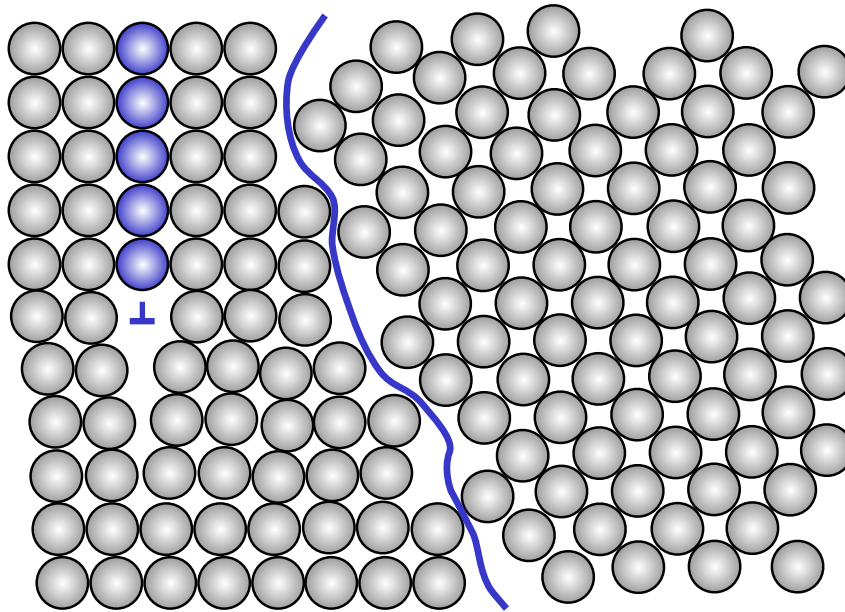


**Figure 1.2:** Schematic cross-section of a three-dimensional simple cubic crystal, showing a dislocation and a grain boundary. The dislocation is created by inserting a half-plane of particles (blue) inside the lattice. The grain boundary (blue line) corresponds to the interface between crystal domains of different crystallographic orientations.

molecules and atoms experience at very close separation distances. Importantly, hard particles are not a purely hypothetical system used in theory and simulations only, but can also be realized in experiments using colloids. For example, such hard-core interactions can be reasonably well achieved experimentally by using sterically stabilized poly(methyl methacrylate) particles that are dispersed in an apolar, index-matched solvent [23].

By definition, for these hard-particle systems only non-overlapping configurations are possible, as creating an overlap would require an infinite amount of energy. Hence, the temperature is not a relevant thermodynamic variable in hard-particle model systems – the total potential energy of the system is by definition always zero. As a result, these systems are purely driven by entropy.

In 1957, computer simulations examined the phase behaviour of hard spheres, and, somewhat surprisingly, found a phase transition from a fluid phase to a crystal phase [24, 25]. This appearance of a crystal phase was somewhat controversial at this time, as it was debated whether purely repulsive particles could form a stable crystal, or whether attractions were necessary (see e.g. Ref. [26]). Nowadays, we know that monodisperse hard spheres undergo a first-order phase transition from a disordered fluid phase to a face-centered-cubic crystal phase at high enough packing fractions [27]. The phase diagram has also been confirmed by experiments, revealing a fluid phase, a fluid-crystal coexistence, a crystal phase, and a glassy phase, as a function of the packing fraction [23].

More complex phase behavior of hard spheres can be obtained by mixing particles of different sizes [28–53]. For example, when hard spheres of two different sizes are mixed together they may spontaneously undergo an entropy-driven crystallization process into a

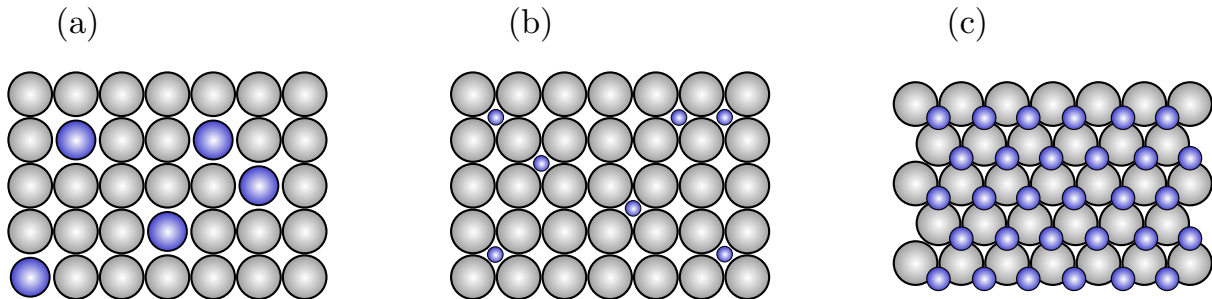


**Figure 1.3:** Schematic of different crystalline behaviors observed for binary mixtures of hard spheres. (a) Substitutional solid solutions occur for size ratios close to unity. Because the particles of the two species are so similar in size, they are commensurate with each other and share the same underlying lattice. (b) Interstitial solid solutions occur for small size ratios. Due to the large size-disparity, the small particles can be accommodated in the interstices of the host lattice of large particles. (c) Binary crystals occur for intermediate size ratios. In this case both species have their own sub-lattice.

binary crystal. More specifically, by tuning the size ratio and the overall composition of the system, several ordered crystal phases can be achieved with structures often analogous to those found in the atomic realm. Roughly speaking, these mixtures exhibit three different crystalline behaviors depending on the size ratio  $q = \sigma_a/\sigma_b$  of the diameters  $\sigma_{a,b}$  of the two species. For particles of similar size, i.e. a size ratio of  $q \gtrsim 0.85$ , a thermodynamically-stable substitutional solid solution forms with the two species sharing the same host lattice [34–40]. As such, the species of which the fewest particles are present can be thought of as substituting for a particle of the other species [Figure 1.3(a)]. For particles of dissimilar size, i.e. a size ratio of  $q \lesssim 0.4$ , a thermodynamically-stable interstitial solid solution forms with the small particle being located in the interstices of the host lattice of large particles [41, 42], as shown schematically in Figure 1.3(b). For particles of intermediate size ratios  $0.3 \lesssim q \lesssim 0.85$ , several binary crystal structures can be achieved [43–53], where both species are sitting on their own sub-lattice [Figure 1.3(c)].

More recently, it has become experimentally possible to synthesize a wide variety of hard particles with novel, anisotropic shapes. Examples include dumbbells [54], rods [55, 56], platelets [57–59], superballs [60], etc. These particles can self-assemble into a wide array of new crystal structures, and as such hold a big promise for materials science. Computer simulations have proven to be especially useful in mapping out the phase behavior of these systems (see e.g. [61–63]).

## 1.5 Active colloids

While all the colloidal systems described previously obey the laws of classical statistical physics, more recently a new class of colloids was introduced, so called “active colloids” [64–69]. The key feature of these active colloidal systems is that its constituent particles incessantly convert energy into self-propulsion. Due to this constant input of energy, these systems are inherently out-of-equilibrium and cannot be described by equilibrium statistical physics. Specifically, apart from Brownian motion, these particle un-

dergo an autonomous swimming motion. As a result, these systems exhibit a wealth of new phase behaviour, including, for example, motility-induced phase separation into dense and dilute phases [67–78], giant density fluctuations [79, 80], and swarming [81]. As traditionally such particles occurred solely within the purview of natural systems (e.g. bacteria), synthetic active colloids have attracted significant interest as a model for active biological matter. Additionally, they have a promising prospect in term of possible applications, including cargo-delivery [82–84], water treatment [85], and as building blocks for new materials [86].

## 1.6 Computer simulations

In this thesis we will investigate colloidal systems using various computer simulation techniques [87, 88]. Specifically, three methods are used: Monte Carlo simulations, molecular dynamics simulations, and Brownian dynamics simulations. In the following we briefly describe these three methods.

### 1.6.1 Monte Carlo simulations

Monte Carlo simulations provide an efficient way to study the equilibrium phase behavior of colloidal suspensions. In this method, the goal is not to approximate realistic dynamics, but rather to construct a large set of particle configurations according to their equilibrium distribution. For instance, for a simulation where the number of particles  $N$ , volume  $V$  and temperature  $T$  are kept constant, commonly referred to as the  $NVT$ -ensemble, a Monte Carlo simulation creates a set of configurations according to the Boltzmann distribution. In this ensemble, the probability that the system is in a configuration with particle positions  $\mathbf{r}^N$  and its corresponding energy  $U(\mathbf{r}^N)$  is given by

$$P(\mathbf{r}^N) = \frac{\exp(-\beta U(\mathbf{r}^N))}{Q}, \quad (1.2)$$

where  $\beta = 1/k_B T$  with  $k_B$  Boltzmann's constant, and

$$Q = \int d\mathbf{r}^N \exp(-\beta U(\mathbf{r}^N)). \quad (1.3)$$

Using this probability distribution function, the average value of a measurable quantity  $A$  is given by

$$\langle A \rangle = \int d\mathbf{r}^N A(\mathbf{r}^N) P(\mathbf{r}^N). \quad (1.4)$$

As a Monte Carlo simulation by definition generates configurations that are correctly weighted, i.e. with probability  $P(\mathbf{r}^N)$ , one can simply average the quantity  $A$  over many configurations. Hence, in this case the average value is given by

$$\langle A \rangle = \frac{1}{M} \sum_{k=1}^M A(\mathbf{r}^N), \quad (1.5)$$

with  $M$  the number of configurations.

In Monte Carlo simulations these configurations are generated via a Markov process, i.e. a process of constructing a new configuration from the current configuration without any history dependence. In the  $NVT$ -ensemble this is generally done as follows. A new trial configuration is obtained by moving a randomly selected particle by a small, random amount. Following an appropriate acceptance rule, the trial configuration is either accepted or rejected. If accepted, it becomes the next configuration in the chain. Otherwise, the old configuration is used again as the next configuration in the Markov chain. Note that as the acceptance rule is probabilistic in nature, the resulting chain is not deterministic.

In principle, Monte Carlo simulations are extremely versatile, and can be developed to incorporate a wide variety of different degrees of freedom. For instance, if particles are anisotropic, then in addition to their positions, one also needs to consider the orientations of the particles. In this case, additional Monte Carlo moves will have to be incorporated that allow for particle rotation. One can also adapt the Monte Carlo simulations to other ensembles. These simulations can then involve, for example, volume changes, particle-insertion moves, particle-deletion moves, and particle-swap moves that exchange the positions between particles.

Hence the Monte Carlo method is extremely flexible. However, due to the absence of realistic underlying dynamics this method is only suitable for investigating static quantities.

## 1.6.2 Dynamics simulations

The equations of motion for a colloidal system in principle must include equations for both the colloids and the solvent. However, treating the equations of motions for both the colloids and the solvent would be extremely computationally expensive, as there are *many* solvent molecules for each colloid, and they move on much shorter time scales. Hence, a common approximation is to coarse grain out the solvent, i.e. to treat the solvent “implicitly”. In the following we describe two methods where the solvent is being described implicitly.

### Brownian dynamics simulations

If we assume no hydrodynamic interactions between the colloids, then the solvent has two important effects on the dynamics of the colloidal particles. First, as Brown first noticed under his microscope, the solvent molecules exert random forces on the colloid due to collisions. In Brownian dynamics simulations, this is incorporated as a stochastic noise term. Second, the fluid induces a drag force, which is taken to be proportional to the velocity of the colloid. This results in the well known Langevin equation [89], which is given by

$$m \frac{d^2 \mathbf{r}_i}{dt^2} = - \sum_{j \neq i} \frac{\partial U(\mathbf{r}_{ij})}{\partial \mathbf{r}_{ij}} - \eta \frac{d\mathbf{r}_i}{dt} + \sqrt{2\eta k_B T} \boldsymbol{\xi}_i, \quad (1.6)$$

where  $\mathbf{r}_i$  is the position of particle  $i$ ,  $m$  is the particle’s mass,  $U(r)$  is the pairwise potential between particles with  $r$  the separation distance,  $\eta$  is the damping coefficient, and  $\boldsymbol{\xi}_i$  is a

random vector with zero mean and unit variance

$$\langle \boldsymbol{\xi}_i(t) \rangle = 0, \quad (1.7)$$

$$\langle \boldsymbol{\xi}_i(t) \boldsymbol{\xi}_j(t') \rangle = \mathbb{I} \delta_{ij} \delta(t - t'), \quad (1.8)$$

with  $\mathbb{I}$  the identity matrix. The three terms at the right-hand side of Equation 1.6 correspond to the force due to inter-particle interactions, the drag force, and the stochastic Brownian force, respectively.

For a typical colloidal system, particles move at a so-called low Reynold number, which is to say that viscous forces dominate over inertial effects. Hence, a common approximation is to consider a colloidal system to be inertia-free. This allows us to simplify Equation 1.6 and write down the equation of motion most often used in Brownian dynamics simulations

$$\frac{d\mathbf{r}_i}{dt} = -\frac{D_0}{k_B T} \sum_{j \neq i} \frac{\partial U(\mathbf{r}_{ij})}{\partial \mathbf{r}_{ij}} + \sqrt{2D_0} \boldsymbol{\xi}_i, \quad (1.9)$$

where  $D_0 = k_B T / \eta$  is the translational diffusion coefficient. Specifically, this equation of motion corresponds to the overdamped limit of the Langevin equation, also commonly referred to as the overdamped Langevin equation. This equation of motion can be numerically integrated using a stochastic variant of the standard Euler scheme, namely the the Euler-Maruyama method [90].

## Molecular dynamics simulations

A further approximation is to remove even the stochastic noise and drag due to the solvent. In this case, one is left with Newton's equations of motion for the colloids. Note that as the static properties do not depend on the dynamics, such simulations can safely be used to measure them. Additionally, the stochastic noise and friction are most important at short time scales, thus the molecular dynamics method can also be used to explore long time dynamical behaviour.

The basic idea in a molecular dynamics simulation is to numerically evolve a system according to Newton's equations of motion. In the case where the interactions between the particles are described by a continuous potential, then the numerical solutions generally move the system from one state to another in discrete time steps  $\delta t$ . There are many different algorithms which are used to do this, but the most common is the so-called Verlet algorithm, which is accurate to order  $O(\delta t^4)$ . However, such time-driven schemes run into problems when working with discontinuous potentials, such as in the case of hard particles. In systems with hard potentials, the particles move ballistically until two particles collide. Such collisions are instantaneous, but the time between collisions is clearly not fixed. Hence, if one were to use a finite fixed time step to integrate the equations of motion, instead of changing direction when the two particles collide, they would end up overlapping - which should not be possible for hard particles. A simple way to solve this issue is to make use of a collision-by-collision approach [91, 92]. This method is commonly referred to as event-driven molecular dynamics. In such event-driven simulations the times of all possible collisions are calculated, and the system is evolved to exactly the next collision event, so that it can be handled correctly.

## 1.7 Thesis outline

The chapters in this thesis are organized as follows. We will start off in Chapter 2 by looking into the diffusion and interactions of the simplest of defects, namely vacancies and interstitials, in arguably the simplest model system: monodisperse hard spheres. In Chapters 3 and 4 we will look at binary mixtures of hard spheres. In Chapter 3, we will investigate the diffusion and interactions of small interstitial particles in a hard-sphere interstitial solid solution. Specifically, we show how transition state theory can be used to accurately predict diffusion rates in these systems. In Chapter 4, we will investigate the role of defects in the colloidal Laves phase. We find a high equilibrium concentration of antisite defects to be present in the Laves phase, thus shedding new light on its self-assembly. In Chapter 5, we study vacancies in a variety of repulsive systems forming simple cubic crystals. In particular, we show that for all these systems the vacancies are “delocalized” along a row of particles, suggesting this to be an inherent feature of simple cubic crystals of repulsive particles. In Chapters 6 – 8, we will be mixing passive and active colloids. In Chapters 6 and 7, we show that active particles can provide an elegant new route to removing grain boundaries in polycrystals, in two and three dimensions, respectively. Chapter 8 focusses on a fundamental question: is it possible to predict quantitatively whether two phases of active particles coexist? We show that for a torque-free active system the phase diagram can be predicted by measuring the pressure and a chemical potential-like variable.



---

## Diffusion and interactions of point defects in hard-sphere crystals

---

Using computer simulations we study the diffusion, interactions, and strain fields of point defects in a face-centered-cubic crystal of hard spheres. We show that the vacancy diffusion decreases rapidly as the density is increased, while the interstitial diffusion exhibits a much weaker density-dependence. Additionally, we predict the free-energy barriers associated with vacancy hopping and find that the increasing height of the free-energy barrier is solely responsible for the slowing down of vacancy diffusion. Moreover, we find that the shape of the barriers is independent of the density. The interactions between vacancies are shown to be weakly attractive and short-ranged, while the interactions between interstitials are found to be strongly attractive and are felt over long distances. As such, we find that vacancies do not form vacancy-clusters, while interstitials do form long-lived interstitial-clusters. Considering the strain field of vacancies and interstitials, we argue that vacancies hardly feel each other, as they do not substantially perturb the crystal, and as such exhibit weak interactions. Two interstitials, on the other hand, interact with each other over long distances, and start to interact (attractively) when their strain fields start to overlap.

## 2.1 Introduction

Defects are thermodynamically bound to occur in any crystal at finite temperature. These defects play an important role in the mechanical and transport properties of crystals, and are a crucial factor for mechanical instabilities such as creep, yield, and fracture [10–12, 93]. The key aspects that underlie these phenomena are the concentrations at which these defects occur, their mobility, and their mutual interactions.

The hard-sphere model system is one of the most extensively investigated systems and has strongly contributed to a basic understanding of a variety of fundamental phenomena in condensed matter physics, such as glass transitions [94–96], crystal nucleation [97–102], and optimal packings [103–106]. Likewise, hard spheres provide a simple model system to study crystal defects, both in statistical mechanical theories [107–110], as well as in experiments using “colloidal” hard spheres [111–116]. While these experiments on colloidal particles allow for direct quantitative studies of crystals in real space and real time, studying their defects is typically very challenging. Therefore, computer simulations have proven to be very useful. The first studies of point defects in hard spheres date back to the early 1970s by Bennett and Alder [117]. Using computer simulations they estimated a relatively high vacancy concentration close to melting ( $\sim 10^{-4}$ ). Moreover, they showed that the concentrations of higher-order vacancies, such as di-vacancies and tri-vacancies, are significantly smaller than those of mono-vacancies. Almost three decades later, Pronk and Frenkel calculated the equilibrium concentrations of both vacancies and interstitials, even for polydisperse systems [107, 108]. More recently, Lechner provided a method to calculate the effective interactions between point defects in two-dimensional crystals, which were shown to be attractive in a system of soft, dipolar spheres [118, 119]. Yet, so far a detailed understanding of the dynamics and mutual interactions of point defects in hard-sphere crystals is lacking.

In this Chapter, we study the diffusion, interactions, and strain fields of point defects in a face-centered-cubic hard-sphere crystal. We show that the vacancy diffusion decreases rapidly as the density is increased, while the interstitial diffusion exhibits a much weaker density dependence. The interactions between vacancies are shown to be weakly attractive and short-ranged. As such, di-vacancies are found to be unstable and break up easily into two separate mono-vacancies, which may occasionally reform into a di-vacancy. The interactions between interstitials, however, are found to be strongly attractive and are felt over long distances. As such, we find that interstitials form stable interstitial clusters, which only sporadically manage to dissociate into separate mono-interstitials. These point defect interactions can be understood through considering the strain field of vacancies and interstitials.

## 2.2 Model and Methods

### 2.2.1 Simulation details

We investigate face-centered-cubic crystals of  $N_L$  lattice sites and  $N$  hard spheres of diameter  $\sigma$  using event-driven molecular dynamics (EDMD) simulations. We express the density in terms of the number of lattice sites per unit volume, i.e.  $\rho = N_L/V$  with  $V$  the

volume of the simulation box. Note that in these reduced units the coexistence densities are  $\rho_s\sigma^3 = 1.0372$  for the solid and  $\rho_f\sigma^3 = 0.9387$  for the fluid [120]. We define the EDMD unit time as  $\tau = \sqrt{\beta m \sigma^2}$ , where  $m$  is the mass of a particle, and  $\beta = 1/k_B T$  with  $k_B$  Boltzmann's constant and  $T$  the temperature.

For the calculations of the free-energy barrier associated with vacancy diffusion, and the calculations of the vacancy-vacancy interactions we have also employed Monte Carlo (MC) simulations. For the latter, the incorporation of ‘‘hopping’’ moves allows for more efficient sampling of all separation distances at high densities. More specifically, apart from regular translational moves of particles, we also allow a particle to move an integer number of lattice spacings, thus greatly enhancing the probability that a particle will jump into the vacancy.

## 2.2.2 Defect tracking

We locate vacancies and interstitials in the crystal using algorithms similar to those mentioned in Refs. [107, 118]. Namely, we assign each particle to its closest lattice site and check the occupancy of each lattice point. If there are no particles assigned to a given lattice point  $\mathbf{R}$ , it corresponds to a vacancy defect. We define the vacancy position to be equal to the position of the empty lattice site:  $\mathbf{r}_{\text{vac}}(t) = \mathbf{R}$ . If there are two particles assigned to a given lattice point, it corresponds to an interstitial defect. In this case, we calculate for both particles the distance to the lattice point and define the interstitial position to be equal to the position  $\mathbf{r}_i$  of the particle  $i$  that is furthest away from the lattice point:  $\mathbf{r}_{\text{int}}(t) = \mathbf{r}_i$ . Note that during the simulation we correct for the center of mass drift of the system, as described in Ref [121].

## 2.2.3 Initialization of point defects

In all simulations we start from a lattice in which we have introduced the desired number of vacancies or interstitials. Vacancies are initialized by simply removing random particles from an otherwise perfect crystal. The introduction of interstitials, on the other hand, can be a bit more involved at high densities. To this end, we start from a low density crystal, in which the interstitials can be introduced without creating overlaps, and compress it to the desired density. This is accomplished using standard  $NPT$  MC simulations, in which the number of particles  $N$ , the pressure  $P$ , and the temperature  $T$  are kept constant.

## 2.3 Results

### 2.3.1 Diffusion coefficients of vacancies and interstitials

We begin by examining the diffusion of vacancies and interstitials. To this end, we introduce either one vacancy or one interstitial in the crystal, and follow the diffusion of the point defect using the tracking algorithm described in Section 2.2.2. From these trajectories we calculate the diffusion constant of the defect from the long-term diffusive

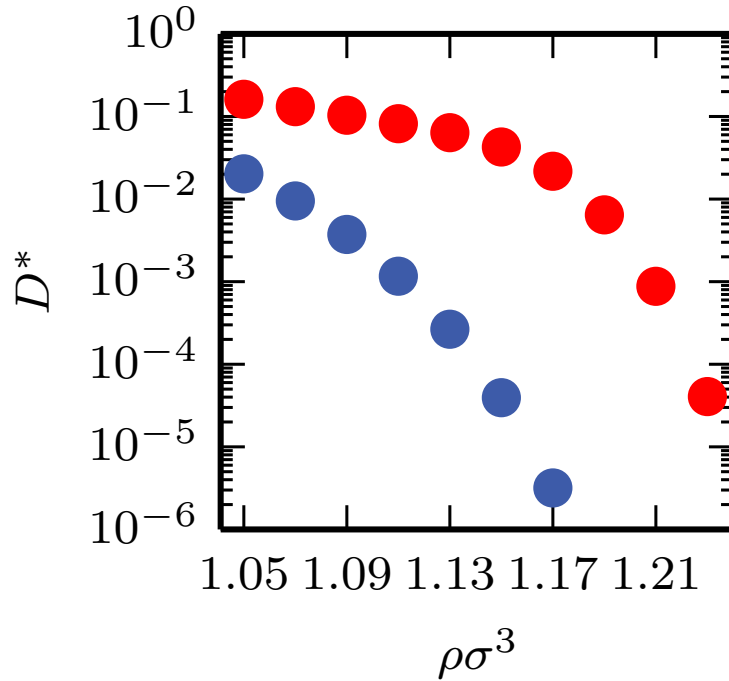


**Figure 2.1:** Vacancy (blue) and interstitial (red) diffusion constants  $D^*$  as a function of the density  $\rho$ . The diffusion constants were rendered dimensionless using  $D^* = D\tau\sigma^{-2}$ .

behaviour of the mean square displacement:

$$D = \lim_{t \rightarrow \infty} \frac{\langle \Delta r^2(t) \rangle}{6t}, \quad (2.1)$$

where  $\Delta r^2(t) = |\mathbf{r}(t) - \mathbf{r}(0)|^2$  with  $\mathbf{r}(t)$  the position of the defect at time  $t$ . We plot the diffusion constants for vacancies and interstitials as a function of density in Figure 2.1. For vacancies, we find that diffusion goes down rapidly with the density  $\rho$ , in agreement with the early results by Bennett and Alder [117]. This is understandable as in order for the vacancy to diffuse, a neighbouring particle has to hop inside of it, which becomes increasingly more difficult at higher densities. In contrast, for interstitials we observe a weak density-dependence on the mobility for densities  $\rho\sigma^3 \lesssim 1.17$ , and only observe a more drastic slowing down at very high densities  $\rho\sigma^3 \gtrsim 1.19$ . These data thus show that the slowing down of vacancies and interstitials are fundamentally different from each other and do not follow the same trend. We also observe that interstitial diffusion is always faster than vacancy diffusion,  $D_i(\rho) > D_v(\rho)$ . Thus, there is a density window where we expect vacancies to be essentially immobile while interstitials are still mobile.

### 2.3.2 Free-energy barrier for vacancy diffusion

To better understand the rapid slowing down of vacancy diffusion with increasing density  $\rho$ , we calculate the free-energy barrier associated with vacancy hopping. More specifically, we introduce a single vacancy in the crystal and constrain all but one particle to their own lattice point. This one particular particle is allowed to hop between its own lattice

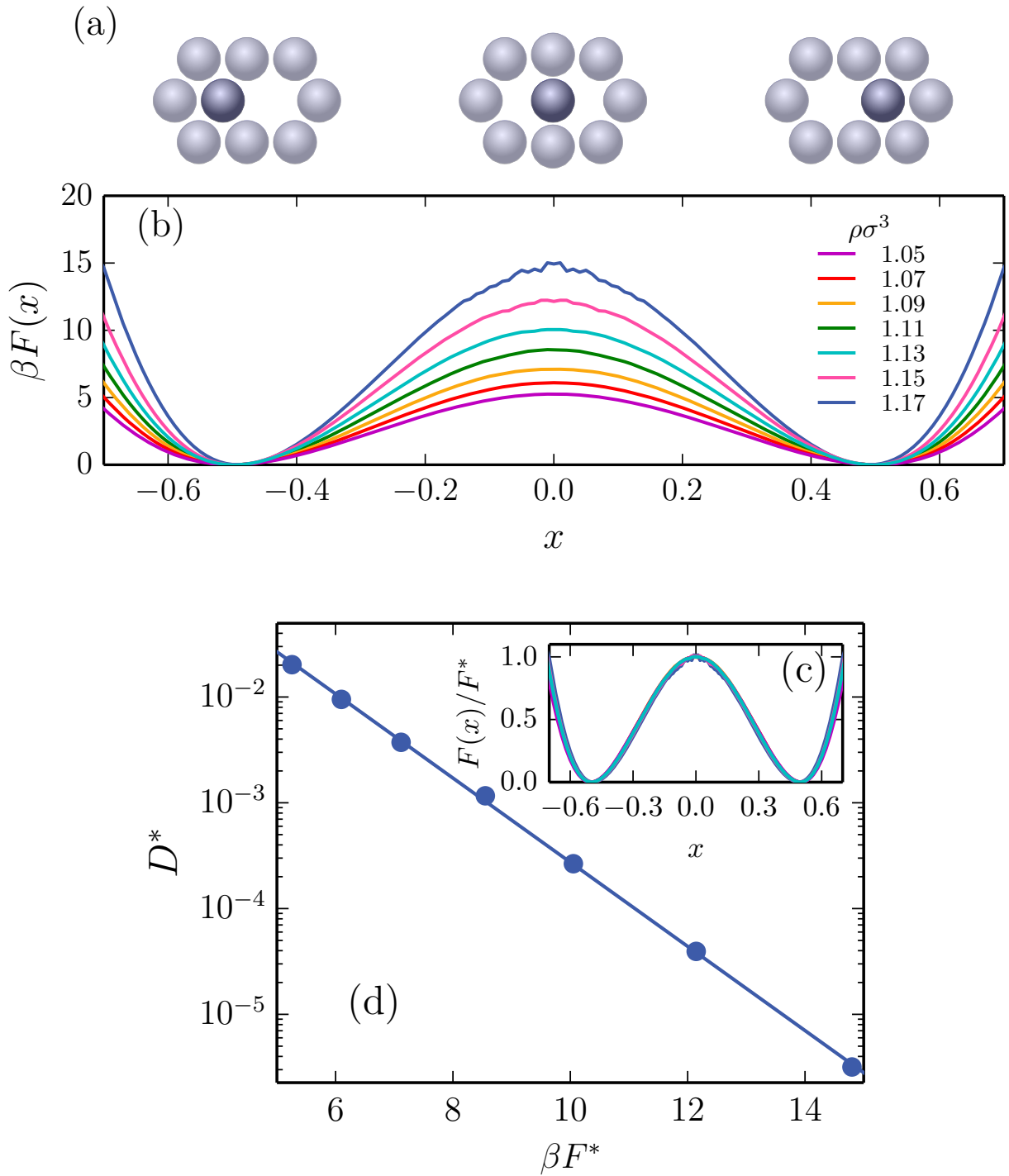


**Figure 2.2:** Free-energy barriers associated with vacancy diffusion. (a) A schematic picture of a hopping vacancy showing a particle at the left lattice site  $x = -\frac{1}{2}$ , at the transition state  $x = 0$ , and at the right lattice site  $x = \frac{1}{2}$ . (b) The free-energy barrier for vacancy diffusion  $\beta F(x)$  for a range of densities. (c) The normalized free-energy barrier for vacancy diffusion, which collapses for many different densities unto a single profile. (d) The exponential dependence of the vacancy diffusion constant  $D^*$  on the barrier height  $\beta F^*$ .

site and the neighbouring vacant lattice site. By projecting the positions of this hopping particle onto the line that connects the two lattice sites we obtain the free-energy barrier using  $\beta F(x) = -\ln(P(x))$  with  $P(x)$  the probability distribution function of the projected particle coordinate  $x$ . Here  $x = \pm\frac{1}{2}$  corresponds to the particle being located at one of the lattice sites, and  $x = 0$  corresponds to the transition state. This is sketched in Figure 2.2(a).

In Figure 2.2(b), we show the predicted free-energy barriers associated with vacancy hopping for a range of densities. These free-energy profiles confirm that the height of the free-energy barrier increases strongly with increasing density. Interestingly, we observe no changes in the shape of the free-energy barriers. To show this, we normalize all free-energy profiles by their maximum barrier height  $\beta F^*$ , and obtain an excellent collapse, as shown in Figure 2.2(c).

The increasing height of the free-energy barrier for vacancy hopping is solely responsible for the slowing down of vacancy diffusion. In Figure 2.2(d), we plot the activation energy  $\beta F^*$  versus the vacancy diffusion coefficient  $D_v$ , and obtain a clear exponential dependence.

### 2.3.3 Interactions between point defects

Next, we quantify the interactions between point defects. Our method is based on recent simulation studies of the interactions between point defects in two-dimensional colloidal systems of dipolar spheres [118, 122]. Here, we apply this method to hard-sphere crystals, in three dimensions.

We start off by introducing either two vacancies or two interstitials into the crystal, and follow their motion over time. In the case of vacancies, the separation distance between the two empty lattice sites located at positions  $\mathbf{R}_i^{\text{vac}}$  and  $\mathbf{R}_j^{\text{vac}}$  is given by  $r = |\mathbf{R}_i^{\text{vac}} - \mathbf{R}_j^{\text{vac}}|$ . The separation distance  $r$  can now be used to define an effective potential as

$$\beta F(r) = -\ln \frac{P(r)}{n_L(r)}, \quad (2.2)$$

where  $P(r)$  is the probability to find the vacancy pair at a separation distance  $r$  and  $n_L(r)$  is the number of lattice sites at a distance  $r$  from a reference lattice site. In the case of interstitials, we choose to express the separation distance also in terms of the distance between the two doubly occupied lattice sites  $r = |\mathbf{R}_i^{\text{int}} - \mathbf{R}_j^{\text{int}}|$ , where  $\mathbf{R}_i^{\text{int}}$  and  $\mathbf{R}_j^{\text{int}}$  refer to the positions of the two doubly occupied lattice sites.

The effective potential for the vacancy-vacancy interaction is shown in Figure 2.3(a) for a range of densities  $\rho$ . Clearly the vacancy-vacancy interactions are only weakly attractive for all densities ( $\approx -1k_B T$ ). These weak attractions highlight that indeed mono-vacancies do not form stable vacancy clusters, in agreement with the early results of Bennett and Alder [117], who showed that the concentrations of higher-order vacancies are significantly smaller than those of mono-vacancies. During the simulation, we observe that a di-vacancy will occasionally form from the fusion of two mono-vacancies, but that these clusters break up continually. Thus entropy alone cannot stabilize vacancy clusters but rather tends to stabilize mono-vacancies due to the large number of possible configurations and its associated combinatorial entropy. Interestingly, the vacancy-vacancy interactions

weaken slightly with increasing density; yet we observe very little density-dependence in the vacancy-vacancy interactions [Figure 2.3(a)].

We also show the effective potentials for the interstitial-interstitial interactions for varying densities  $\rho$  [Figure 2.3(b)]. In contrast to the vacancies, the interactions between interstitials are found to be strongly attractive, and range many lattice sites. As such, we find that interstitials form long-lived di-interstitials, which only sporadically manage to dissociate into separate mono-interstitials. Thus entropy alone plays an important role in stabilizing interstitial clusters. We observe a large density-dependence on the interstitial-interstitial interactions. Namely, the effective interactions between interstitials become substantially stronger as the lattice becomes more compact with increasing density. Unfortunately, we were unable to properly sample the effective interactions at higher densities due to these strong interactions.

Interestingly, if we calculate the  $g(r)$  of the interstitial particle coordinates (instead of the interstitial lattice sites), and subsequently use  $\beta F(r) \approx -\ln(g(r))$  we obtain an extremely similar effective potential (black solid line). This highlights that our way of calculating the effective interactions is robust, and does not depend on the exact definition of the interstitial coordinate.

### 2.3.4 Displacement field of point defects

Intuitively, the interactions between defects arise from the strain that these point defects generate inside the crystal lattice. To this end, we calculate the average displacements around a single vacancy and a single interstitial. Specifically, we define the displacement  $\mathbf{u}_i = \mathbf{r}_i - \mathbf{R}_i$  of a particle  $i$  with respect to its lattice site  $\mathbf{R}_i$ . For each lattice site, we

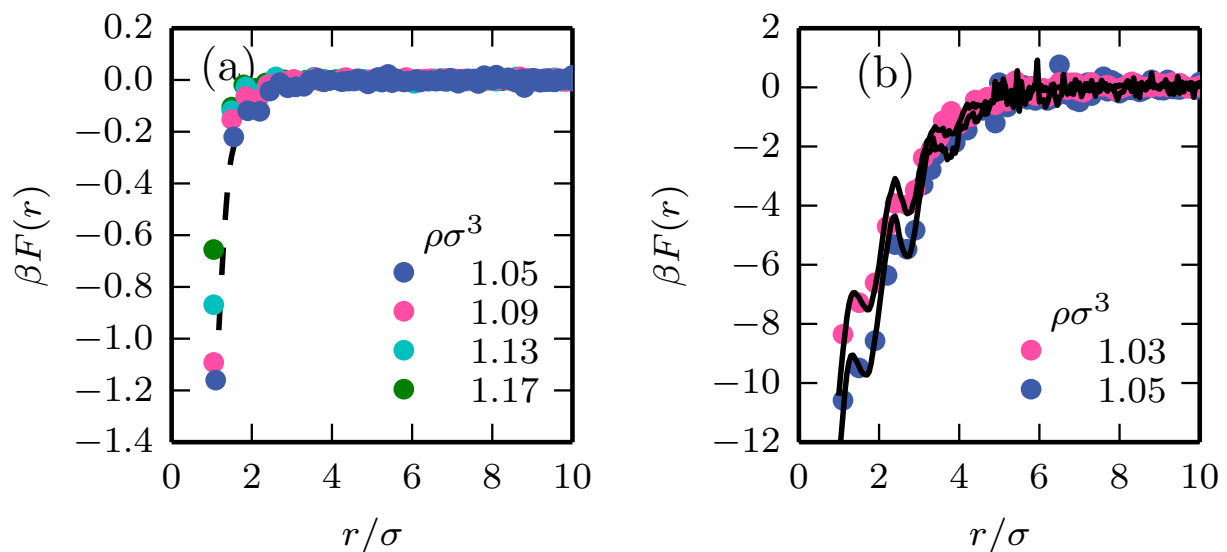


**Figure 2.3:** Effective interactions between two vacancies (a) and two interstitials (b). The dotted black line in (a) is a guide to the eye. The solid black line in (b) corresponds to the interstitial-interstitial interaction potential as obtained from a  $g(r)$ -inversion.

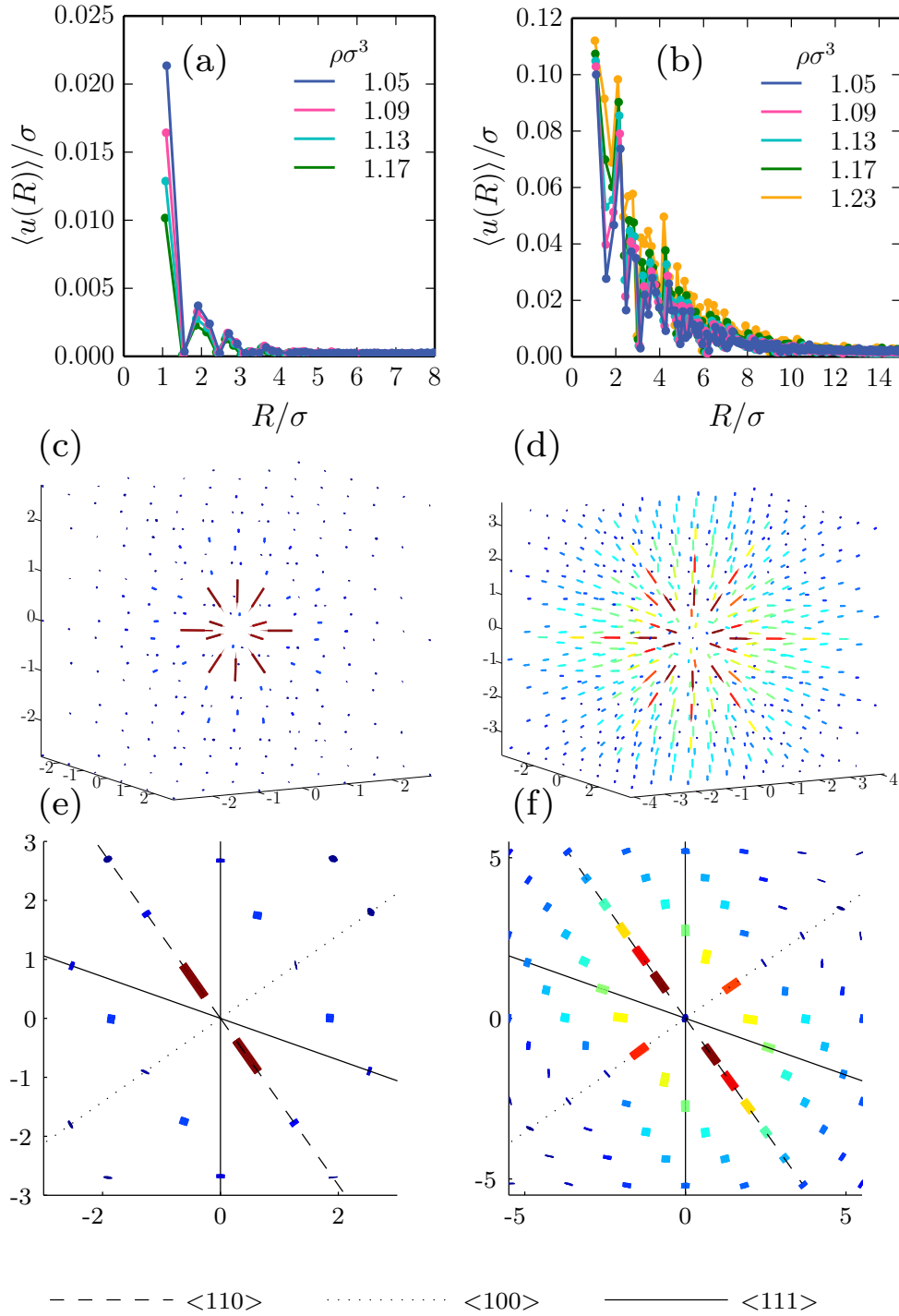


**Figure 2.4:** The average displacements  $\langle u(R) \rangle$  around a vacancy (a) and an interstitial (b) for various densities. (c) The displacement field  $\langle \mathbf{u}(\mathbf{R}) \rangle$  around a vacancy at  $\rho\sigma^3 = 1.05$ . (d) The displacement field  $\langle \mathbf{u}(\mathbf{R}) \rangle$  around an interstitial at  $\rho\sigma^3 = 1.23$ . (e) The displacement field  $\langle \mathbf{u}(\mathbf{R}) \rangle$  in the  $\{110\}$ -plane around a vacancy at  $\rho\sigma^3 = 1.05$ . (f) The displacement field  $\langle \mathbf{u}(\mathbf{R}) \rangle$  in the  $\{110\}$ -plane around an interstitial at  $\rho\sigma^3 = 1.23$ . In (c,e) and (d,f) displacement vectors are scaled up by a factor of 30 and 6, respectively. Note that, although not depicted, all vectors for the vacancy (c,e) point inwards, while all vectors for the interstitial (d,f) point outwards. The axes in (c-f) are in units of  $\sigma$ , and the colors merely serve to guide the eye.

then determine the average displacement  $\langle \mathbf{u}(\mathbf{R}) \rangle$  by averaging over many configurations, where  $\mathbf{R} = \mathbf{R}_i - \mathbf{R}^{\text{def}}$  and  $\mathbf{R}^{\text{def}}$  denotes the lattice site containing the defect.

Our results are summarized in Figure 2.4. Specifically, in Figure 2.4(a,b) we plot the magnitude of the average displacements of particles, averaged over all lattice sites at distance  $R = |\mathbf{R}|$  from the defected lattice site, which we denote by  $\langle u(R) \rangle$ . In the case of a vacancy, we observe that particles next to a vacancy tend to relax only a small amount ( $0.01\sigma$ - $0.02\sigma$ ) inward towards the vacancy center, as shown in Figure 2.4(a). Moreover, the displacements of particles are short-ranged; only the nearest neighbours feel the local dilation of the lattice. This is also clear upon plotting the average displacement vectors  $\langle \mathbf{u}(\mathbf{R}) \rangle$ , as shown in Figure 2.4(c), where vectors are scaled up by a factor of 30. As such, we conclude that the vacancies hardly perturb the lattice. Note that with increasing density, the displacements around the vacancy decrease [Figure 2.4(a)].

In contrast, interstitials cause substantial displacements of surrounding particles from their lattice sites: the nearest-neighbouring particles are forced to displace large amounts from their lattice sites in order to be able to accommodate the interstitial particle. These particle displacements occur even over large distances from the core of the defect; the local deformation of the lattice is felt over many lattice sites from the interstitial center, as shown in Figure 2.4(d). The displacements increase with increasing packing fraction [Figure 2.4(b)]. Note that in the region near the center of the interstitial ( $r \lesssim 10\sigma$ ) the displacements decay exponentially, as was also observed previously in a simple bead-spring model [123, 124]. Thus, somewhat surprisingly we find similar scaling to the bead-spring model, despite the presence of hard interactions in our system.

From Figure 2.4(c,d) it is clear that the displacements for both interstitials and vacancies are more pronounced along certain lattice directions than others. Thus, what appears as noise in Figure 2.4(a,b) actually stems from anisotropic strains inside the lattice. This anisotropy is clearly visible in plots of the displacements in 2d planes that pass through the defect. In Figure 2.4(e,f) we plot such a plane, namely the  $\{110\}$ -plane that intersects the defect. This plane allows us to examine the strain along the  $\langle 110 \rangle$ ,  $\langle 100 \rangle$ , and  $\langle 111 \rangle$  directions, among others. Interestingly, these plots show that both for vacancies as well as interstitials, the displacements are most pronounced along the  $\langle 110 \rangle$ -direction, while displacements along the other primary crystal axes,  $\langle 100 \rangle$  and  $\langle 111 \rangle$ , are significantly weaker. Note that this anisotropic character to the strain fields is also responsible for the fluctuations in the interactions plotted in Figure 2.3.

## 2.4 Discussion and Conclusions

In conclusion, we have studied the diffusion, interactions, and strain fields of the simplest point defects in the hard-sphere model system. We have shown that the vacancy diffusion decreases rapidly as the density is increased, while the interstitial diffusion exhibits a much weaker density dependence. The rapid decrease of the vacancy diffusion was found to be directly related to the increase in the height of the predicted one-dimensional free-energy barriers. Additionally, we have quantified the interactions between vacancies, which were shown to be weakly attractive and short-ranged, and between interstitials, which were found to be strongly attractive and act over much larger distances. Thus we

found that entropy alone cannot stabilize vacancy clusters but rather tends to stabilize mono-vacancies, while interstitials tend to cluster into long-lived multi-interstitials. We also measured the average particle displacements around a single vacancy and a single interstitial. For vacancies, only the neighbouring particles were found to displace a small amount towards the vacancy center, while for interstitials the particles displacements are large, and even involve particles that are many lattice sites away from the defect center. This is well reflected in the effective interactions we have calculated, which were found to be weak and short-ranged for vacancies, and strong and wide-ranging for interstitials.

The fact that vacancy diffusion goes down rapidly with increasing density explains why vacancies in the dense, lower regions of sediments will not be able to anneal out, as observed in both experiments and simulations [125, 126]. For interstitials we found a much less strong density-dependence on the diffusion constant. This feature may be especially relevant under out-of-equilibrium conditions where the crystal is perturbed (e.g. radiation damage or through the application of optical tweezers) and point defects are generated: while the interstitials may still be able to diffuse to the boundaries and anneal out, the vacancies will be stuck inside the bulk of the crystal. We hypothesize that the reason that vacancies slow down so drastically is that they are perfectly commensurate with the lattice, and do not impose any lattice distortions. Namely, at high densities the jumping particle requires significant displacements of the surrounding particles in order to be able to pass through. Yet, these fluctuations become increasingly less probable at higher densities. For interstitials, however, the surrounding particles are always forced to deviate from their lattice site, in order to be able to accommodate the extra particle, and small collective displacements can lead to diffusion of the interstitial defect. It would be interesting to investigate further whether, similar to the 2d case [127–130], distinct topological configurations of single point defects can be identified and connected to defect diffusion and rotation.

Lastly, we would like to point out that the predicted free-energy barriers associated with vacancy diffusion all collapse onto a single curve when normalized by the barrier height. For further research it would be interesting to investigate where this collapse originates from.

## 2.5 Acknowledgements

I would like to thank Marijn van Huis, Frank Smalenburg, and Michiel Hermes for useful discussions and carefully reading the corresponding manuscript.

---

## Diffusion and interactions of interstitials in hard-sphere interstitial solid solutions

---

Using computer simulations we study the dynamics and interactions of interstitial particles in hard-sphere interstitial solid solutions. We calculate the free-energy barriers associated with their diffusion for a range of size ratios and densities. By applying classical transition state theory to these free-energy barriers, we predict the diffusion coefficients, which we find to be in good agreement with diffusion coefficients as measured using event-driven molecular dynamics simulations. These results highlight that transition state theory can capture the interstitial dynamics in the hard-sphere model system. Additionally, we quantify the interactions between the interstitials. We find that, apart from excluded volume interactions, the interstitial-interstitial interactions are almost ideal in our system. Lastly, we show that the interstitial diffusivity can be inferred from the large-particle fluctuations alone, thus providing an empirical relationship between the large-particle fluctuations and the interstitial diffusivity.

### 3.1 Introduction

Solid solutions occur when one species is dissolved within the host crystal of another species. The Hume-Rothery rules state that whether or not a solid solution may form, and in which way the two components mix, is largely controlled by the ratio  $q = \sigma_a/\sigma_b$  of the diameters  $\sigma_{a,b}$  of the two species [131]. In particular, we expect two distinct types of solid solutions to occur depending on the size ratio. More specifically, for  $q \gtrsim 0.85$  solid solutions occur where the solute is incorporated into the solvent crystal lattice via substitution, i.e. by replacing a particle in the host lattice, while at smaller size ratios  $q \lesssim 0.4$  small solutes are fitted interstitially within the voids of the host crystal lattice [131]. Examples of such solid solutions can be found in the atomic realm, but also in colloidal systems [35–42, 116, 132, 133].

Over the last decades, colloidal “hard spheres” have provided an excellent model system to investigate a variety of problems in condensed matter physics, such as glass transitions [94–96], crystal nucleation [97–102], and optimal packings [103–106]. Likewise, binary mixtures of hard spheres provide a simple model system to study solid solutions. More specifically, theory and simulations reveal a thermodynamically stable substitutionally disordered crystal phase in hard-sphere systems with size ratios  $q \geq 0.85$ , thus highlighting the validity of the Hume-Rothery rules [35–40]. Moreover, recent colloidal realizations of interstitial solid solutions have opened the door for direct observation of these mixtures in real space and real time using microscopy [41, 42, 132]. For hard spheres, both experiments and simulations demonstrate the stability of interstitial solid solutions for binary mixtures with a size ratio of  $q = 0.30$  [41]. This interstitial solid solution is obtained by filling the octahedral holes of a face-centered cubic crystal of large particles with small particles. It was shown that the diffusion of the small particles occurs through hopping between neighbouring octahedral holes via an intermediate tetrahedral hole. Surprisingly, in this system, the interstitial diffusion increased with increasing interstitial concentration, due to a lowering of the free-energy barrier associated with interstitial diffusion [41]. More recently, Tauber *et al.* found that in body-centered cubic crystals of soft particles, the interstitial dynamics deviate substantially from predictions based on classical transition state theory in which the base crystal was considered to be static [132]. Such classical theories attempt to predict the interstitial dynamics from the activation barrier associated with an interstitial particle hopping between adjacent interstitial sites [134]. The breakdown of transition state theory in Ref. [132] was attributed to the importance of thermal excitations of the host crystal lattice, and to the presence of strong interstitial-interstitial interactions. It remains to be seen whether or not transition state theory can capture the interstitial dynamics in the binary hard-sphere model system.

In this Chapter, we study the dynamics and interactions of interstitials in hard-sphere interstitial solid solutions. We calculate the free-energy barriers associated with interstitial diffusion for a wide range of size ratios and densities. For very small interstitials  $q = 0.1$  we find that the barrier height depends only on the density of the large particles, and not on the stoichiometry. For interstitials of intermediate size ratios  $0.2 \leq q \leq 0.35$ , we observe that for increasing stoichiometry the barrier height decreases. For large interstitials  $q > 0.35$  we observe a more intricate dependence of the barrier height on the stoichiometry, where the barrier transitions from decreasing to increasing in height with stoichiometry,

as the large-sphere density is increased. Next, we apply classical transition state theory to these free-energy barriers in order to predict the diffusion coefficients of interstitials, and obtain good agreement with diffusion coefficients as measured using event-driven molecular dynamics simulations. These results highlight that transition state theory can capture the interstitial dynamics in the hard-sphere model system. Additionally, we quantify the interactions between interstitials in our system, and find that, apart from excluded volume interactions, the interstitial-interstitial interactions are almost ideal. Finally, we show that the interstitial diffusivity can be inferred from the large-particle fluctuations alone, thus providing an empirical relationship between the two.

## 3.2 Model and Methods

Using computer simulations, we investigate interstitial solid solutions consisting of  $N_l$  large particles and  $N_s$  small particles with a size ratio  $q = \sigma_s/\sigma_l$ , where  $\sigma_l$  and  $\sigma_s$  are the large and small particle diameters, respectively. The stoichiometry is defined as  $n = N_s/N_l$ . The interstitial solid solutions are initialized by creating a face-centered cubic crystal of large particles and distributing the small interstitials randomly among the octahedral holes. The dynamics of these systems are investigated using event-driven molecular dynamics (EDMD) simulations [91, 135]. We define the EDMD unit time as  $\tau = \sqrt{\beta m_l \sigma_l^2}$ , where  $m_l$  is the mass of a large particle, and  $\beta = 1/k_B T$  with  $k_B$  Boltzmann's constant and  $T$  the temperature. For the small particle mass we used  $m_s = m_l \sigma_s^3/\sigma_l^3$ .

For the calculations of the free-energy barrier associated with interstitial diffusion, and the calculations of the interstitial-interstitial interactions we employ Monte Carlo (MC) simulations. In these MC simulations, the incorporation of ‘‘hopping’’ moves allows for more efficient sampling. More specifically, apart from regular translational moves of particles, we also allow the small particles to move an integer number of lattice spacings, which greatly enhances the probability that an interstitial will jump into another octahedral hole.

In our simulations, we typically fix the packing fraction of the large spheres  $\eta_l = \pi N_l \sigma_l^3/6V$ , where  $V$  is the volume of the system, and vary the stoichiometry. Note that for all analysis we corrected for drift in the center of mass of the host lattice.

## 3.3 Results

### 3.3.1 Diffusion of interstitial particles

#### Free-energy barriers

It has been previously observed in Ref. [41] that in hard-sphere interstitial solid solutions the small particles reside mainly in the octahedral holes in the host lattice [Figure 3.1(a)], and diffuse by hopping through a neighbouring tetrahedral hole [Figure 3.1(b)]. It should be noted that each octahedral hole is connected to eight adjacent tetrahedral holes, while each tetrahedral is connected to four octahedral holes. We start off by examining the free-energy barriers associated with the transitions between octahedral and tetrahedral

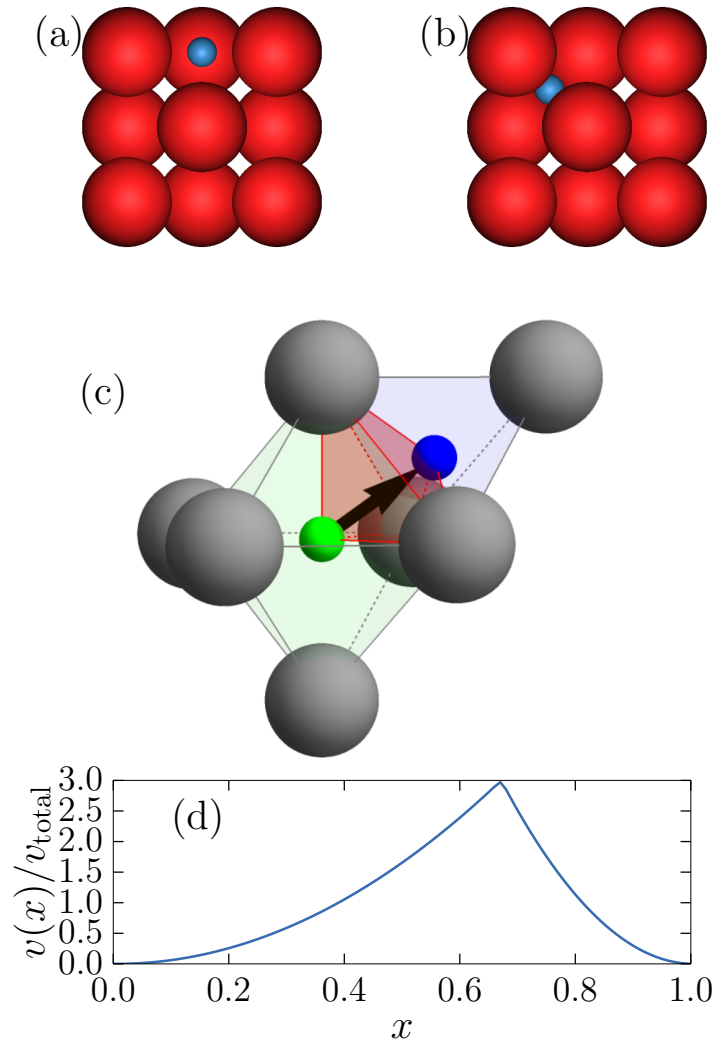


**Figure 3.1:** Interstitial particle (blue) located at (a) an octahedral hole  $x = 0$ , and (b) a tetrahedral hole  $x = 1$ . (c) Schematic representation of the volume (red) projected onto the line between a specific octahedral hole (green) and a specific tetrahedral hole (blue). Large particles are indicated in gray. The black arrow indicates the path along which  $x$  is measured. (d) The projected volume  $v(x)$  along the coordinate  $x$ .

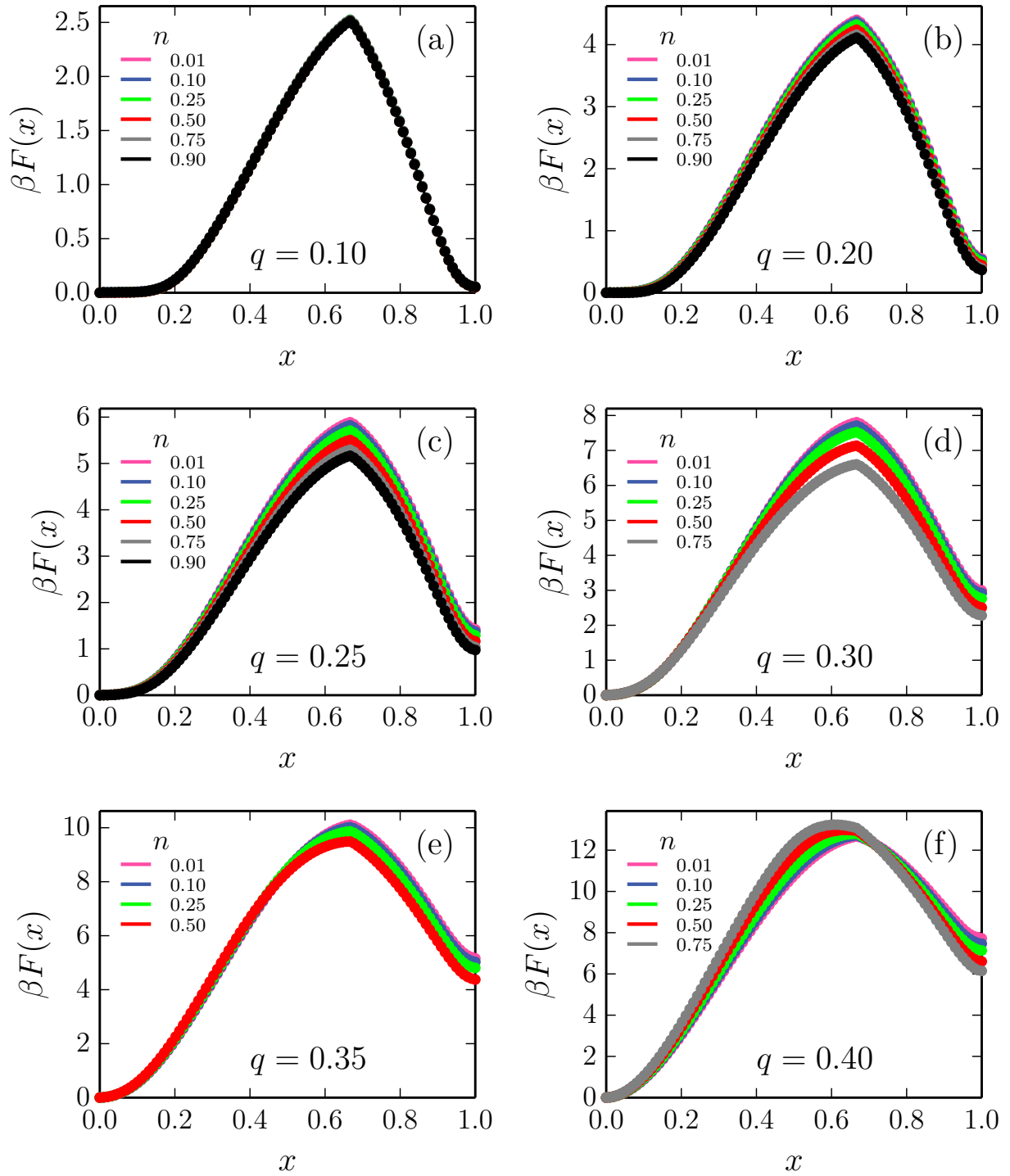


**Figure 3.2:** Free-energy barriers associated with the diffusion of interstitials at a large-sphere packing fraction  $\eta = 0.60$  for various size ratios: (a)  $q = 0.10$ , (b)  $q = 0.20$ , (c)  $q = 0.25$ , (d)  $q = 0.30$ , (e)  $q = 0.35$ , and (f)  $q = 0.40$ .

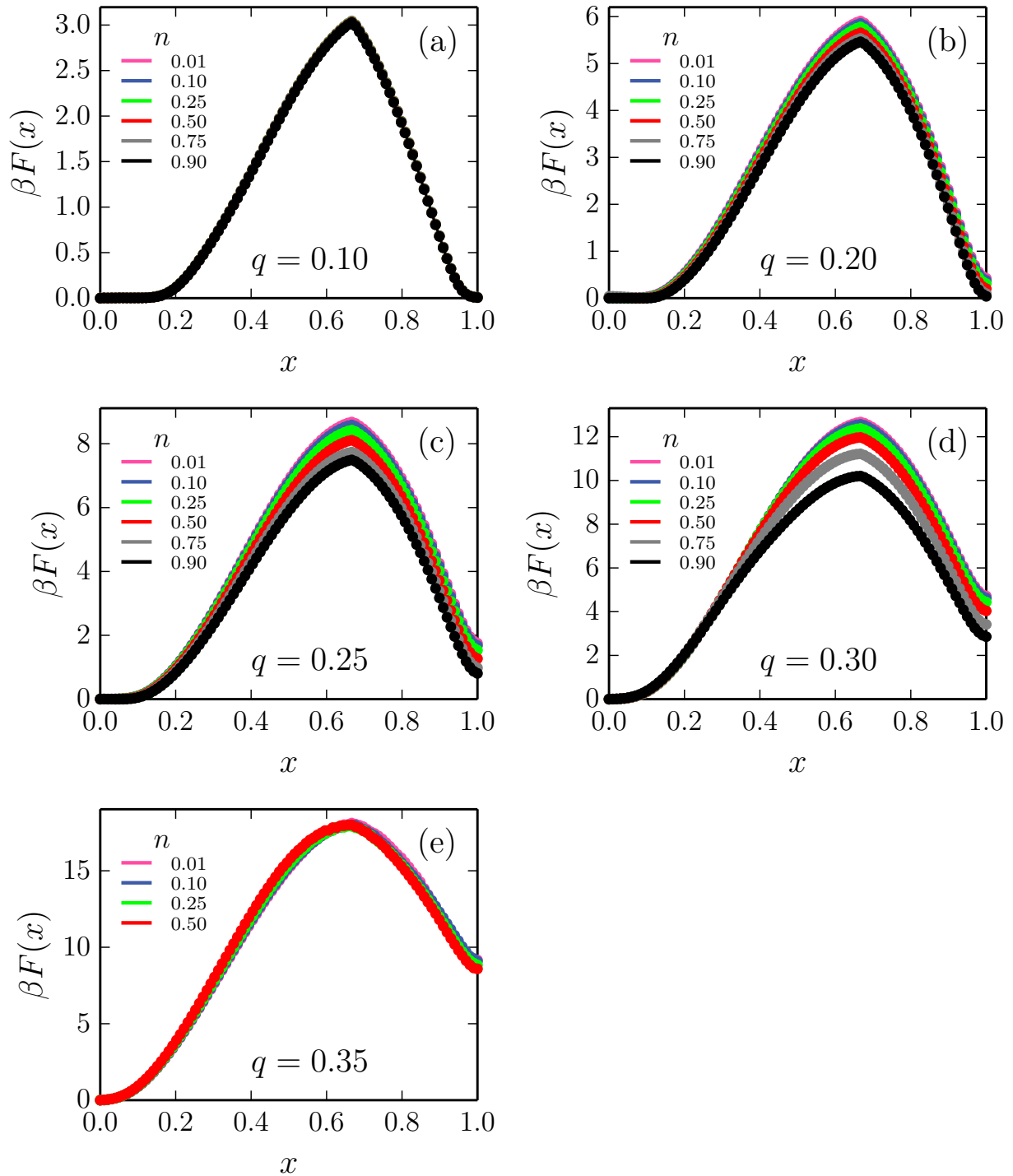


**Figure 3.3:** Free-energy barriers associated with the diffusion of interstitials at a large-sphere packing fraction  $\eta_l = 0.64$  for various size ratios: (a)  $q = 0.10$ , (b)  $q = 0.20$ , (c)  $q = 0.25$ , (d)  $q = 0.30$ , and (e)  $q = 0.35$ .

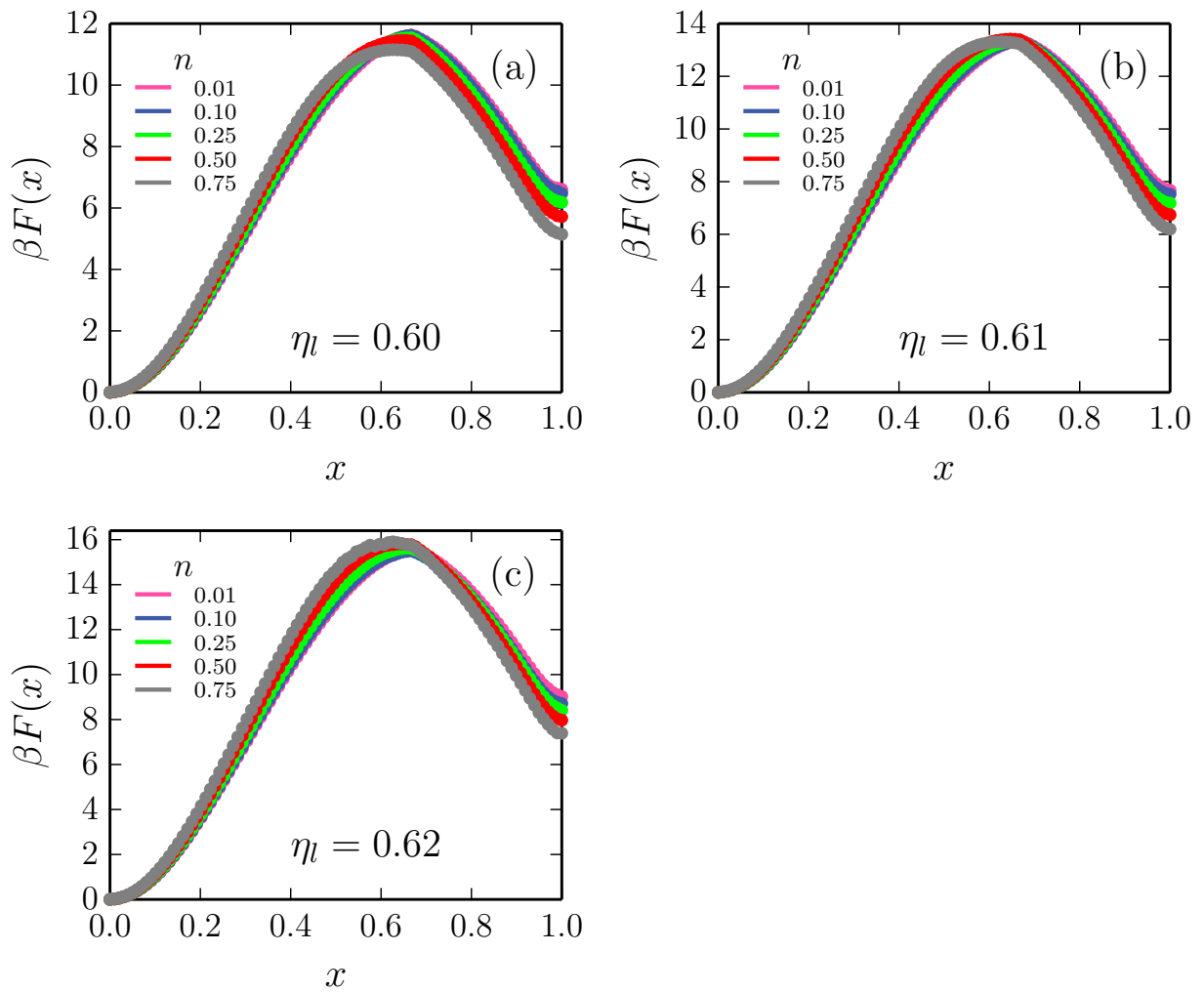


**Figure 3.4:** Free-energy barriers associated with the diffusion of interstitials for a size ratio  $q = 0.38$ : (a)  $\eta_l = 0.60$ , (b)  $\eta_l = 0.61$ , and (c)  $\eta_l = 0.62$ .

holes, for a range of large-sphere packing fractions  $\eta_l$ , stoichiometries  $n$ , and size ratios  $q$ . To this end, we project the positions of the interstitial particles onto the line that connects the neighbouring octahedral and tetrahedral holes. We obtain a free-energy barrier using  $\beta F(x) = -\ln(P(x)\sigma_l^3/v(x))$  with  $P(x)$  the probability distribution function of the projected particle coordinate  $x$ , and  $v(x)$  the projected volume, as shown in Figure 3.1(c,d). Hence we normalize this free-energy barrier to the probability distribution function of an ideal gas. Here  $x = 0$  corresponds to the particle being located at the center of the octahedral hole, and  $x = 1$  corresponds to the center of the tetrahedral hole.

We show these free-energy barriers for a range of size ratios and stoichiometries in Figures 3.2 and 3.3, for host crystal packing fractions of  $\eta_l = 0.60$  and  $\eta_l = 0.64$ , respectively. We observe these free-energy barriers to exhibit a clear single peak around  $x = 0.66$ . This can be understood from the fact that the channel between the octahedral and tetrahedral holes is narrowest at  $x = 2/3$ . Hence, intuitively the small particles are least likely to be found at this position. We identify three behaviours of the free-energy barrier as the stoichiometry  $n$  is increased, depending on the size ratio  $q$ .

For very small interstitials  $q = 0.1$ , we find that the free-energy barriers are independent of the interstitial concentration [Figures 3.2(a) and 3.3(a)]. Here, the diffusion of small particles is governed entirely by the packing fraction of the host crystal. In other words, the interstitials in these systems behave almost ideally. We therefore expect that these systems provide an excellent starting point for more theoretical investigations of diffusion in such systems.

For interstitials of intermediate size ratio  $0.2 \lesssim q \lesssim 0.35$ , we observe that for increasing stoichiometry  $n$  the free-energy barriers decrease, meaning that diffusion will increase [Figures 3.2(b-e) and 3.3(b-d)]. This is in agreement with Ref. [41], where for a size ratio of  $q = 0.30$  the interstitial diffusion was found to increase with increasing stoichiometry. Here we thus show that this feature of increased interstitial diffusivity occurs for a broad range of size ratios.

For large interstitials  $q \gtrsim 0.35$  we observe a more intricate dependence of the barrier height on the stoichiometry  $n$ . Namely, here we find that the large-sphere density starts to play an important role as well. More specifically, we find that the barrier transitions from decreasing to increasing in height with stoichiometry  $n$ , as the large-sphere density is increased. To illustrate this transition, we plot the free-energy barriers for  $q = 0.38$  at different large-sphere packing fractions and stoichiometries in Figure 3.4. Here, for a large-sphere packing fraction of  $\eta_l = 0.60$  we observe that the free-energy barrier goes down with increasing stoichiometry, while at the cross-over  $\eta_l = 0.61$  the free-energy barriers remain constant, and at  $\eta_l = 0.62$  the free-energy barriers increase by increasing the stoichiometry. Note that for very large interstitials  $q = 0.40$  the free-energy barriers always increase with increasing stoichiometry  $n$ , see for example Figure 3.2(f). Interestingly, for these large interstitials we also observe a shift in the peak of the barrier to lower  $x$  as the concentration of small particles increases. This effect is stronger at higher packing fraction. This is likely a result of the small particles disturbing the crystal structure of the large particles.

Lastly, we have checked that these free-energy barriers remain constant upon changing the system size. More specifically, we have calculated the free-energy barrier for two different system sizes, namely  $N_l = 864$  and  $N_l = 4000$ . In Figure 3.5 we plot the free-

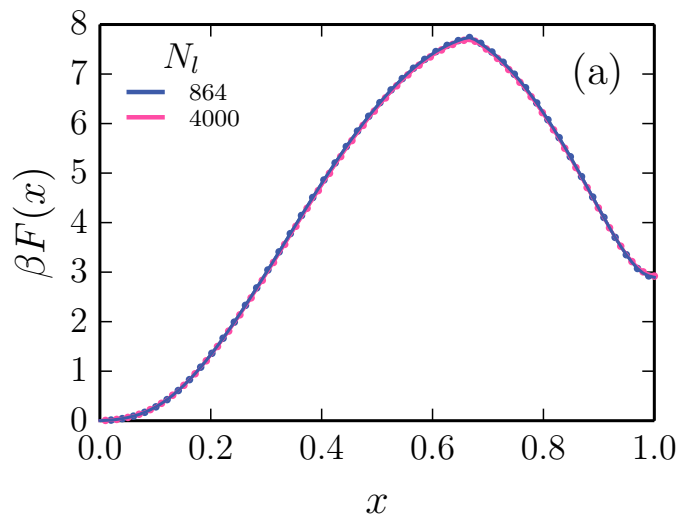


**Figure 3.5:** (a) System-size dependence of the free-energy barriers associated with the diffusion of interstitials for a size ratio  $q = 0.30$  at a large-sphere packing fraction  $\eta_l = 0.60$  and stoichiometry of  $n = 0.10$ . The perfect agreement between the two system sizes,  $N_l = 864$  and  $N_l = 4000$ , shows that there are no significant finite-size effects on the free-energy barrier.

energy barriers at these two different system sizes, and find them to agree very well. Clearly, we observe no significant finite-size effects on the free-energy barrier.

### Mean square displacement of interstitials

Let us now quantify the interstitial diffusivity, in order to be able to compare to predictions based on classical transition state theory in the next section. Using EDMD simulations we study the dynamics of the interstitials by calculating the mean square displacement  $\langle \Delta r_s^2(t) \rangle$ . While the mean square displacement may exhibit more complex scaling at short and intermediate time-scales, we can always safely extract the diffusion coefficient  $D_s$  using the long-term diffusive behaviour of the mean square displacement  $\langle \Delta r_s^2(t) \rangle$ , i.e.

$$D_s = \lim_{t \rightarrow \infty} \frac{\langle \Delta r_s^2(t) \rangle}{6t}. \quad (3.1)$$

To illustrate this, we show several mean square displacement curves for different size ratios in Figure 3.6. At short time scales the interstitial particles move ballistically with  $\langle \Delta r_s^2(t) \rangle \sim t^2$ , while at intermediate time scales the particle dynamics enter a sub-diffusive regime  $\langle \Delta r_s^2(t) \rangle \sim t^\beta$  with  $0 \leq \beta < 1$ . This sub-diffusive dynamics originates from the interstitial particle being “caged” inside an interstitial hole. Yet, at long time scales the interstitial particles manage to hop between neighbouring interstitial holes, giving rise to diffusive dynamics, as characterized by  $\langle \Delta r_s^2(t) \rangle \sim t$ . Using mean square displacements like these we can extract the interstitial diffusivity for a wide range of large-sphere packing fractions  $\eta_l$  and stoichiometries  $n$ .

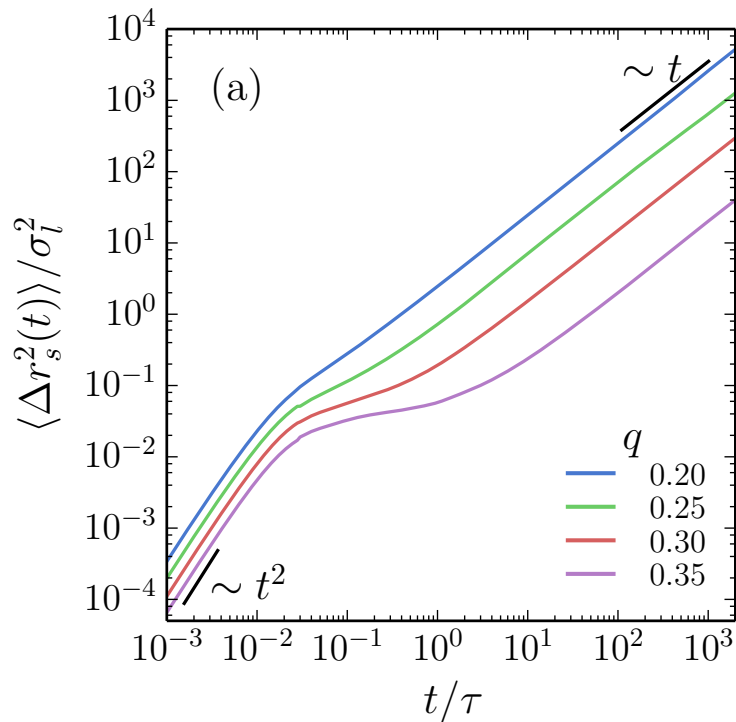


**Figure 3.6:** (a) Mean square displacements of interstitials  $\langle \Delta r_s^2(t) \rangle$  for different size ratios  $q$  at a large-sphere packing fraction  $\eta_l = 0.60$  and a stoichiometry  $n = 0.10$ .

### Transition state theory

We now investigate in more detail the relationship between the interstitial diffusivity and the associated free-energy barriers. To this end, we employ transition state theory to calculate the rate associated with an interstitial hopping between octahedral holes. Note that in a face-centered cubic lattice the octahedral holes are also on a face-centered cubic lattice and that all hopping processes involve an intermediate tetrahedral hole.

In this framework, the diffusion constant of the interstitials  $D_s^{\text{TST}}$  is given by

$$D_s^{\text{TST}} = \frac{1}{12} k_{oo}^{\text{TST}} a^2 \quad (3.2)$$

with  $k_{oo}^{\text{TST}}$  the rate of hopping between octahedral holes, and  $a$  the lattice spacing [136]. Following Ref. [137], we calculate the escape rate associated with interstitial hopping from an octahedral hole into a tetrahedral hole using

$$k_{ot}^{\text{TST}} = \frac{D_0}{\int_a^c dx \exp(-\beta V(x)) \int_b^d dy \exp(\beta V(y))} \quad (3.3)$$

with  $D_0$  the short-time diffusion coefficient of the interstitial,  $\beta V(x) = -\ln(P(x))$  the bare free-energy barrier, which in contrast to  $\beta F(x)$  has not been normalized to an ideal gas, and the integration limits as indicated in Figure 3.7(a). Once an interstitial has jumped into the tetrahedral hole it can jump to any of four neighbouring octahedral

holes, one of which corresponds to its previous position. If we assume this choice to be random, we expect that three out of four hopping events will result in the particle ending up in a different octahedral hole. Note that as the free-energy barriers associated with the first octahedral-to-tetrahedral hopping process are much higher than those associated with the subsequent tetrahedral-to-octahedral hopping process, we expect the rate to be dominated by the first process and make the approximation

$$k_{oo}^{\text{TST}} \approx \frac{3}{4} k_{ot}^{\text{TST}}, \quad (3.4)$$

where the prefactor accounts for the possibility of the interstitial hopping back to its original octahedral hole. Hence, we can predict the relative small-particle diffusion constant

$$\frac{D_s^{\text{TST}}}{D_0} \approx \frac{3a^2}{48} \left[ \int_a^c dx \exp(-\beta V(x)) \int_b^d dy \exp(\beta V(y)) \right]^{-1}, \quad (3.5)$$

which can be calculated directly from the measured free-energy barriers. In Figure 3.7(b) we compare this quantity to the diffusion constant  $D_s$  measured in EDMD simulations. For each size ratio we find an approximately linear relation between  $D_s^{\text{TST}}/D_0$  and  $D_s$ , as one would expect if  $D_0$  is approximately constant for each size ratio. Note that Figure 3.7 includes data for a wide range of host lattice packing fractions at distinct size ratios (colors), and stoichiometries (symbol shapes).

In order to quantitatively predict the diffusion of the small particles from Equation 3.5, we require knowledge of  $D_0$ . In our EDMD simulations, the particles move ballistically at short time scales, and hence  $D_0$  is not clearly defined. Nonetheless, we expect Equation 3.3 to hold with an effective  $D_0$ , which is related to the rate of escape attempts from the octahedral hole. Hence, we estimate the effective  $D_0$  by calculating the collision rate of the small particles  $k_c$ , and use the mean squared displacement to estimate an approximate value for the short-time diffusion coefficient

$$D_0 \approx \frac{\langle \Delta r_c^2 \rangle}{6\tau_c} \quad (3.6)$$

with  $\langle \Delta r_c^2 \rangle$  the mean squared displacement between collisions and  $\tau_c = 1/k_c$  the time-scale between collisions. Note that this corresponds to the diffusion coefficient associated with a three-dimensional random walk with step size  $\langle \Delta r_c^2 \rangle^{1/2}$  and time step  $\tau_c$ .

In Figure 3.7(c), we plot  $D_0$  for different size ratios  $q$  as a function of the large-sphere packing fraction (solid markers). As expected,  $D_0$  is primarily set by the size (mass) ratio. Additionally, we find that  $D_0$  is mildly dependent on the large-sphere packing fraction and the stoichiometry. This data agrees well with a first-order Enskog expression for the self-diffusion coefficient (open markers), given by

$$D_E \approx k_B T \left[ \frac{16\pi}{3} \sigma_{ls}^2 \rho_l g_{ls}(\sigma_{ls}) \sqrt{\frac{k_B T \mu_{ls}}{2\pi}} \right]^{-1}, \quad (3.7)$$

where  $\sigma_{ls} = (\sigma_l + \sigma_s)/2$  is the contact diameter,  $\rho_l$  is the large-particle number density,  $g_{ls}(\sigma_{ls})$  is the value of the pair distribution function at contact, and  $\mu_{ls} = (m_l m_s)/(m_l +$

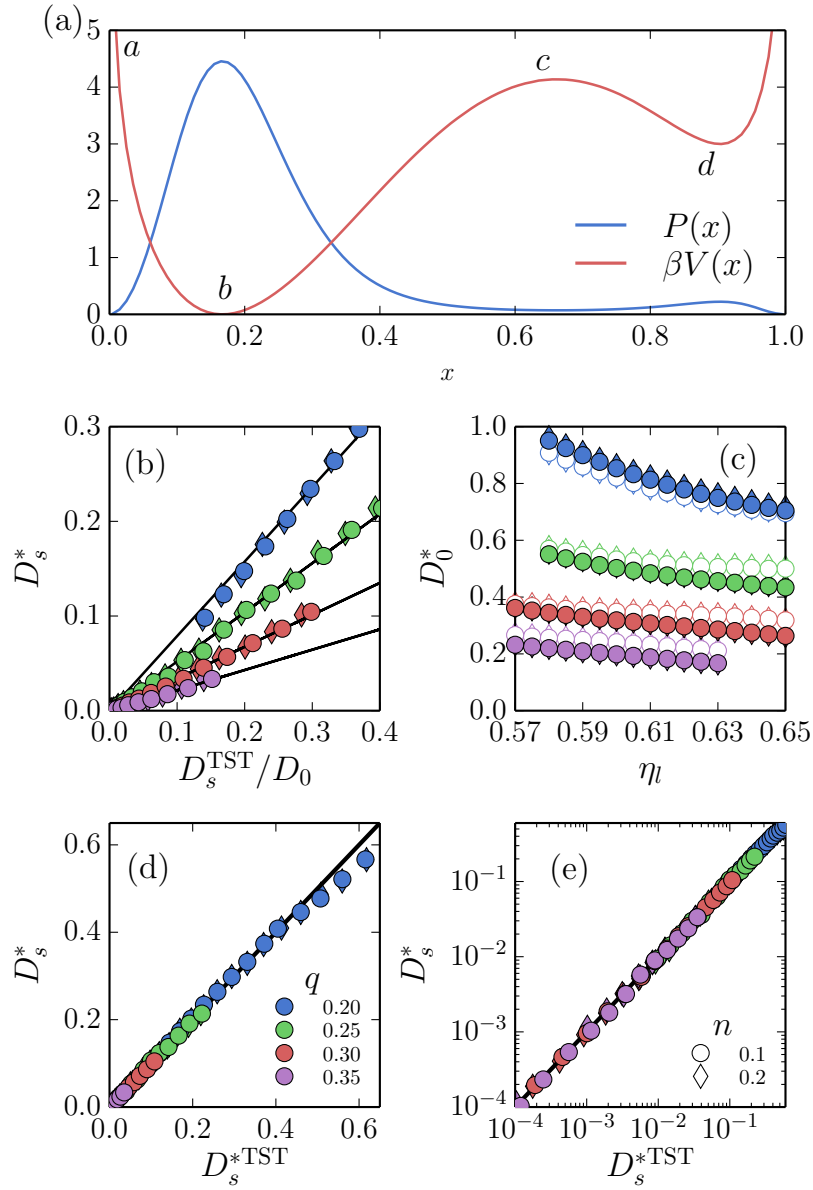


**Figure 3.7:** Predicted and observed diffusion coefficients for interstitials. (a) Sketch of the free-energy barrier  $\beta V(x)$  and probability distribution function  $P(x)$  as a function of the coordinate  $x$  along a transition path. The wells at  $x = b$  and  $x = d$  correspond to the octahedral and tetrahedral hole, respectively, while  $x = c$  corresponds to the transition state. (b) The ratio of the predicted diffusion constant and the short-time diffusion coefficient  $D_s^{\text{TST}}/D_0$  versus the measured diffusion coefficient  $D_s$ . Black lines correspond to linear fits. (c) The short-time diffusion coefficient as calculated using Equation 3.6 (solid markers), and as obtained from the first-order Enskog expression (open markers). (d) The predicted diffusion coefficient  $D_s^{\text{TST}}$  versus the measured diffusion coefficient  $D_s$ . All data collapses unto the black line  $D_s^{\text{TST}} = D_s$ , showing that the diffusion coefficients can be accurately predicted. (e) Same as in (d) but now on log-log scale. Markers with different colors in (b-e) correspond to different size ratios as labelled in (d). Markers with different shapes in (b-e) correspond to different stoichiometries as labelled in (e). Diffusion constants were rendered dimensionless using  $D^* = D\tau\sigma_l^{-2}$ .

$m_s$ ) is the reduced mass [138]. This expression is expected to work for a binary gas of ballistically moving particles. Nonetheless, it here functions as a simple estimate for the short-time diffusion within the octahedral cages.

Using the short-time diffusion coefficient  $D_0$  as calculated from Equation 3.6, we now plot the predicted diffusion coefficient  $D_s^{\text{TST}}$  versus the measured diffusion coefficient  $D_s$  in Figure 3.7(d,e). This data covers a wide range of packing fractions of the host crystal and size ratios, allowing us to test our predicted diffusion constants over multiple orders of magnitude. We find that the diffusion coefficients as predicted from the free-energy barriers  $D_s^{\text{TST}}$  are in excellent quantitative agreement with the measured diffusion coefficients  $D_s$ . Namely, all data largely collapses onto the black line  $D_s^{\text{TST}} = D_s$ , highlighting that the diffusion coefficients can be accurately predicted. A mild deviation was only observed at very high diffusion constants. This can likely be attributed to the finite time it takes an interstitial to move back from a tetrahedral to an octahedral hole, which is neglected due to our approximation in Equation 3.4. Nonetheless, the extremely good overall agreement validates our approximations.

We have thus shown that the diffusion of interstitials in the hard-sphere model system can be accurately described by transition state theory. Interestingly, it was recently found that in soft body-centered cubic crystals the interstitial dynamics deviate substantially from predictions based on classical transition state theory in which the base crystal was considered to be static [132]. This breakdown was attributed both to the importance of thermal excitations of the host crystal lattice, and to the presence of strong interstitial-interstitial interactions [132, 133]. As such, our data raise the interesting question whether or not such interactions between interstitial particles also play an important role in our system. Thus we will now explore further the interstitial-interstitial interactions in our system.

### 3.3.2 Interactions between interstitials

We evaluate the effective interstitial-interstitial interactions using methods similar to those presented in Refs. [118, 122]. More specifically, we first assign all interstitials to their nearest octahedral hole. Subsequently, for each interstitial pair we calculate the (discrete) separation distance between the two occupied holes located at positions  $\mathbf{R}_i$  and  $\mathbf{R}_j$ , which is given by  $r = |\mathbf{R}_i - \mathbf{R}_j|$ . Using this separation distance  $r$  we define an effective potential between interstitials as

$$\beta U_{\text{eff}}(r) = -\ln \frac{P_{\text{pair}}(r)}{h(r)}, \quad (3.8)$$

where  $P_{\text{pair}}(r)$  is the probability to find two interstitials at a separation distance  $r$ , and  $h(r)$  is the number of octahedral holes at a distance  $r$  from a reference octahedral hole.

In Figure 3.8(a-d), we plot the effective interactions between interstitials for a range of size ratios  $q$  at different stoichiometries  $n$  and large-sphere packing fractions  $\eta_l$ . Surprisingly, we find that the interstitials hardly interact with each other. Namely, even for the first shell of neighbouring octahedral sites, we find  $\beta U_{\text{eff}} \approx 0$ . These ideal interactions are in stark contrast to the strong attractions between self-interstitials in single-component hard spheres [Chapter 2]. Only when the interstitials are assigned to the same octahedral site we observe substantial repulsions between interstitials. This repulsion arises from the

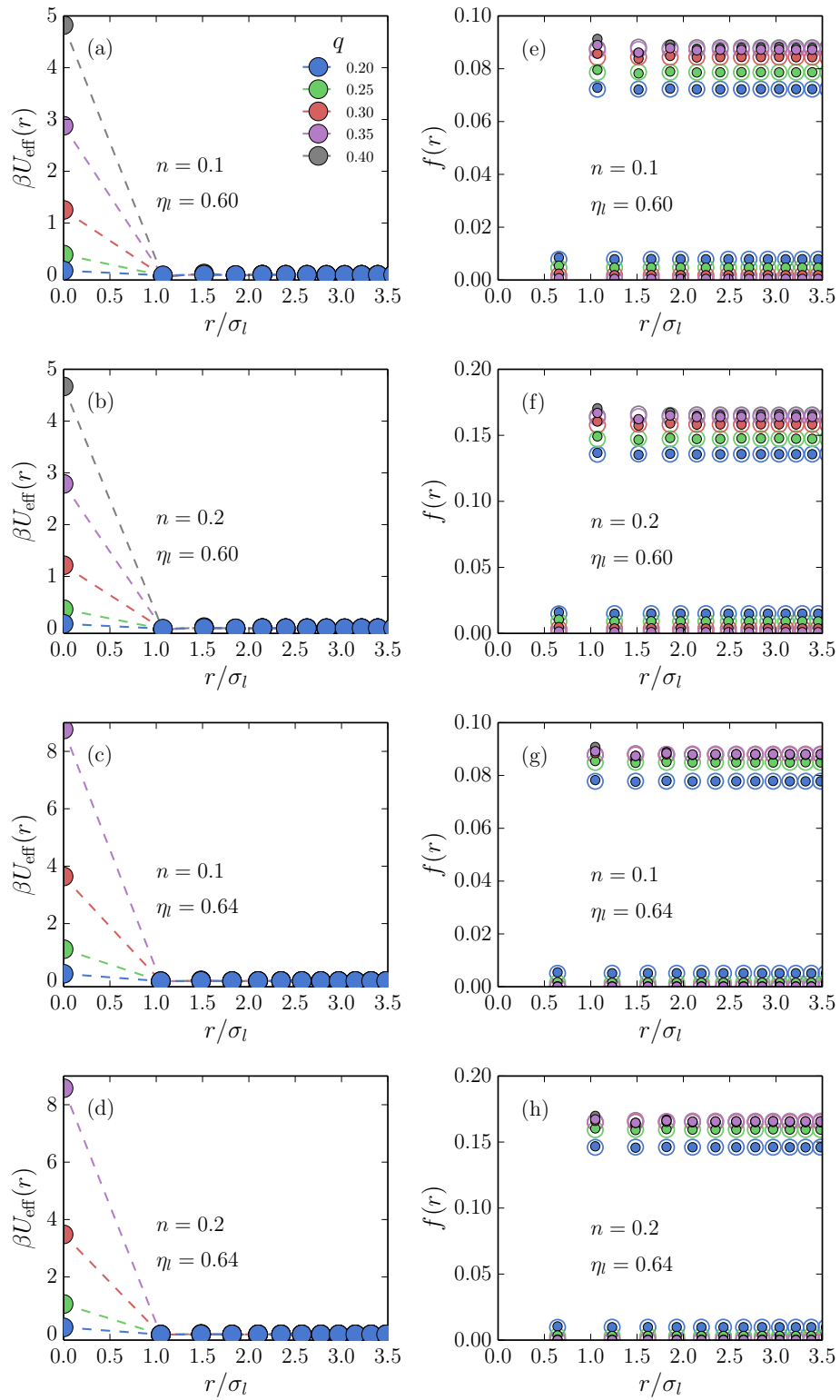


**Figure 3.8:** (a-d) Effective potential between interstitials  $\beta U_{\text{eff}}(r)$  for a range of size ratios  $q$  at different stoichiometries  $n$  and large-sphere packing fractions  $\eta_l$ . Dashed lines are a guide to the eye. (e-h) Corresponding filling parameter  $f(r)$  around an occupied octahedral hole (solid markers) and around an empty octahedral hole (open markers).

hard-core excluded volume interactions between the particles. Note that for the largest size ratio  $q = 0.40$  these excluded volume interactions become so strongly repulsive that we were unable to sample the interactions at  $r = 0$ .

In order to examine the possibility of interactions between particles in adjacent octahedral and tetrahedral holes, we now compare the spatial distribution of interstitials around an empty octahedral hole to that around an octahedral hole containing an interstitial. If there are attractions (repulsions) present between the interstitials, the local density of interstitials around the filled octahedral hole should be on average higher (lower) than in the case of the empty octahedral hole. We quantify this using a filling parameter defined as

$$f(r) = \frac{\langle N_s(r) \rangle}{h(r)}, \quad (3.9)$$

with  $\langle N_s(r) \rangle$  the average number of interstitials in a octahedral or tetrahedral hole at a distance  $r$  from the reference octahedral hole. In Figure 3.8(e-h), we plot this filling parameter associated with the local density of interstitials around the empty octahedral hole, and around the filled octahedral hole, using open and solid markers respectively. Here, two distinct filling fractions are visible, namely the higher filling fraction occurring at distances corresponding to octahedral holes, and a lower filling fraction at distances corresponding to tetrahedral holes. Clearly, we observe that the spatial distribution of interstitials around an empty octahedral hole and around a filled octahedral hole collapse almost perfectly on top of each other (open and solid markers). In both cases we find the filling fraction of the octahedral and tetrahedral holes to be constant and equal to  $nf_o$  and  $n(1 - f_o)$ , respectively, with  $f_o$  the fraction of interstitials located in octahedral holes. Hence, this further demonstrates that, apart from excluded volume interactions, the interstitial-interstitial interactions are essentially ideal in our system.

### 3.3.3 Empirical relationship between the large-particle fluctuations and interstitial diffusivity

In Ref. [41], the increase in interstitial diffusivity with increasing stoichiometry  $n$  was found to coincide with the increase in displacements of the large particles from their lattice site. Here we quantify further the relationship between the displacements of the particles of the host lattice and the diffusivity of the interstitials. To this end, we define a large-particle fluctuation parameter:

$$\delta_l = \sqrt{\langle |\mathbf{R}_{0,i} - \mathbf{r}_i|^2 \rangle} \quad (3.10)$$

with  $\mathbf{r}_i$  the position of a large particle  $i$ , and  $\mathbf{R}_{0,i}$  the position of the lattice site it occupies. In Figure 3.9 we plot the large-particle fluctuation parameter  $\delta_l$  versus the diffusion constant of the small particles  $D_s$  as measured using EDMD simulations. These data were obtained for a wide range of host lattice packing fractions at distinct size ratios (colors), and stoichiometries (symbol shapes). Interestingly, we find that at a fixed size ratio  $q$ , this data collapses onto a single curve for a wide range of stoichiometries  $n$ . Hence, we conclude that the small particle diffusion in these systems is primarily set by fluctuations of the large particles  $\delta_l$ . Note that  $\delta_l$  is dependent not only on the packing fraction of the

large particles, but also on the number of small particles in the crystal. Hence, a larger concentration of small particles increases the fluctuations of the large particles, which in turn increases the small-particle diffusion. Interestingly, although this is a collective dynamic effect between the small particles, their diffusion is still mainly determined by the large-particle fluctuations.

We would like to highlight that the interstitial diffusivity can thus be inferred from the large-particle fluctuations, assuming the curve has been mapped out for a single interstitial concentration. This could be useful for experiments, in which it is typically easier to track the (relatively static) large particles than the highly diffusive interstitials. Curves like those plotted in Figure 3.9 show that the interstitial diffusivity  $D_s$  can be estimated quite accurately via  $\delta_l$ . As such, in experiments the interstitial diffusivity could be obtained at very low stoichiometry, where it may be possible to track individual interstitials, and then easily extended to higher concentrations simply by examining the fluctuations of the larger particles.

### 3.4 Discussion and Conclusions

In conclusion, we have studied the diffusion and interactions of interstitials in hard-sphere interstitial solid solutions. We have calculated the free-energy barriers associated with interstitial diffusion for a range of size ratios and densities. For very small interstitials  $q \lesssim 0.1$  we found that the barrier height depends only on the density of the large particles, and does not depend on the stoichiometry  $n$ . For interstitials of intermediate size ratio  $0.2 \lesssim q \lesssim 0.35$ , we observed that for increasing stoichiometry  $n$  the barrier height decreases. For large interstitials  $q \gtrsim 0.35$  we observe a more intricate dependence of the barrier height on the stoichiometry  $n$ , where the barrier transitions from decreasing to increasing in height with stoichiometry, as the large-sphere density is increased. Next, we applied classical transition state theory to these free-energy barriers to predict the diffusion coefficients of interstitials, and obtained good agreement with diffusion coefficients as measured using EDMD simulations. Additionally, we have quantified the interactions between interstitials. Apart from excluded volume interactions when two interstitials occupy the same hole, we found these interactions to be almost ideal in our system. Lastly, we showed that the interstitial diffusivity can be inferred from the large-particle fluctuations alone, thus providing an empirical relationship between the large-particle fluctuations and the interstitial diffusivity.

Importantly, we have shown that transition state theory can capture the interstitial dynamics in the hard-sphere model system. The free-energy barriers we used for our calculations were measured in a system where the large particles are fluctuating around their lattice sites. This is in contrast to the predictions made in Ref. [132] in which the base crystal was considered to be static, resulting in the interstitial dynamics deviating substantially from predictions based on classical transition state theory. Our results thus highlight the importance of taking these fluctuations into account in order to obtain the relevant free-energy barrier associated with interstitial diffusion. It would be interesting to see whether incorporating these lattice fluctuations for soft systems can recover an accurate description of the interstitial dynamics using transition state theory.

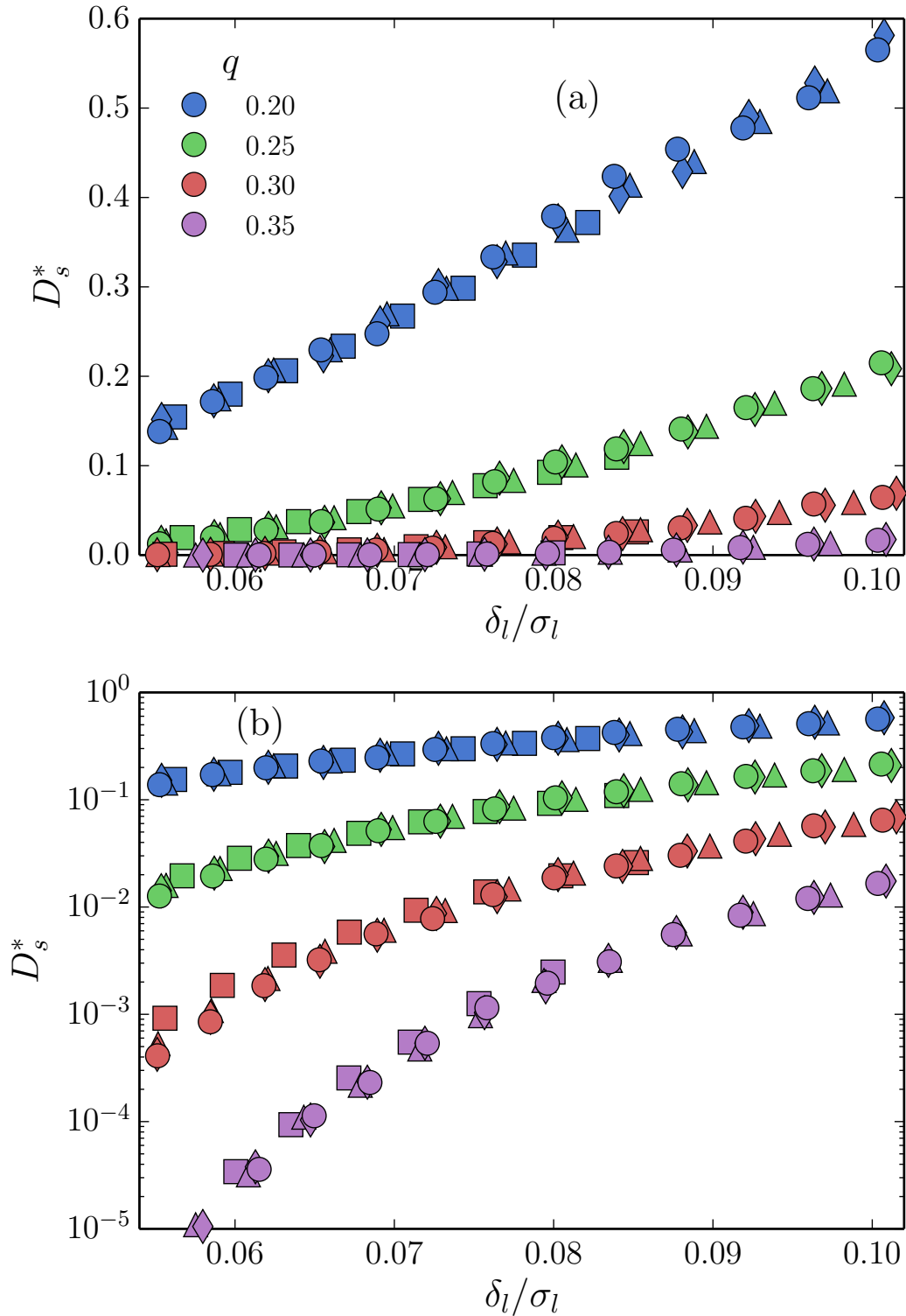


**Figure 3.9:** (a) Relationship between the large-particle fluctuations  $\delta_l$  and the interstitial diffusivity  $D_s$ . (b) Same as in (a) but now on log scale. The circle, diamond, triangle and square markers correspond to stoichiometries of  $n = 0.1$ ,  $n = 0.1875$ ,  $n = 0.375$ , and  $n = 0.75$  respectively. Diffusion constants were rendered dimensionless using  $D^* = D\tau\sigma_l^{-2}$ .

## 3.5 Acknowledgements

The work in this Chapter was performed in collaboration with Emma Lathouwers, who carried out preliminary calculations on the free-energy barriers and the interstitial-interstitial interactions as a part of her bachelor's thesis. I would like to thank Frank Smalenburg for help with the event-driven molecular dynamics simulations and many useful discussions. I would also like to thank Vasileios Prymidis for carefully reading the corresponding manuscript.

---

## Antisite defects induce non-stoichiometry in the hard-sphere colloidal Laves phase

---

Binary mixtures of hard spheres can spontaneously self-assemble into binary crystals. Computer simulations have been especially useful to map out the phase behaviour of these mixtures in detail, under the assumption that the stoichiometry of the binary crystal is ideal. Here we show that for a size ratio of  $q = 0.82$  this assumption is not valid near the fluid-Laves coexistence region. Specifically, we find an antisite defect concentration of up to 2% to be present in the  $\text{MgZn}_2$  Laves phase. Our results shed new light on the self-assembly of the colloidal Laves phases.

## 4.1 Introduction

In equilibrium, even the most perfect crystal is marred by a small concentration of point defects, such as vacancies and interstitials. Interestingly, while these defects can strongly affect the optical and mechanical properties of crystalline materials, and are the main agents for transport in crystals, most theoretical and numerical studies that predict phase boundaries ignore them. In most cases, and in particular in the case of single-component systems, this is fully justifiable: the high free-energy cost of creating a defect ensures that they only occur in low concentrations [107, 117]. In multicomponent systems, this assumption is also generally made, but perhaps less justifiable.

In systems of more than one component, in addition to vacancies and interstitials, new forms of point defects arise: a lattice site of one species can be filled by a particle of another species, creating a so-called “antisite” defect [9]. If the intruding particle is sufficiently similar to the original one, the free-energy cost carried by the creation of such a defect can be relatively small, opening the door to much larger defect concentrations. Nonetheless, studies predicting colloidal phase diagrams have to date ignored these defects (see e.g. [46–48, 50, 53, 139]).

Here, we explore the effect of antisite defects on the phase diagram of a binary hard-sphere mixture. Binary hard-sphere mixtures are perhaps the simplest possible model for studying binary crystal structures, and have been instrumental in understanding the phase behavior of colloidal systems [28–53, 139, 140]. The equilibrium phase diagrams of binary hard-sphere mixtures for various size ratios have been extensively explored using simulations [30, 41, 46–48, 50, 53, 139, 141], revealing a number of stable binary crystal structures. However, even for this classical colloidal system, antisite defects have not been considered. Here, we focus our attention on binary hard spheres with a size ratio of  $q = \frac{\sigma_S}{\sigma_L} = 0.82$ , where  $\sigma_{S(L)}$  is the diameter of the small (large) particles. For this size ratio, previous studies have concluded that the phase diagram contains a binary fluid phase, single-component face-centered-cubic (FCC) crystals of both the large and small particles, and a binary crystal phase [53, 139, 141]. The stable binary crystal phase is the  $\text{MgZn}_2$

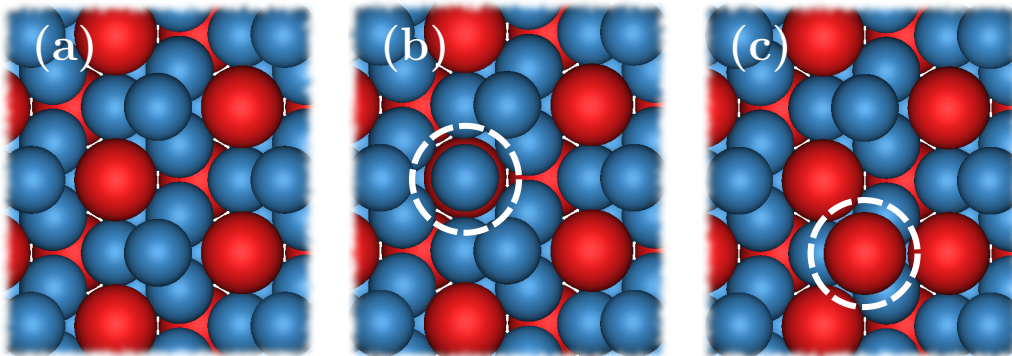


**Figure 4.1:** (a) Ideal  $\text{MgZn}_2$  structure. (b)  $S_L$  antisite defect where a small particle occupies a large-particle lattice site. (c)  $L_S$  antisite defect where a large particle occupies a small-particle lattice site.

Laves phase, with two other Laves phases,  $\text{MgCu}_2$  and  $\text{MgNi}_2$  closely competing [139]. Note that these phases are very similar and differ by the stacking of the large particles. As the  $\text{MgZn}_2$  phase has been shown to be the most stable, we will focus on it in this Chapter, and in the following use the terms  $\text{MgZn}_2$  Laves phase and Laves phase interchangeably.

Of all stable binary hard-sphere crystal structures,  $\text{MgZn}_2$  occurs for size ratios closest to 1, suggesting that switching out a particle in the crystal with one of the opposite species carries a relatively low free-energy cost. Hence, this structure is a prime candidate for exploring the effect of antisite defects on equilibrium phase behavior. Moreover, colloidal Laves phases have drawn considerable attention, due to the interesting photonic properties of the sublattices of the  $\text{MgCu}_2$  phase [53, 142]. Such properties could be affected by the presence of defects.

In this Chapter, we calculate the free energy of FCC and  $\text{MgZn}_2$  hard-sphere crystals as a function of the antisite defect concentration. Combining this free energy with that of the fluid, we redraw the equilibrium bulk phase diagram. The topology of the new phase diagram differs significantly from that of the phase diagram calculated without taking defects into account: while in the defect-free phase diagram, the Laves phase was only stable at one specific composition, in the new phase diagram, the Laves phase covers a range of compositions, all of which are higher than  $2/3$ . This correction arises from a significant concentration of antisite defects, with up to 2% of the large-particle lattice sites occupied by a small particle. This defect concentration is orders of magnitude higher than the vacancy and interstitial defect concentrations found in monodisperse hard-sphere crystals [107, 117].

## 4.2 Model and Methods

### 4.2.1 Free energy of the $\text{MgZn}_2$ Laves phase

Here we consider the Helmholtz free energy of a binary crystal with  $M$  lattice sites,  $N$  particles, volume  $V$ , and temperature  $T$ . In the ideal  $\text{MgZn}_2$  crystal (see Figure 4.1(a)), there is one large particle (denoted  $L$ ) for every two small particles ( $S$ ), and each particle is on a lattice site corresponding to its own species. Here, however, we allow for the inclusion of antisite defects in both directions. Using Kröger-Vink notation, we denote a small particle occupying a large lattice site  $S_L$  and a large particle occupying a small lattice site as  $L_S$ . Figure 4.1(b,c) shows illustrations of both types of defect. The total free energy  $F_{\text{tot}}$  of a crystal containing  $N_{S_L}$  and  $N_{L_S}$  antisite defects of type  $S_L$  and  $L_S$ , respectively, can be written as

$$F_{\text{tot}}(M, V, N_{S_L}, N_{L_S}) = F_0(M, V) + F_d(M, V, N_{S_L}, N_{L_S}) + F_c(M, N_{S_L}, N_{L_S}), \quad (4.1)$$

with  $F_0$  the free energy of the defect-free crystal,  $F_d$  the free-energy cost of introducing  $N_{S_L}$  and  $N_{L_S}$  defects at specific lattice sites, and  $F_c$  the combinatorial free energy resulting from the entropy of distributing these defects over all possible locations in the lattice. Since all free energies in a hard-sphere system scale trivially with the temperature, we drop the temperature-dependence in our notation. Note that we ignore the possibility of defects other than antisite defects (such as vacancies or interstitials), as these are known to be extremely rare in hard-sphere crystals [107, 117].

The free energy of a defect-free crystal is simply given by

$$F_0(M, V) = M f_0(\rho_M), \quad (4.2)$$

where  $f_0(\rho_M)$  is the free energy per particle of a defect-free lattice at density  $\rho_M = M/V$ . The free energy per particle of the defect-free crystal can be obtained for any given density  $\rho_M$  using

$$f_0(\rho_M) = f_0(\rho_M^r) + \int_{\rho_M^r}^{\rho_M} \frac{P_0(\rho'_M)}{(\rho'_M)^2} d\rho'_M, \quad (4.3)$$

where  $P_0(\rho_M)$  is the pressure, which we measure in standard event-driven molecular dynamics (EDMD) simulations [91, 92]. Additionally,  $f_0(\rho_M^r)$  is the Helmholtz free energy per particle at a given reference density of lattice sites  $\rho_M^r$ . For the Laves phases, reference free energies can be found in Ref. [139].

The free-energy cost of introducing defects at specific lattice sites is given by

$$F_d(M, V, N_{S_L}, N_{L_S}) = N_{S_L} f_{S_L}(\rho_M) + N_{L_S} f_{L_S}(\rho_M), \quad (4.4)$$

where  $f_{S_L}$  and  $f_{L_S}$  are the change in free energy upon creating a single  $S_L$ - and  $L_S$ -defect, respectively. These free energies are measured in Monte Carlo simulations, by letting one of the particles fluctuate in size, as we will describe later in this Chapter. Note that in Equation 4.4 we have assumed no interactions between the defects, an assumption expected to hold at sufficiently low defect concentrations. Additionally, it should be noted that the small particles in the  $MgZn_2$  lattice appear in two different local environments, which in principle correspond to different free-energy costs  $f_{L_S}$ . However, since our calculations show that  $f_{L_S}$  is nearly identical for the two local environments, and since  $L_S$ -defects are extremely rare, we ignore this distinction here.

Finally, the combinatorial entropy associated with the distribution of defects over the lattice, again assuming that the defects do not interact, can be written as

$$\beta F_c(M, N_{S_L}, N_{L_S}) = -\ln \left( \frac{M_L!}{(M_L - N_{S_L})! N_{S_L}!} \frac{M_S!}{(M_S - N_{L_S})! N_{L_S}!} \right) \quad (4.5)$$

with  $M_L = \frac{1}{3}M$  and  $M_S = \frac{2}{3}M$  the number of large-particle and small-particle lattice sites, respectively, and  $\beta = 1/k_B T$  with  $k_B$  Boltzmann's constant and  $T$  the temperature.

## 4.2.2 Free energy of the FCC crystals

In addition to the antisite defects in the  $MgZn_2$  crystals, it is also possible that “substitutional” defects are present in the FCC crystals. Specifically, as the system is by definition a mixture of large and small particles, it is possible for the FCC crystal of the large particles to include substitutional defects where a small particle replaces a large particle. Similar defects occur for the FCC crystal of small particles.

Hence, along the same lines as the derivation for the Laves free energy, we derive an expression for the Helmholtz free energy  $F_{\text{tot}}$  of a FCC crystal with  $M$  lattice sites,  $N$

particles, volume  $V$ , in which substitutional defects are present. In the following  $N_{\text{sub}}$  will refer to the number substitutional defects. The total free energy  $F_{\text{tot}}$  of a crystal containing  $N_{\text{sub}}$  substitutional defects can be written as:

$$F_{\text{tot}}(M, V, N_{\text{sub}}) = F_0(M, V) + F_d(M, V, N_{\text{sub}}) + F_c(M, N_{\text{sub}}) \quad (4.6)$$

with  $F_0$  the defect-free free energy,  $F_d$  the free-energy cost of creating  $N_{\text{sub}}$  defects at specific lattice sites, and  $F_c$  the combinatorial free energy associated with the number of possible realizations of distributing the defects inside the lattice. Note that we again assume no interactions between the defects.

The base free energy is given by

$$F_0(M, V) = Mf_0(\rho_M), \quad (4.7)$$

where  $f_0(\rho_M)$  is the free energy per particle of a defect-free lattice at density  $\rho_M = M/V$ , which can be calculated for any given density  $\rho_M$  using Refs. [87, 143, 144].

Next, the total change in free energy associated with the introduction of defects at specific lattice sites is given by

$$F_d(M, V, N_{\text{sub}}) = N_{\text{sub}}f_{\text{sub}}(\rho_M), \quad (4.8)$$

where  $f_{\text{sub}}$  is the change in free energy associated with creating a single substitutional defect at a specific lattice point. This free energy is again measured in Monte Carlo simulations, by letting one of the particles fluctuate in size, analogous to the method described later in this Chapter for the Laves phase.

In order to get the full free energy of a defected crystal where the defect locations are random, we will have to add an additional combinatorial term

$$\beta F_c(M, N_{\text{sub}}) = -\ln \frac{M!}{(M - N_{\text{sub}})!N_{\text{sub}}!}. \quad (4.9)$$

### 4.2.3 Measuring the free energy associated with single defects

We calculate  $f_{\text{S}_L}$  and  $f_{\text{L}_S}$  using Monte Carlo simulations in which we allow a single particle to fluctuate in size over the course of the simulation. More specifically, we perform standard Monte Carlo simulations in the  $NVT$  ensemble in which apart from standard particle moves we also allow the size of a single particle to vary at no energy cost – moves changing the particle size are always accepted if there is no overlap. We start off by initializing an ideal  $\text{MgZn}_2$  crystal, and assign all particles to their corresponding lattice site. In order to prevent the spontaneous creation of additional defects, we confine the particles to their Wigner-Seitz cell by rejecting any particle move that will cause the particle to be closer to any other lattice point than its own. For example, in the case an  $\text{S}_L$ -defect, we allow a single large particle in the crystal to fluctuate in size during the simulation. This allows us to measure the change in free energy associated with changing the size of this specific particle. The free-energy difference  $\Delta F(\sigma_a, \sigma_L)$  between a crystal

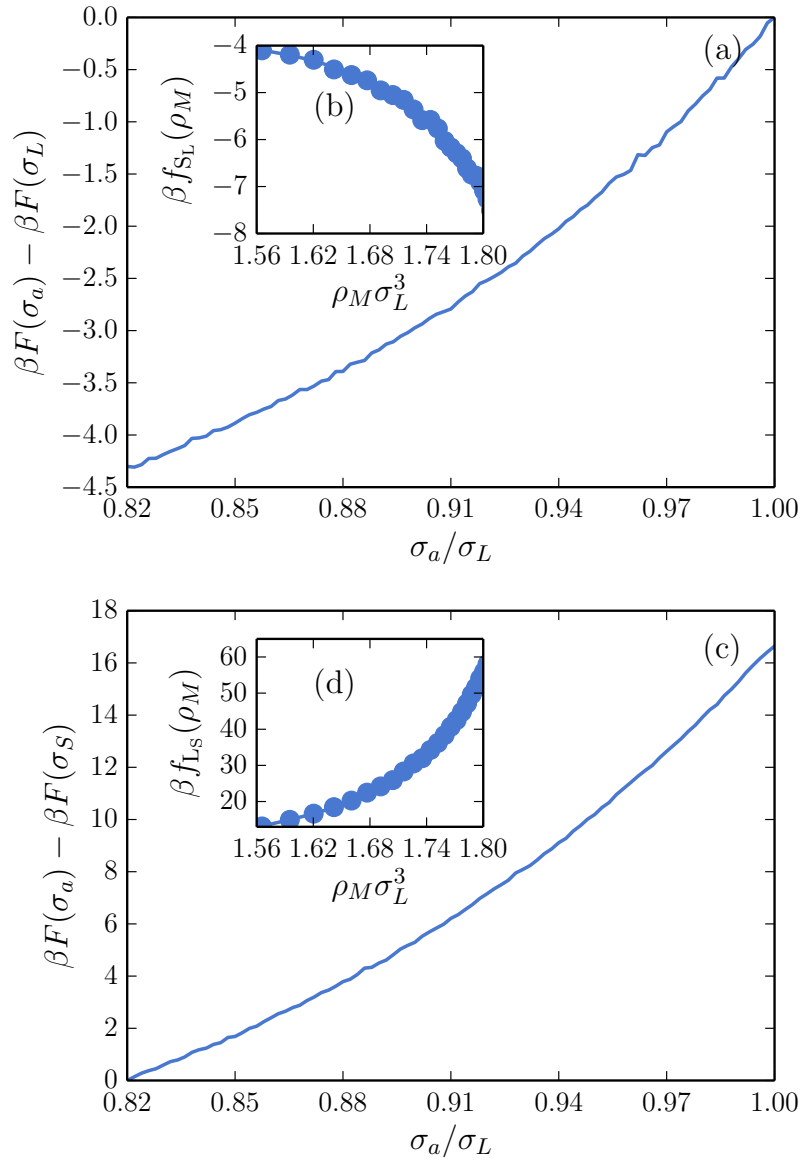


**Figure 4.2:** Defect free energies associated with creating an antisite defect at (a,b) a large-particle lattice site and (c,d) a small-particle lattice site. (a) The free-energy difference associated with shrinking a single large particle to a size  $\sigma_a$ , at a density of  $\rho_M \sigma_L^3 = 1.62$ . (b) The defect free energy  $f_{SL}$  as a function of the density  $\rho_M$ . (c) The free-energy difference associated with growing a single small particle to a size  $\sigma_a$ , at a density of  $\rho_M \sigma_L^3 = 1.62$ . (d) The defect free energy  $f_{LS}$  as a function of the density  $\rho_M$ .

with a particle of actual size  $\sigma_a$  and its nominal size  $\sigma_L$  at a specific lattice site is directly related to the probability  $P(\sigma_a)$  of observing that size in the simulation:

$$\Delta F(\sigma_a, \sigma_L) = F(\sigma_a) - F(\sigma_L) = k_B T \ln \left[ \frac{P(\sigma_L)}{P(\sigma_a)} \right]. \quad (4.10)$$

The free energy associated with substitutional defects in the FCC crystals is calculated using the same approach.

### 4.3 Results

We begin our investigation by examining the free-energy cost associated with the introduction of single defects in the MgZn<sub>2</sub> Laves phase. In Figure 4.2(a), we plot the free-energy difference  $\Delta F(\sigma_a, \sigma_L)$  associated with changing the size of the particle at a specific large-particle lattice site for a density of  $\rho_M \sigma_L^3 = 1.62$ . Note that in order to ensure proper sampling of all possible sizes of the particle we make use of the Wang-Landau biasing method [145]. Following Wang-Landau, we introduce a biasing potential that is optimized during the simulation, that aims to “flatten” the free-energy landscape so that all particle sizes are sampled roughly equally. The free-energy cost of creating a single S<sub>L</sub>-defect is then

$$f_{S_L} = \Delta F(\sigma_S, \sigma_L). \quad (4.11)$$

We can extract this defect free energy  $f_{S_L}$  for a range of densities, as summarized in Figure 4.2(b). For the L<sub>S</sub>-defect, we repeat the same process but allow a small particle to fluctuate in size, with the results plotted in Figure 4.2(c,d). As one might expect, the free-energy cost of shrinking a large particle is negative, while the cost of growing a small particle is positive: the pressure of the surrounding particles favors shrinking of any particle in the crystal. Moreover, the cost of creating an L<sub>S</sub>-defect is much higher than the gain of creating an S<sub>L</sub>-defect, suggesting that simply swapping two particles in the crystal is not a favourable way to create defects. However, introducing excess S<sub>L</sub>-defects has the potential to significantly lower the crystal free energy.

Using Equation 4.1, we can now calculate the full free energy for a crystal at a given density and composition, containing an arbitrary number of S<sub>L</sub>- and L<sub>S</sub>-defects. Moreover, we can calculate the pressure  $P = -\partial F_{\text{tot}}/\partial V$  (at constant defect concentration) at each state point, giving us access to the Gibbs free energy  $G = F + PV$  as well. Note that comparing the pressure derived from  $F_{\text{tot}}$  perfectly matches the pressure measured directly in simulations containing explicit defects. Specifically, in Figure 4.3, we compare the pressure of defected MgZn<sub>2</sub> crystals, as measured in event-driven molecular dynamics (EDMD) simulations [91, 92], to those predicted from our free-energy calculations, for different concentrations of S<sub>L</sub>-defects. Clearly, we observe excellent agreement between the two approaches, confirming the validity of our assumption that the defects do not interact.

We now turn our attention to the relative concentrations of S<sub>L</sub>- and L<sub>S</sub>-defects. In principle, even when the volume  $V$ , and the number of lattice sites  $M$  are held constant, a given composition  $x$  can be realized in a number of different ways:

$$x = \frac{2}{3} + \frac{N_{S_L} - N_{L_S}}{N}. \quad (4.12)$$

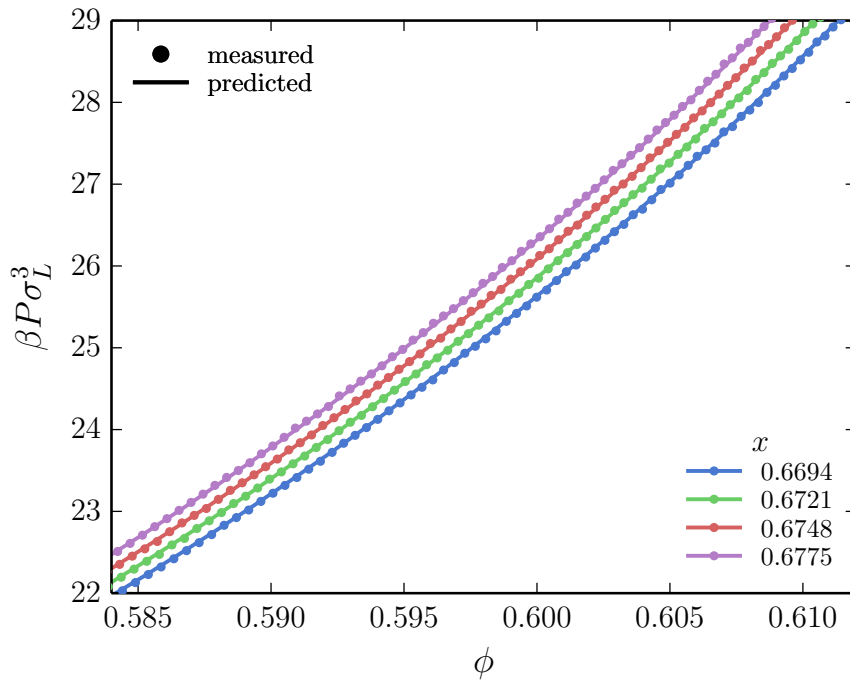


**Figure 4.3:** Comparison of the pressure  $P$  as measured in EDMD simulations (markers) and as obtained from the free energy (lines). Different colors correspond to different concentrations of  $S_L$ -defects, which change the composition of the Laves phase  $x$ . Note that the volume fraction on the x-axis is given by  $\phi = \frac{N\pi}{6V}\sigma_L[(1-x) + xq^3]$ .

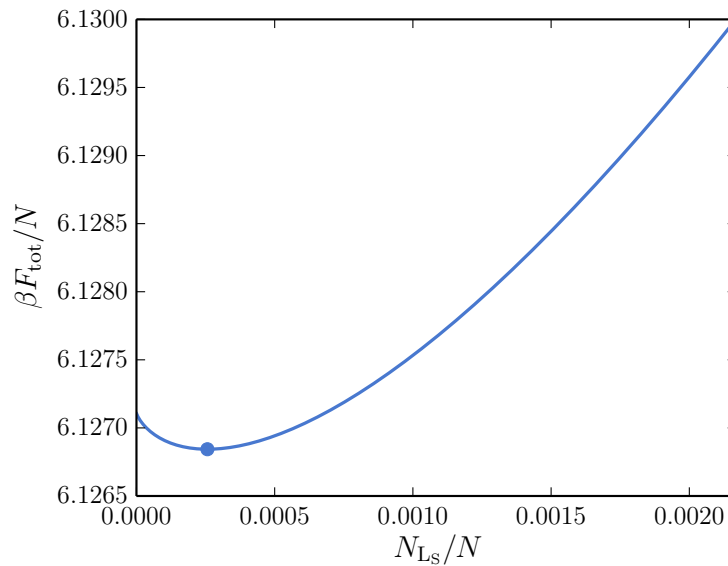


**Figure 4.4:** Helmholtz free energy per particle at a fixed composition  $x = 0.67$ , volume  $V$ , and number of lattice sites  $M$ , as a function of the concentration of  $L_S$ -defects. The minimum in the free energy corresponds to a very low concentration of  $L_S$ -defects and has a negligible effect on the free energy. The density is  $\rho_M \sigma_L^3 = 1.62$ .

Clearly, fixing  $x$  only fixes the *difference* between  $N_{S_L}$  and  $N_{L_S}$ . Since the combination of  $x$ ,  $M$ , and  $V$  determines our state point in the canonical ensemble, the absolute number of defects is a free parameter that is determined by minimizing the Helmholtz free energy.

To estimate the importance of the two types of defects, we plot in Figure 4.4 the Helmholtz free energy per particle at a fixed composition  $x = 0.67$  as a function of the concentration of  $L_S$ -defects. Note that for  $N_{L_S} = 0$ , the composition requires that 1% of large particles are replaced by a small particle. Clearly from Figure 4.4, the concentration of  $L_S$ -defects that minimized the free energy is orders of magnitude smaller than the 1% of  $S_L$ -defects associated with this composition. Moreover, the difference in the free energy between the equilibrium defect concentration and the concentration with no  $L_S$ -defects is less than  $0.0005k_B T$  per particle. Therefore, we can safely ignore  $L_S$ -defects because their concentration is so low, and as such they will have a negligible effect on the free energy (and the phase diagram). Note that this was to be expected considering the high cost in free energy associated with introducing  $L_S$ -defects [Figure 4.2(d)].

In order to predict coexistences between the defected crystal and other phases, we make use of common tangent constructions in the  $(x, g)$  plane, where  $x = N_S/N$  is the composition and  $g = \beta G/N$  is the Gibbs free energy per particle. Note that for the free energy of the fluid, we have used the analytic expression given in Ref. [146]. A typical example of the common tangent construction is shown in Figure 4.5, where we draw the common tangent between the coexisting fluid and Laves phase at a fixed pressure  $\beta P \sigma_L^3 = 23.3$ . In gray, we plot the common tangent without taking antisite defects into account, resulting in a coexistence between a perfect crystal  $x = 2/3$  and a binary fluid. However, taking into account the antisites defect (black dashed line), the composition of the coexisting Laves phase shifts to  $x = 0.672$ , corresponding to a substantial net concentration of  $S_L$ -defects: around 1.6% of the large-sphere lattice sites are taken up by small particles.

By taking into account defect free energies in both the  $MgZn_2$  Laves phase and FCC phases we can map out the phase diagram, as corrected for the possibility of antisite defects. We plot this “updated” phase diagram in Figure 7.3, and provide a zoom-in of the Laves phase region in Figure 7.3(b). Unlike in Refs. [53, 139], where the Laves phase manifests itself as a single line at  $x = 2/3$  on the phase diagram, the Laves phase in the new phase diagram is stable over a narrow but finite region. Strikingly, the composition of the Laves phase can be significantly higher  $x \approx 0.6733$  than the ideal composition. This corresponds to 2.0% of the large particles being substituted by small particles. In contrast, our calculations show that the concentration of  $L_S$ -defects is negligible, being orders of magnitude smaller than the concentration of  $S_L$ -defects in the region where the Laves crystal is stable [Figure 4.4]. We would like to point out that the maximum defect concentration of 2.0% is orders of magnitude higher compared to typical vacancy and interstitial concentrations in single-component hard spheres [107, 117].

Aside from a high  $S_L$ -defect concentrations, our phase diagram exhibits a few other interesting features. Firstly, for the fluid-Laves region our updated phase diagram reveals that at low pressures the  $S_L$ -defect concentration *increases* with pressure. This is uncommon as usually the free energy associated with the formation of defects increases strongly with pressure, resulting in lower defect concentrations [117]. Secondly, we find that at pressures  $\beta P \sigma_L^3 < 30$  the Laves phase is thermodynamically unstable at its ideal compo-

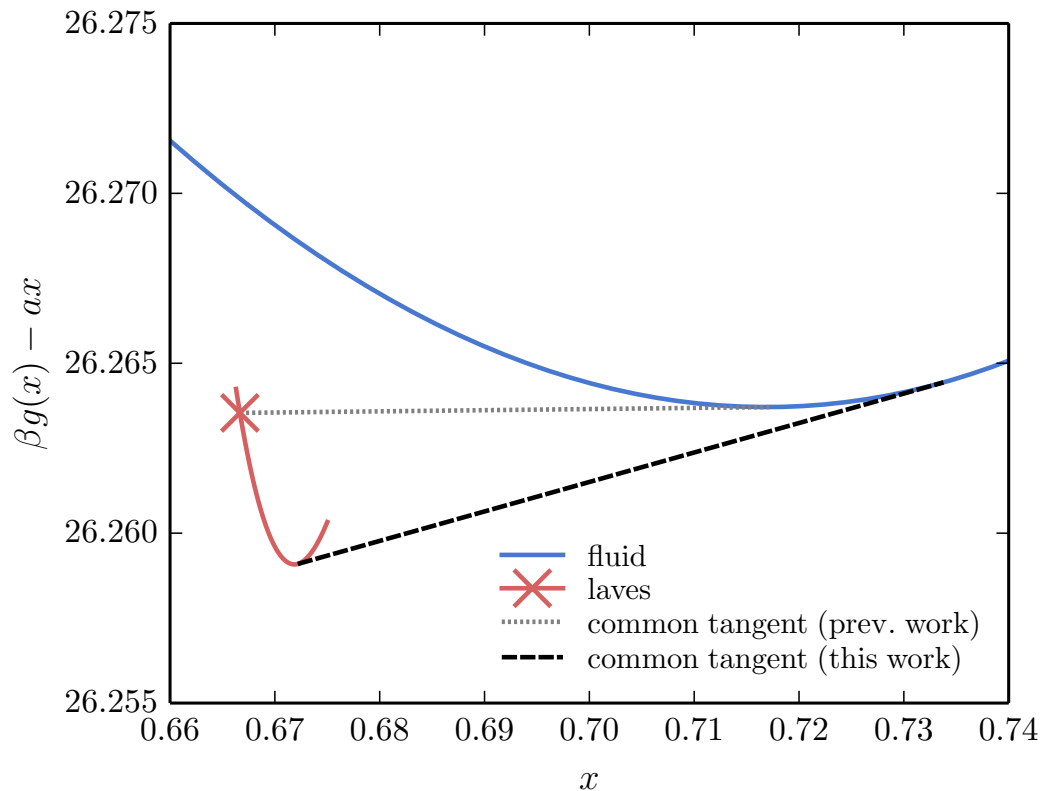


**Figure 4.5:** Effect of taking antisite defects into account on the common tangent construction between the fluid and Laves phase. Specifically, we plot the Gibbs free energy per particle  $g = G/N$  as a function of the composition  $x$  at  $\beta P\sigma_L^3 = 23.3$ . A linear shift has been subtracted here to aid the visualization of the common tangent construction. When only the ideal Laves composition ( $x = 2/3$ ) is taken into consideration the common tangent between the fluid and Laves phase manifests itself as the horizontal line, as was used in previous work [53, 139]. However, upon taking into consideration the Laves phase for a range of composition it becomes clear that the common tangent is changed significantly. Note that in this plot the free-energy differences between different compositions appear a lot smaller than they are in reality due to the subtraction of a linear shift  $ax$ .

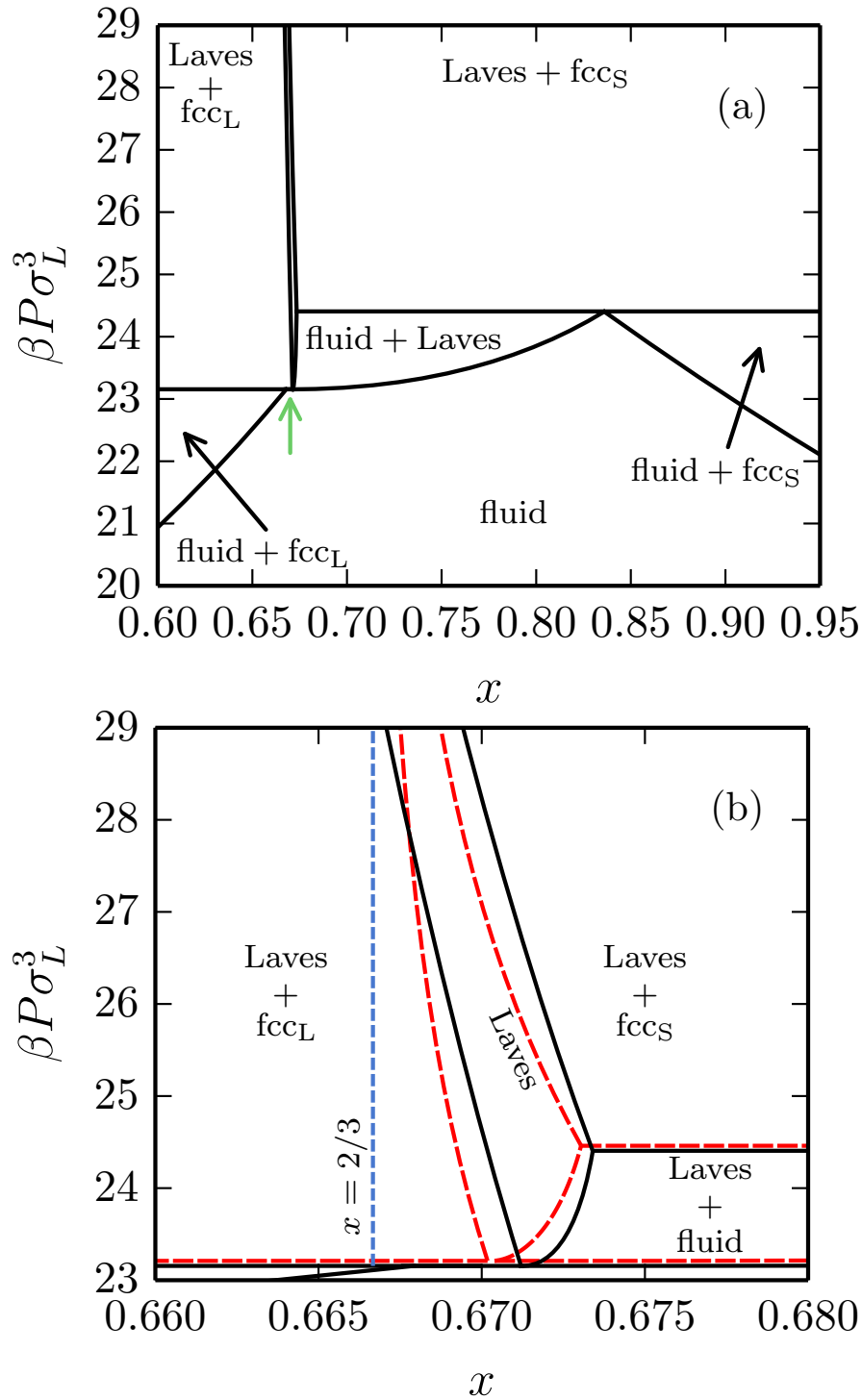


**Figure 4.6:** (a) Revisited phase diagram for a binary hard-sphere mixture with a size ratio of  $q = 0.82$  upon taking defects into account in both the Laves phase and fcc phases. (b) Zoomed-in section on the Laves region. The dashed blue line corresponds to composition of the ideal crystal ( $x = 2/3$ ). The dashed red lines corresponds to the binodals as obtained by using Equation 4.17. Note that there is an extremely small Laves + fluid region at the tip of the green arrow in (a) that is not visible on either of the pressure scales displayed here, as the pressure range of the region is  $\beta P \sigma_L^3 = 0.002$  [141].

sition  $x_{id} = 2/3$  with respect to phase separation between a large-particle FCC phase and a Laves phase containing antisite defects. This might have important repercussions for future studies of the Laves phases, in particular studies into the dynamics or nucleation.

Lastly, we would like to show a convenient, yet more approximate way to take these defects into account. To this end, we consider a binary crystal at constant pressure  $P$ . We now make the approximation that introducing antisite defects has no effect on the equation of state, and again assume that the defects do not interact. In order to allow for the creation of  $S_L$ -defects, we put the crystal in contact with a particle reservoir (e.g. a coexisting fluid) with  $N_S^{\text{res}}$  and  $N_L^{\text{res}}$  small and large particles, respectively. Note that we only allow the direct exchange of large and small particles between the crystal and the reservoir, so that the total number of particles in each system remains fixed.

The Gibbs free energy of the full system (crystal plus reservoir), can be written as:

$$G_{\text{sys}}(N_S, N_L, N_{S_L}, P) = G_{\text{crys}}(N_S^{\text{crys}}, N_L^{\text{crys}}, P) + G_{\text{res}}(N_S^{\text{res}}, N_L^{\text{res}}, P). \quad (4.13)$$

Here,  $N_{S(L)}^{\text{crys}}$  and  $N_{S(L)}^{\text{res}}$  denote the number of small (large) particles in the crystal and reservoir, respectively, and  $N_{S(L)} = N_{S(L)}^{\text{crys}} + N_{S(L)}^{\text{res}}$  is the total number of small (large) particles. Creating an antisite defect corresponds to exchanging a large particle in the crystal for a small particle from the reservoir. We want to minimize the total Gibbs free energy with respect to  $N_{S_L}$ . For the reservoir, we can then write:

$$\begin{aligned} \left( \frac{\partial G_{\text{res}}(N_S^{\text{res}}, N_L^{\text{res}}, P)}{\partial N_{S_L}} \right)_{N_S, N_L, P} &= \\ - \left( \frac{\partial G_{\text{res}}(N_S^{\text{res}}, N_L^{\text{res}}, P)}{\partial N_S^{\text{res}}} \right)_{N_S, N_L, P} + \left( \frac{\partial G_{\text{res}}(N_S^{\text{res}}, N_L^{\text{res}}, P)}{\partial N_L^{\text{res}}} \right)_{N_S, N_L, P} &= -\mu_S + \mu_L. \end{aligned} \quad (4.14)$$

Here we have used  $\left( \frac{\partial N_S^{\text{res}}}{\partial N_{S_L}} \right)_{N_S, N_L, P} = -1$ , and  $\left( \frac{\partial N_L^{\text{res}}}{\partial N_{S_L}} \right)_{N_S, N_L, P} = 1$ .

For the crystal, we Legendre-transform the Gibbs free energy:

$$\begin{aligned} G_{\text{crys}}(N_S^{\text{crys}}, N_L^{\text{crys}}, P) &= F_{\text{crys}}(N_S^{\text{crys}}, N_L^{\text{crys}}, V) + PV \\ &= M f_0(\rho_M) + N_{S_L} f_{S_L}(\rho_M) - k_B T \ln \left( \frac{M_L!}{(M_L - N_{S_L})! N_{S_L}!} \right) + PV, \end{aligned} \quad (4.15)$$

where  $M = N_S^{\text{crys}} + N_L^{\text{crys}}$  and  $\rho_M = M/V$  is the density of the defect-free crystal at pressure  $P$ . Assuming that the defects do not affect the equation of state of the crystal,  $\frac{\partial(PV)}{\partial N_{S_L}} = 0$ . Hence, the derivative of  $G_{\text{sys}}$  is given by

$$\left( \frac{\partial G_{\text{sys}}(N_S, N_L, N_{S_L}, P)}{\partial N_{S_L}} \right)_{N_S, N_L, P} = g_{S_L} - k_B T \frac{\partial}{\partial N_{S_L}} \ln \left( \frac{M_L!}{(M_L - N_{S_L})! N_{S_L}!} \right) \quad (4.16)$$

where  $g_{S_L} = f_{S_L} + \mu_L - \mu_S$  is the Gibbs free-energy cost of creating a defect at a specific lattice site. Applying Stirling's approximation and minimizing with respect to  $N_{S_L}$  yields

$$\frac{N_{S_L}}{M_L} \simeq \exp(-\beta g_{S_L}), \quad (4.17)$$

which provides a straightforward estimate of the effect of defects on the composition of the binary crystal.

To test to what extent this approach can be used to predict whether or not antisite defects are important, we have estimated the equilibrium defect concentration for the Laves-fluid as well as the Laves-FCC coexistences. Specifically, for the chemical potential difference we have used the slope of the common tangent between the Laves phase of ideal composition, and the fluid or pure FCC phases. Note that this is the same common tangent construction as was used in Refs. [53, 139]. In Figure 7.3(b), we superimpose the binodals as obtained from this approximate method. Clearly, this first-order correction to the data presented in Refs. [53, 139] captures the essential traits of our “updated” phase diagram. Specifically, we predict a similarly high concentration of defects. It also captures the atypical defect concentration increasing with pressure in the fluid-Laves region, as well as the Laves phase being unstable at its ideal composition. The fact that these approximate binodals agree relatively well with our phase diagram suggests a simple way to estimate the importance of antisite defects on a given coexistence.

## 4.4 Discussion and Conclusions

In conclusion, we have re-calculated the phase diagram for binary hard spheres with a size ratio of  $q = 0.82$  by taking into consideration antisite defects in the  $\text{MgZn}_2$  Laves phase and substitutional defects in the FCC crystals. The topology of this new phase diagram differs significantly from that of the phase diagram calculated in Refs. [53, 139] where defects were not taken into account: while in the defect-free phase diagram, the Laves phase could only occur at its ideal composition ( $x = 2/3$ ), in the new phase diagram, the Laves phase covers a range of compositions, all of which are higher than  $2/3$  at intermediate pressures. This correction arises from a significant concentration of antisite defects. In fact, we find stable regions where up to 2% of the large-particle lattice sites are occupied by a small particle. This defect concentration is orders of magnitude higher than the vacancy and interstitial defect concentrations found in monodisperse hard-sphere crystals [107, 117].

Hence, the commonly made assumption in the calculation of phase diagrams that the crystal composition is ideal is not valid here. To date, these types of defects have not been considered in any of the binary hard-sphere crystal studies [46–48, 50, 53, 139], nor in any colloidal binary phase diagram studies that we are aware of. While we have focussed in this Chapter only on the Laves phase and FCC crystals, we like to stress that the assumption of ideal crystal composition has also been made for the calculation of phase diagrams of binary hard spheres which show regions of stability of e.g.  $\text{NaZn}_{13}$ ,  $\text{AlB}_2$ . As these crystals appear at more extreme size ratios, it might even be necessary to consider defects in which multiple small spheres take up the space of a single large sphere.

We also provided a more approximate method to take into account the effect of defects on the phase diagram. This simple approach captured the essential traits of the “updated” phase diagram. Specifically, it predicted a similarly high concentration of defects. It also captured the atypical defect concentration that increased with pressure in the fluid-Laves region, as well as the pressure range over which the Laves phase is unstable at its ideal

composition. The fact that the approximate phase diagram agrees well with our phase diagram suggests that this method would be an excellent starting point for future studies when it comes to correcting the phase diagrams which show regions of stability for other binary crystal structures.

Lastly, much of the research on the Laves phases in colloidal crystals has been motivated by the possibility of a complete band gap in the visible part of the spectrum, associated with the sublattices in the  $\text{MgCu}_2$  crystal [53, 142]. The high concentration of antisite defects we have found in the Laves phase with the  $\text{MgZn}_2$  structure, is also very likely to play an important role in the other, metastable Laves phases with the  $\text{MgCu}_2$  and  $\text{MgNi}_2$  structures. Hence, high defect concentrations may affect the photonic band gap of the metastable  $\text{MgCu}_2$  Laves phase, as it is well known that already low concentrations of defects can deteriorate the performance of band-gap materials. As these defects are an inherent part of the crystal phase behavior, removing them may be a considerable challenge.

## 4.5 Acknowledgements

I would like to thank Frank Smalenburg for his contribution to the derivation of the expression for the free energy of the defected crystals, and both him and Michiel Hermes for many useful discussions.

---

## Revealing a vacancy analogue of the crowdion interstitial in simple cubic crystals

---

Vacancies in simple cubic crystals of hard particles have been shown to be able to delocalize over chains of several lattice sites. In this Chapter, we use event-driven molecular dynamics and Monte Carlo simulations to explore the structure and dynamics of these defects in crystals of hard cubes and hard right rhombic prisms (slanted cubes). We show that they form a vacancy analogue of the interstitial crowdion. In particular, these “voidions” generate a strain-field which follows a soliton solution of the sine-Gordon equation, and show diffusive behavior following a persistent random walk. Surprisingly, the structure of the vacancies is largely independent of the system density, defect concentration, particle shape, and particle interactions, strongly suggesting that voidions are an inherent feature of simple cubic crystals of repulsive particles.

## 5.1 Introduction

Many material properties of crystals are determined by the formation and diffusion of small collections of point defects inside the lattice. In crystals consisting of spherical particles, these point defects are typically fairly localized, primarily affecting the location of only a few particles, and diffuse inside the crystal through hopping motions. Therefore, imagining a point defect as localized to one specific lattice point is fundamentally correct in many cases, and forms a crucial ingredient in theories of solid-state self-diffusion [147].

Yet, in some cases point defects take on forms that are significantly extended in space, such as the interstitial crowdion, which was proposed by Paneth in the 1950s [148]. Here the lattice distortion due to the interstitial particle is largely one-dimensional, displacing particles in a chain along a specific lattice direction, which can extend over a large number of lattice sites. These crowdion defects have been shown to exhibit fundamentally different diffusion properties compared to their localized counterparts [149, 150], and have triggered the formulation of simple models that can capture their essential traits [151–155]. Specifically, one interesting trait of the crowdion defect is that the displacements of the particles in the defect are essentially one-dimensional and can be accurately captured by the Frenkel-Kontorova model [151, 155], which in the continuum limit reduces to the sine-Gordon equation. Recent experimental work has hinted that a vacancy-equivalent of this extended configuration, called an “anti-crowdion” [152] or a “voidion” [156], may exist in metals, where  $N - 1$  particles are spread over  $N$  lattice sites in a chain [156]. However, as the atomic structure around these extended defects is typically not accessible in experiments it remains unclear whether these voidions exist, and to what extent they are related to crowdions.

Hard colloidal particles with different shapes have emerged as an excellent model system for exploring crystalline phase behavior (e.g. [27, 60–63, 98, 157–171]). An intriguing family of such colloidal model systems was shown to form crystals containing extended vacancy defects [169–171]. Although particles in this family have a variety of shapes and symmetries, including cubes, truncated cubes, and right rhombic prisms (“slanted cubes”, see Figure 5.1), they all form a simple cubic crystal phase with an abnormally high defect concentration, orders of magnitude higher than that of the archetypical hard-sphere crystal [107]. The presence of these defects has a profound effect on the crystal dynamics close to melting, resulting in self-diffusion rates as high as 30% of those in the corresponding fluid [169]. Both the delocalization and high diffusivity of these vacancies are strongly reminiscent of interstitial crowdions, suggesting that they may be a direct realization of the hypothesized voidion.

To test this hypothesis, in this Chapter we use computer simulations to examine the structure and dynamics of point defects in simple cubic crystals formed by hard cubes and slanted cubes. We show that both vacancies and interstitials are characterized by a strain field closely following the sine-Gordon equation, and hence are colloidal realizations of voidions and crowdions. Additionally, we show that the diffusion of the vacancies follows a persistent random walk along the lattice lines of the crystal, similar to the dynamics of crowdions [149, 150]. Finally, we demonstrate that the structure of the voidions is not significantly affected by changes in density, vacancy concentration, and even particle

interaction, suggesting that they are a robust phenomenon in systems of repulsive particle forming simple cubic crystals.

## 5.2 Model and Methods

### 5.2.1 Simulation details

Using computer simulations, we investigate simple cubic crystals of cubes and slanted cubes with slant angle  $\theta = 72^\circ$  (see Figure 5.1), whose interactions are assumed to be purely due to excluded volume (i.e. overlaps between particles are not allowed). Specifically, we perform Monte Carlo (MC) and event-driven molecular dynamics (EDMD) simulations [91, 169, 172] of three-dimensional crystals of  $N$  particles containing their net equilibrium concentration of vacancies  $\alpha = \frac{N_L - N}{N_L}$ , where  $N_L$  is the number of lattice sites. These vacancy-rich crystals are initialized by distributing the vacancies randomly throughout the crystal. Note that in principle, additional vacancy-interstitial pairs can form which increases the total number of vacancies. The net equilibrium vacancy concentration is taken from previous free-energy calculations presented in Refs. [169, 171].

### 5.2.2 The tracking algorithm

#### Location of defects

As a first step to locating the point defects in our crystals we compare the particle positions in the system to a simple cubic lattice. Specifically, we find out which Wigner-Seitz cells in the crystal are occupied by zero, one, or two particles. Wigner-Seitz cells that contain no particle correspond to a vacancy and Wigner-Seitz cells that contain two particles correspond to an interstitial.

Typically, this simple routine already gives quite a good estimation of the positions of vacancy and interstitial centers in our system. However, thermal fluctuations occasionally lead to the particles moving slightly out of their Wigner-Seitz cell into a neighbouring cell. This is detected as a (very short-lived) vacancy-interstitial pair, even though no stable

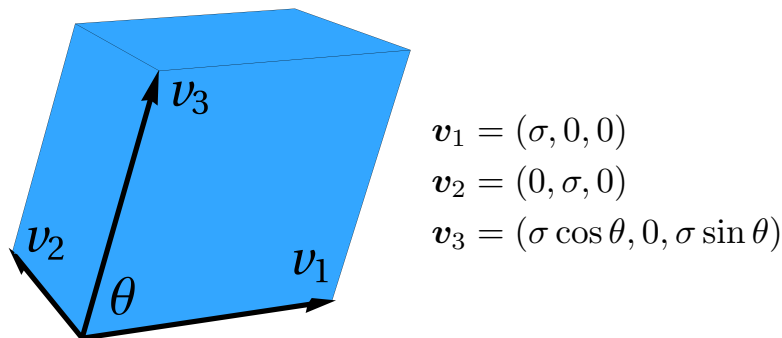


**Figure 5.1:** A slanted cube and the vectors by which it is defined.

defect has formed. To this end, we remove vacancies and interstitials that are adjacent to each other, by letting this vacancy and interstitial pair cancel out.

### Orientation of defects

We determine the orientation of a vacancy by looking at the displacements of particles towards the vacant lattice site. Note that vacancies only tend to spread along the three major axes of the crystal. A vacancy is considered to be oriented along a certain direction if the particles directly adjacent to the vacancy are separated by less than two particle dimensions  $\sigma$ . In this case, the vacancy can only spread along this direction as in the other direction the passage is blocked. If this holds for none of the three directions, we take the direction where the neighboring particles have displaced most towards the vacant lattice point.

### Length of defects

We determine the length of a vacancy by looking at the displacements along the direction of the vacancy. Particles that are part of the extended vacancy have displaced away from their lattice point towards the vacancy center. We attribute a particle to the extended vacancy if the particle has displaced more than  $\delta^* = 0.5(a - \sigma)$  towards the vacancy center, where  $a$  is the lattice spacing. Similarly, particles are considered to be part of an extended interstitial if they have displaced more than  $\delta^*$  away from the interstitial center. The extended defect includes all particles on both sides up to the first particle in the chain that has displaced less than  $\delta^*$  towards the vacancy center (or away from the interstitial center).

## 5.3 Results

### 5.3.1 Particle displacements associated with point defects

We begin our investigation by characterizing the displacement field of particles around defects in equilibrium crystals of cubes and slanted cubes with slant angle  $\theta = 72^\circ$ , whose interactions are assumed to be purely due to excluded volume. In each simulation, we track the defects, their length, and their orientation by examining the occupancy of Wigner-Seitz cells in the crystal. Examples of a vacancy and an interstitial are shown in Figure 5.2(a,b). Clearly in both cases, the defect is extended over a long chain of lattice sites. Note that the number of vacancies is much larger than the number of interstitials in these systems. To provide a better image of the distribution of defects in a crystal, Figure 5.2(c) shows all vacancies in a typical crystal of hard cubes, illustrating that the defects are delocalized with random orientations and positions. We will address later the interactions between the defects in more detail.

One important characteristic of a crowdion defect is that the displacements of the particles in the defect are essentially one-dimensional and can be accurately captured by the Frenkel-Kontorova model [151, 155], which in the continuum limit reduces to the

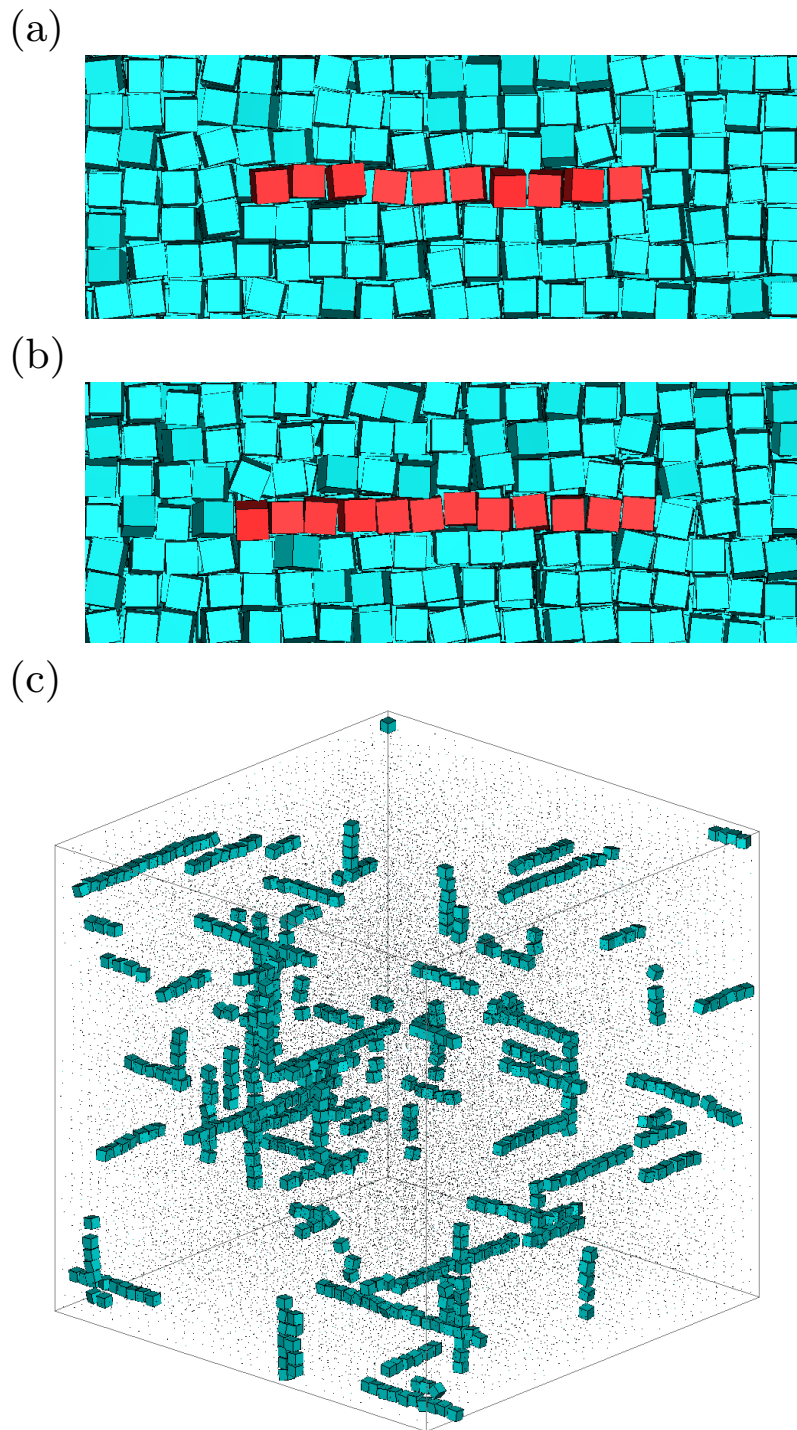


**Figure 5.2:** (a) Typical local structure of a vacancy delocalized over a chain of particles (red) at  $\phi = 0.65$ , and of an interstitial extended over a chain of particles (red) at  $\phi = 0.60$ . (c) Tracking results revealing the position, direction and length of extended vacancies in a crystal of hard cubes at  $\phi = 0.65$ . Particles that are part of a vacancy are shown at their actual size while the other particles are shown much smaller.

sine-Gordon equation:

$$u^\pm(x) = \frac{2a}{\pi} \arctan [\exp (\pm \mu(x - x_0))], \quad (5.1)$$

where  $u^+$  is the vacancy (anti-kink) and  $u^-$  is the interstitial (kink). To check how well this holds for the defects in our systems, we calculate the average particle displacements  $u_n = x_n - an$  around vacancies and interstitials, along the defect direction, where  $x_n$  is the position of particle  $n$  along the chain of particles in the defect. We choose  $n = 0$  to correspond to the particle just before the defect center and use “standard” boundary conditions:  $u_{n=-\infty}^- = a$ ,  $u_{n=\infty}^- = 0$  and  $u_{n=-\infty}^+ = 0$ ,  $u_{n=\infty}^+ = a$ . We plot these displacement fields for a system of hard cubes at packing fraction  $\phi = 0.60$  in Figure 5.3(a), where  $\phi = Nv_0/V$  with  $v_0$  the volume of the particle and  $V$  the volume of the system. We compare our results to the soliton solution of the Frenkel-Kontorova model (black lines). We observe excellent agreement for the interstitial defects, where the displacement field closely follows the theoretical line. This agreement is particularly remarkable since the Frenkel-Kontorova model assumes harmonic interactions between all particles, while the interactions between hard cubes are strongly anharmonic. This is likely due to the extremely extended nature of the defect. Indeed, for the shorter vacancy defects, we also see good agreement, but observe small deviations in the particles closest to the empty lattice site. We conclude that the interstitials in our system manifest as crowdions, and argue that the vacancies appear as the crowdion-equivalent for vacancies, namely the hypothesized “voidions”.

As vacancies are the predominant type of defect in these crystals, in the following we focus on the properties of the voidions. In Figure 5.3(b), we plot the average displacement field around a vacancy for both cubes and slanted cubes (with slant angle  $\theta = 72^\circ$ ) at several packing fractions. Surprisingly, the displacement fields for the different packing fractions  $\phi$  and for the two particle shapes collapse onto a single curve when the displacements are normalized with respect to the lattice spacing  $a$ . Hence, for these particles, the length of a point defect does not seem to depend on the packing fraction  $\phi$  nor the shape of the particle.

The displacement fields shown in Figure 5.3(b) suggest an average length of the vacancy of around 10 particles. However, as shown in Figure 5.2(c), the defects show a large variation in length. To explore this, we plot the probability distribution of instantaneous vacancy lengths  $P(L)$ , defined as the number of particles that are part of the vacancy, in Figure 5.3(c). The  $P(L)$  curves for different  $\phi$  again collapse unto a single curve, indicating that the length distribution of the vacancies is independent of the packing fraction. Moreover, the length of the vacancy is also independent of the slant angle, i.e. the vacancies we find in systems of cubes (circle markers) and slanted cubes with  $\theta = 72^\circ$  (triangle markers) have identical length distributions.

Thus far, we have performed all measurements in crystals containing their equilibrium concentration of defects. As interactions between defects could in principle play an important role in determining their structure, we now investigate the properties of isolated defects. To this end, we perform MC simulations in which each particle is constrained to its Wigner-Seitz cell, and introduce a single vacancy by leaving one of the lattice sites empty. Using these constraints, the vacancy cannot diffuse, nor can additional vacancy-interstitial pairs form. Using these simulations, we again analyze the length distribution

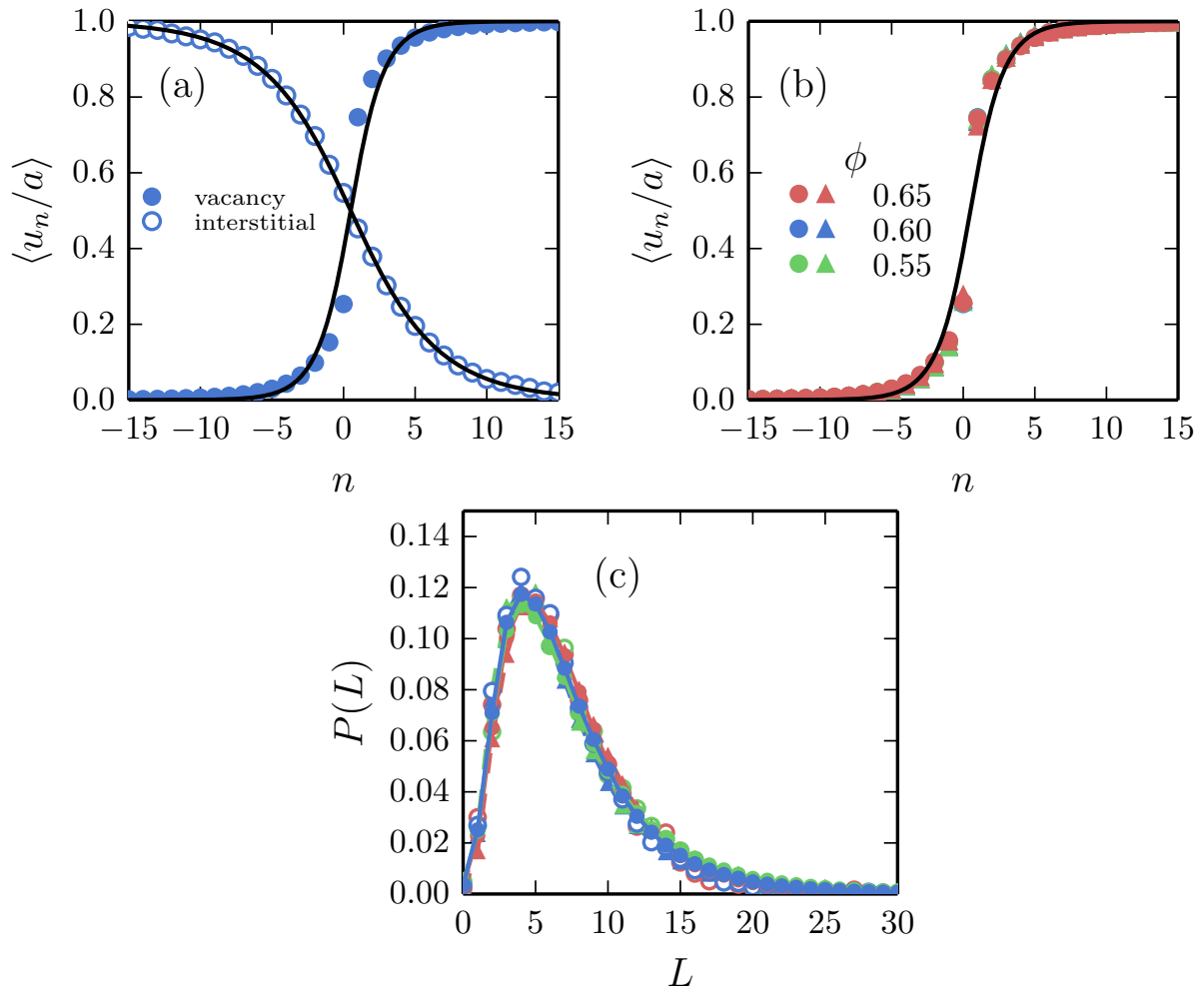


**Figure 5.3:** (a) Averaged displacement field  $\langle u_n \rangle$  along the vacancy (solid markers) and the interstitial (open marker) for a hard-cube system at  $\phi = 0.60$ . The displacements inside these defects follow the sine-Gordon equation (black lines). (b) Averaged displacement field along the vacancy at different  $\phi$  for cubes (circles) and “slanted” cubes with an angle of  $72^\circ$  (triangles). (c) Probability distribution of instantaneous vacancy lengths  $P(L)$  with  $L$  the number of particles at different packing fractions  $\phi$  for cubes (circles) and “slanted” cubes with an angle of  $72^\circ$  (triangles) using the EDMD simulations (solid markers), and the single vacancy MC simulations (open markers).

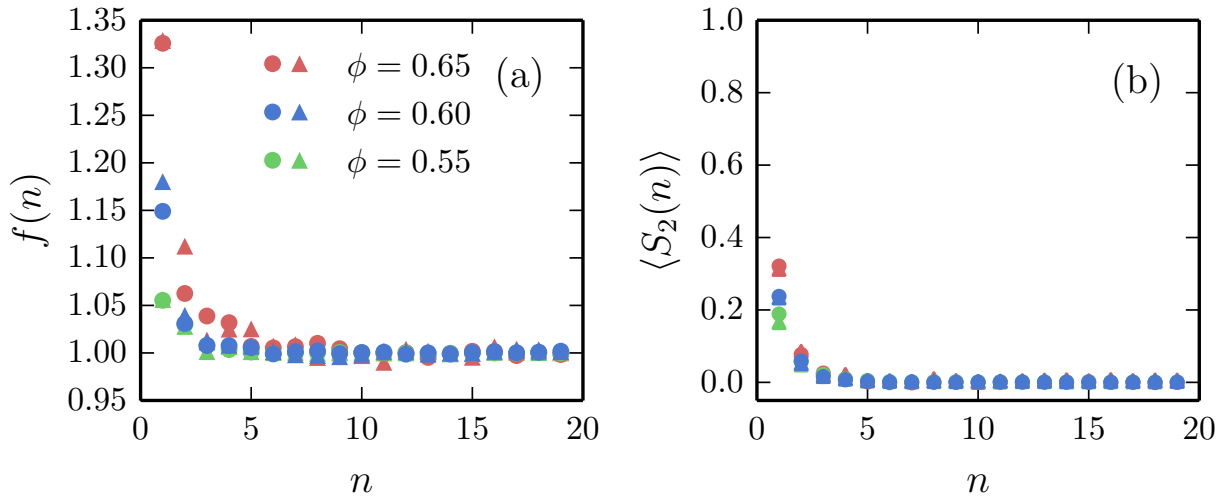


**Figure 5.4:** (a) Normalized vacancy density  $f(n)$  at a distance of  $n$  cubic shells from another vacancy, for both cubes (circles) and “slanted” cubes with an angle of  $72^\circ$  (triangles). (b) Orientation correlation function  $\langle S_2(n) \rangle$  at a distance of  $n$  cubic shells from another vacancy, for both cubes (circles) and “slanted” cubes with an angle of  $72^\circ$  (triangles).

of the voidions, and find results identical to those of the equilibrium case (Figure 5.3(c)). Hence, we conclude that interactions between defects have no effect on their structure. Interestingly, this opens the door to a fast check on whether vacancies in a given system are capable of delocalizing: one can simply perform a simulation of a crystal with a single defect, and investigate its structure. As delocalized vacancies are correlated with high vacancy concentrations [169–171], the observation of such voidions would be a strong reason to take defects into account when analyzing crystal phase behavior.

### 5.3.2 Interactions between vacancies

At the lowest packing fraction investigated here ( $\phi = 0.55$ ), the equilibrium vacancy concentration is  $\alpha \simeq 0.019$ , and the average length of a vacancy is approximately 8 lattice sites. Hence, the total fraction of lattice sites involved in a vacancy is approximately 15%. Clearly, for this system the usual assumption that vacancies are on average separated by many lattice spacings is not valid, which raises the question of whether these defects interact. In fact, due to their one-dimensional character, we should consider not only attraction and repulsion, but also aligning interactions.

The normalized density of vacancies  $f(n)$  in the  $n^{\text{th}}$  cubic shell around a reference vacancy located at  $n = 0$  is plotted in Figure 5.4(a). Here, we have chosen to bin the vacancy-vacancy separation distances in cubic shells to ensure proper statistics in each bin. Specifically, we normalize the number of vacancies  $N_v(n)$  in a shell  $n$  by the number of lattice sites  $N_L(n)$  in this shell and by the overall vacancy concentration  $\alpha$ :

$$f(n) = \frac{N_v(n)}{\alpha N_L(n)} \quad (5.2)$$

The normalized probability of finding two vacancies at a distance of  $n$  shells from each other is well-approximated by an ideal distribution, i.e.  $f(n) \approx 1$  for all  $n$ . Only immediately adjacent to a vacancy ( $n = 1$ ) do we find slightly elevated concentrations of vacancies (ca. 5-30%). This indicates that the interactions are very short-ranged and weak (effective attractions are on the order of  $0.3 k_B T$ ).

Similarly, to investigate whether adjacent vacancies align, in Figure 5.4(b), we plot the orientation correlation function

$$S_2(n) = \left\langle \frac{3}{2} |\hat{\mathbf{u}}_i(0) \cdot \hat{\mathbf{u}}_j(n)|^2 - \frac{1}{2} \right\rangle, \quad (5.3)$$

where  $\hat{\mathbf{u}}_i(0)$  and  $\hat{\mathbf{u}}_j(n)$  are the orientations of a vacancy at the origin and at a distance of  $n$  shells. Note that  $S_2(n) = 1$  if vacancies are perfectly aligned and 0 if their orientations are uncorrelated. Again, the vacancy orientations are essentially uncorrelated, showing only mild alignment when they are directly adjacent.

### 5.3.3 Diffusion of vacancies

We now turn our attention to the dynamics of the voidions. In Figure 5.5(a), we plot the mean squared displacement as a function of time for the center of the vacancies in crystals of hard cubes at their equilibrium vacancy concentration. Counter-intuitively, the vacancy diffusivity goes up with increasing packing fraction. This is in stark contrast to vacancy diffusion in most systems, where the diffusivity goes down drastically with increasing packing fraction; in most cases, the defect diffusion is well-described by a random walk on the crystal lattice, whose speed is determined by the free-energy barrier associated with each step [Chapter 2]. To explore the diffusion mechanism for the voidions, a trajectory of such a defect is shown in Figure 5.5(b). Clearly, the vacancy diffuses by gliding along the main crystalline lattice directions, and from time to time, reorienting. The gliding process itself requires very little activation energy, and results from the collective displacement of the particles that are part of the voidion, requiring only very small displacements of each constituent particle. Reorienting, on the other hand, requires the vacancy to shrink to a single lattice site, and then regrow in a new direction. This is an activated process that occurs on timescales much slower than the gliding diffusion, resulting in a persistent random walk. Hence, the diffusion in this system is governed by two separate timescales: the one-dimensional diffusion, and the timescale associated with reorientations.

To determine how frequently the voidions reorient, we use the orientational autocorrelation function:

$$S_2(t) = \left\langle \frac{3}{2} |\hat{\mathbf{u}}_i(0) \cdot \hat{\mathbf{u}}_i(t)|^2 - \frac{1}{2} \right\rangle \quad (5.4)$$

with  $\hat{\mathbf{u}}_i(t)$  the time-dependent orientation of a vacancy  $i$  and  $\langle \dots \rangle$  denoting an average over all vacancies and times. We plot  $S_2(t)$  for several packing fractions in Figure 5.5(c). In all cases, the decay of  $S_2(t)$  is roughly exponential:  $S_2(t) = \exp(-t/\tau_{or})$  with  $\tau_{or}$  the timescale of reorientation of a vacancy. This reorientation time increases with packing fraction, implying that the defects glide for longer along the same axis, resulting in a faster overall diffusion. Note that since the equilibrium defect concentration decreases rapidly with packing fraction [169], the total self-diffusivity of the particles in the crystal still slows down with increasing packing fraction.

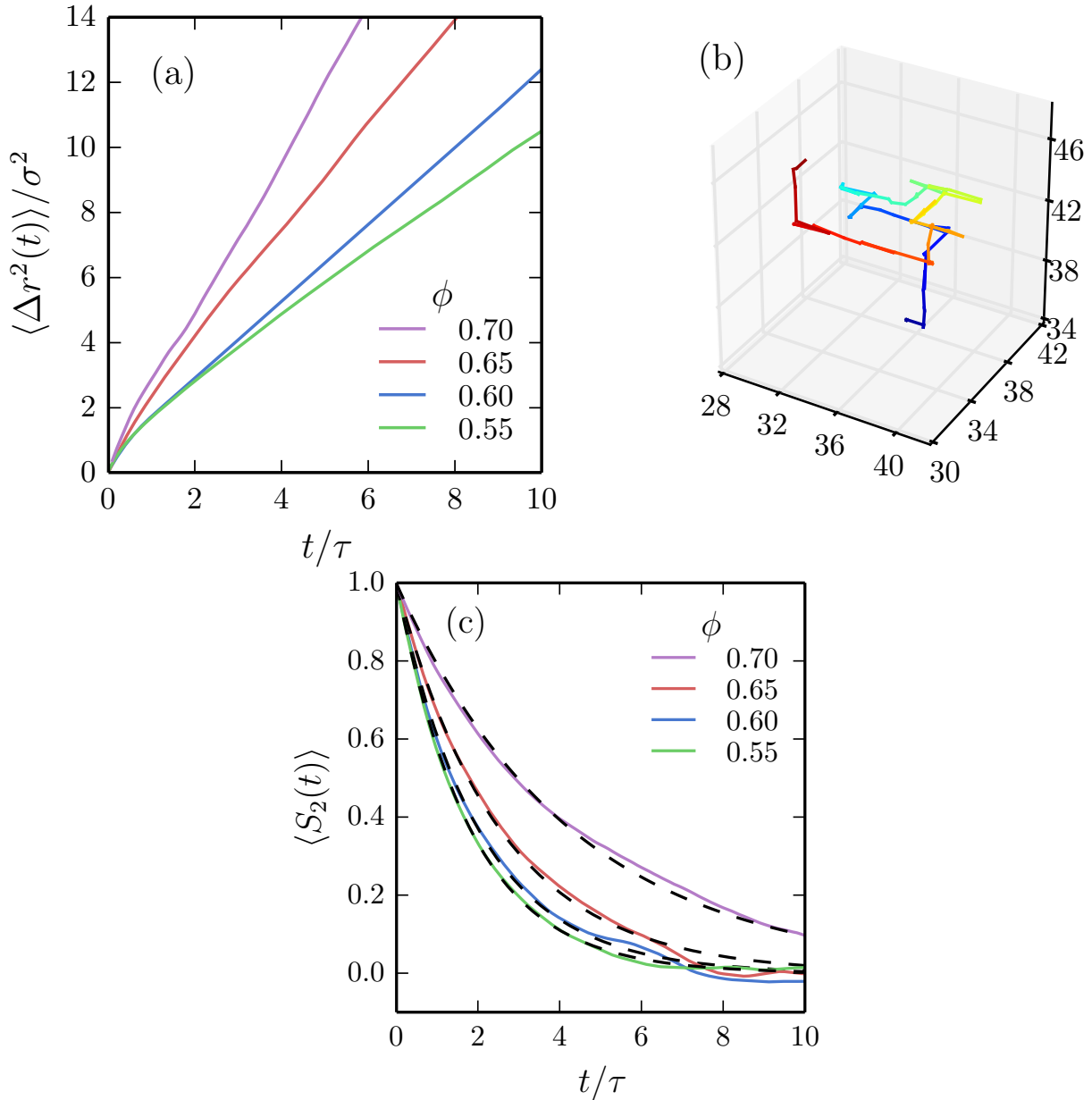


**Figure 5.5:** (a) Mean squared displacement of the center of the vacancies for the hard-cube system at different packing fractions. (b) Trajectory of a diffusing center of the vacancy in the hard-cube system at a packing fraction  $\phi = 0.65$ . (c) The autocorrelation function of the vacancy orientations for the hard-cube system at different packing fractions. Dashed lines correspond to exponential fits.

### 5.3.4 “Voidions” for a system with soft repulsive isotropic interactions

So far, this entire Chapter is focused on crystals of hard anisotropic particles with flat faces, and it might be tempting to assume that this feature is responsible for the delocalization of the defects and hence the appearance of voidions. However, another unifying feature of the investigated systems is the underlying crystalline lattice, which is simple cubic in all cases. This raises the question whether a soft repulsive isotropic potential which stabilizes the same lattice would similarly be capable of forming voidions. To check this, we performed MC simulations of a single defect in a simple cubic crystal consisting of particles interacting via such a potential, as found in Refs. [173, 174]:

$$\beta U(r) = \begin{cases} \beta\epsilon \left( A \left( \frac{r}{\sigma} \right)^{-n} + \sum_{j=1}^2 \lambda_j \left( 1 - \tanh \left[ k_j \left( \left( \frac{r}{\sigma} \right) - \delta_j \right) \right] \right) + f_{\text{shift}}(r) \right), & r/\sigma \leq 2.25 \\ 0, & r/\sigma > 2.25 \end{cases}, \quad (5.5)$$

where

$$f_{\text{shift}}(r) = B \left( \frac{r}{\sigma} \right)^2 + C \left( \frac{r}{\sigma} \right) + D, \quad (5.6)$$

and the optimized parameters  $A = 0.394620116$ ,  $n = 5.31842$ ,  $\lambda_1 = 0.247527755$ ,  $k_1 = 58.1066$ ,  $\delta_1 = 2.63593$ ,  $\lambda_2 = 0.533048319$ ,  $k_2 = 4.35419$ ,  $\delta_2 = 1.05393$ ,  $B = -0.0187544$ ,  $C = 0.0971676$ , and  $D = -0.624056$ , and the cut-off radius  $r_{\text{cut}}/\sigma = 2.25$ . The energy scale was set to  $\beta\epsilon = 25$ .

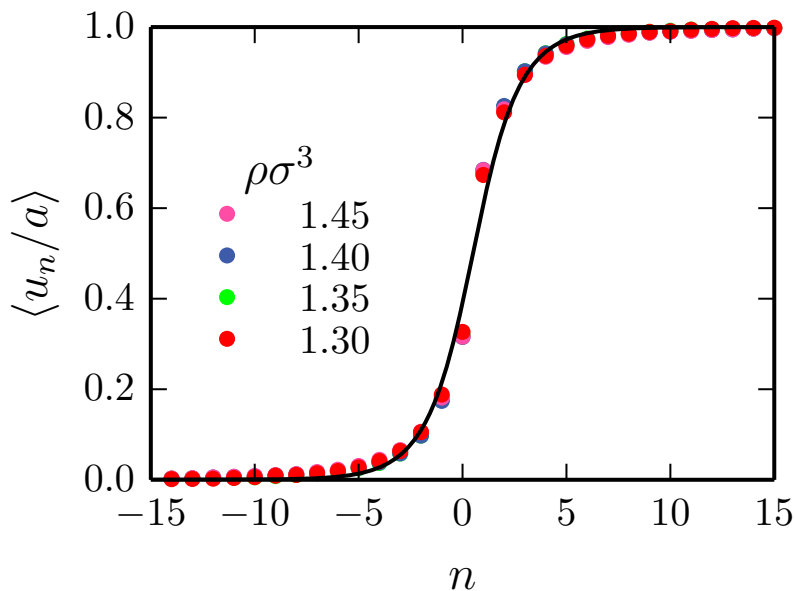


**Figure 5.6:** Averaged displacement field  $\langle u_n \rangle$  along the vacancy for a simple cubic crystal of spheres interacting through an isotropic potential, for four different densities  $\rho\sigma^3$ . The displacements inside these defects follow the sine-Gordon equation. The energy scale was set to  $\beta\epsilon = 25$ .

As shown in Figure 5.6, the deformation field associated with this defect again perfectly follows the Frenkel-Kontorova model, and spreads out over approximately 10 lattice sites, independent of the density. Hence, hard flat faces are clearly not a requirement for the formation of voidions. Moreover, as the presence and structure of vacancies is largely independent of the system density, defect concentration, and particle interaction, it is highly likely that voidions are an inherent feature of simple cubic crystals of repulsive particles.

## 5.4 Discussion and Conclusions

In conclusion, we have used event-driven molecular dynamics and Monte Carlo simulations to explore the structure and dynamics of point defects in crystals of hard cubes and slanted cubes. The vacancies observed in these crystals clearly show strong similarities to crowdions in atomic systems, both in terms of structure, and in terms of their diffusive behavior. Specifically, their deformation fields closely follow the Frenkel-Kontorova model [151, 155], and their diffusion exhibits the behavior of a persistent random walk [149, 150]. Hence, we conclusively identify these vacancies as a vacancy-analogue of crowdions.

Our investigation has led to a number of intriguing observations. First, the structure of the vacancies appears to be extremely robust to changes to the model system, in terms of packing fraction, defect concentration, and particle shape. Second, using an isotropic potential we show that hard flat faces are clearly not a requirement for the formation of voidions. We hypothesize that voidions are an inherent feature of simple cubic crystals of repulsive particles. Third, in contrast to the structure, the diffusion of the defects strongly depends on the packing fraction, but does so in an unexpected way: higher packing fractions lead to faster defect diffusion.

Finally, we showed that the vacancies in our systems exhibit almost ideal interactions. Together with the method we introduced for pinning defects, this opens the door to a fast check on whether vacancies in a given system are capable of delocalizing: one can simply perform a simulation of a crystal with a single defect, and investigate its structure. We expect that this method will be helpful in the future in identifying whether defects may play an important role in determining the phase behavior.

## 5.5 Acknowledgements

I would like to thank Frank Smallenburg for sharing his code for the event-driven molecular dynamics simulations of hard polyhedra. I would like to thank Robin van Damme for his work on the vacancy concentrations in the slanted cubes system. I would also like to thank Michiel Hermes, Matthieu Marechal, Hartmut Löwen, and Jette van den Broeke for useful discussions.

---

## Formation of large two-dimensional single colloidal crystals by doping with active particles

---

Using simulations we explore the behaviour of two-dimensional colloidal (poly)crystals doped with active particles. We show that these active dopants can provide an elegant new route to removing grain boundaries in polycrystals. Specifically, we show that active dopants both generate and are attracted to defects, such as vacancies and interstitials, which leads to clustering of dopants at grain boundaries. The active particles both broaden and enhance the mobility of the grain boundaries, causing rapid coarsening of the crystal domains. The remaining defects recrystallize upon turning off the activity of the dopants, resulting in a large-scale single-domain crystal.

## 6.1 Introduction

Colloidal crystals are ordered, self-assembled solids comprised of (sub)micron particles that are arranged on a periodic lattice. Such crystals are almost always polycrystalline in nature and feature grain boundaries that separate adjacent crystal domains of different crystallographic orientations [175]. Unfortunately, the presence of these grain boundaries is well known to drastically alter the material properties compared to a single crystal, for instance altering the photonic properties of the crystal [176]. Avoiding the formation of grain boundaries during the fabrication of colloidal crystals is very challenging and typically relies on either controlled growth of a single domain [176, 177], epitaxial growth from a template [178–181], or applying external fields [182–184]. Hence, new methods to remove grain boundaries are highly desirable. Here, we examine an elegant, new avenue for removing grain boundaries: doping colloidal polycrystals with self-propelled particles.

Self-propelled particles, also known as active particles, incessantly convert energy into self-propulsion, and as such are intrinsically out-of-equilibrium. While traditionally such particles occurred solely within the purview of natural systems (e.g. bacteria [185, 186]), recent experimental breakthroughs have led to many novel types of synthetic colloidal swimmers and self-propelled particles [64–69]. These systems exhibit a wealth of new phase behaviour, including, for example, motility-induced phase separation into dense and dilute phases [67–77], giant density fluctuations [79, 80], and swarming [81]. Moreover, experimental and simulation studies have shown that the dynamics of a passive system can be altered dramatically by the incorporation of active particles [187–189]. Even for very low concentrations ( $< 1\%$ ), where the self-propelled particles can be viewed as active “dopants”, they can strongly alter the properties (e.g. dynamics) of the underlying passive system. Specifically, active dopants have been shown to promote crystallization in hard sphere glasses [187] and it has recently been suggested that active dopants can be used to help fabricate large, defect-free crystals [188]. Here we confirm this possibility using computer simulations of dense mixtures of active and passive spherical colloids, and explore the mechanism responsible for the growth of crystal domains.

## 6.2 Model and Methods

We perform Brownian dynamics simulations of two-dimensional crystals consisting of  $N$  particles interacting with a purely repulsive Weeks-Chandler-Andersen (WCA) potential

$$\beta U_{WCA}(r) = \begin{cases} 4\beta\epsilon \left[ \left(\frac{\sigma}{r}\right)^{12} - \left(\frac{\sigma}{r}\right)^6 + \frac{1}{4} \right], & r/\sigma \leq 2^{1/6} \\ 0, & r/\sigma > 2^{1/6} \end{cases} \quad (6.1)$$

with  $\sigma$  the particle diameter,  $\beta\epsilon = 40$  the energy scale, and  $\beta = 1/k_B T$ , where  $k_B$  is the Boltzmann constant and  $T$  is the temperature. We activate a small fraction of randomly selected particles  $\alpha = N_a/N$  by adding a constant self-propulsion force  $f$  along the self-propulsion axis  $\hat{\mathbf{u}}_i$ . The direction of this axis  $\hat{\mathbf{u}}_i$  rotates with the Brownian rotational diffusion coefficient  $D_r = 3D_0/\sigma^2$  with  $D_0$  the short-time diffusion coefficient. For passive particles  $f = 0$ . As we need large systems to study the grain growth, we

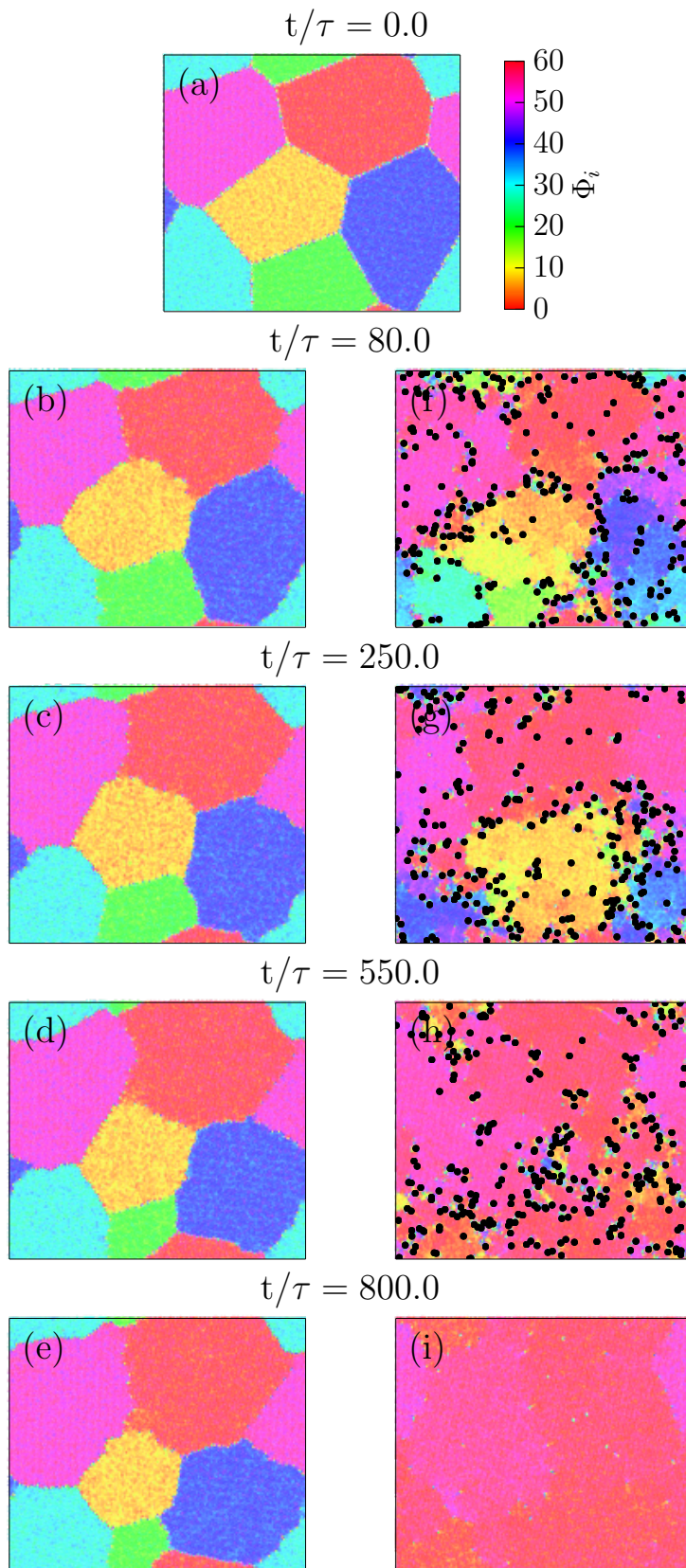


**Figure 6.1:** Grain growth in a passive system (a-e) vs a doped system (a,f-i) starting from initial configuration (a), showing significant coarsening of crystal domains in the doped system, compared to its purely passive counterpart. Here the color indicates the local orientation of a particle as given by Equation 6.2. The initial configuration shown in (a) was created by filling polygonal domains with crystallites of different orientations. In the right panels we activate a fraction  $\alpha = 0.0076$  of particles for  $0 < t/\tau < 550$  with a self-propulsion of  $f\sigma/k_B T = 90$ . Active particles are plotted in black at many times their diameter to improve their visibility. After the activity of the self-propelled particles is switched off we can clearly see that the polycrystal has coarsened. System size:  $N = 39446$  and the density is  $\rho\sigma^2 = 0.842$ .

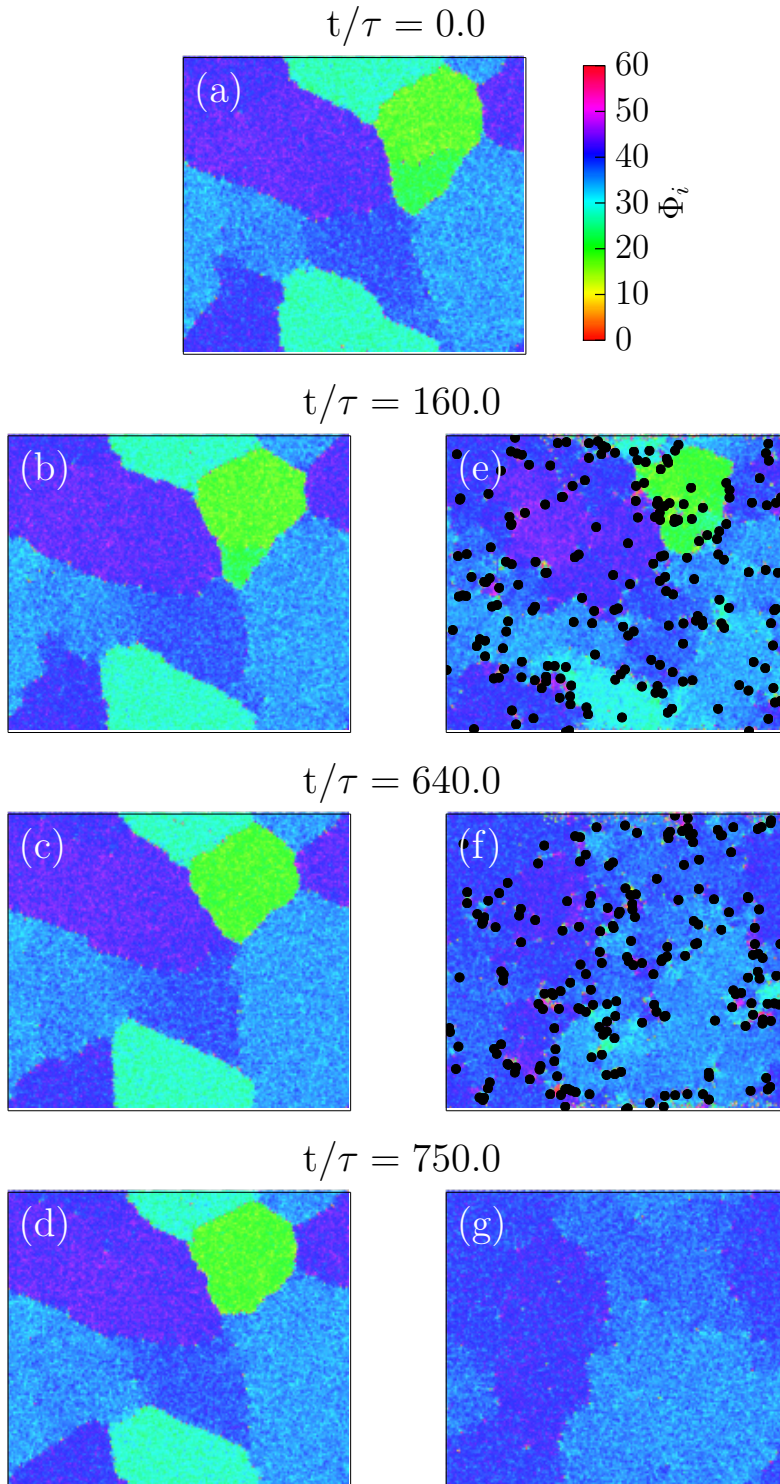


**Figure 6.2:** Grain growth in a passive system (a-d) vs a doped system (a,e-g) starting from initial configuration (a), showing significant coarsening of crystal domains in the doped system, compared to its purely passive counterpart. The initial configuration shown in (a) was obtained through crystallization of a supercooled fluid. In the right panels we activate a fraction  $\alpha = 0.00264$  of particles for  $0 < t/\tau < 640$  with a self-propulsion of  $f\sigma/k_B T = 90$ . Active particles are plotted in black at many times their diameter to improve their visibility. After the activity of the self-propelled particles is switched off for a while we can clearly see that the polycrystal has been coarsened. System size:  $N = 75625$  and the density is  $\rho\sigma^2 = 0.825$ .

neglect hydrodynamic interactions. We measure time in units of the short-time diffusion  $\tau = \sigma^2/D_0$ .

Note that we have assumed throughout this study that the active particles interact in exactly the same manner as their passive counterparts. This ensures that the active particles are compatible with the underlying crystal of the passive particles.

### 6.3 Results

We begin by examining the effect of active dopants on grain boundaries. In Figure 6.1 we show a time series of the evolution of a polycrystal in thermal equilibrium ( $\alpha = 0$ ) and in the case where some particles are active ( $\alpha = 0.0076$ ). The initial polycrystal, shown in Figure 6.1(a), was created by filling polygonal domains with crystallites of different orientations. For the doped case, a random selection of particles were then identified as active. Note that this assumes that the particles are turned active after the crystallization process has taken place. In the snapshots in Figure 6.1, we color code particles according to their local orientation using

$$\Phi_i = \frac{1}{\mathcal{N}_i} \sum_{j=1}^{\mathcal{N}_i} \theta_{ij}, \quad (6.2)$$

with  $\mathcal{N}_i$  the number of nearest neighbours of particle  $i$  as determined by a Voronoi construction, and the angle  $\theta_{ij} = \tan^{-1}(\mathbf{r}_j - \mathbf{r}_i)$  with  $\mathbf{r}_i$  the position of particle  $i$  and  $-\pi \leq \theta_{ij} \leq \pi$  [114]. In Figure 6.1(a-e) we show how the passive system evolves in time. Clearly, in thermal equilibrium ( $\alpha = 0$ ) the grain structure evolves very slowly: the thermal fluctuations allow for some motion of the grain boundaries over long periods of time, yet their mobility is very low, and as such little grain growth occurs. However, as shown in Figures 6.1(f-h), upon activation of a small number of particles,  $\alpha = 0.0076$ , we observe a large increase in the grain boundary mobility, leading to significant coarsening of the domains over time. Interestingly, whereas in thermal equilibrium the grains are separated by a thin, smooth interface, the grain boundaries in the activated systems are highly fluctuating and much broader, reminiscent of the local melting of the grain surfaces observed in Ref. [188]. Note that we also examined the evolution of polycrystals that were obtained through crystallization of a supercooled fluid (instead of the artificially formed polycrystals as shown in Figure 6.1) and observed no significant differences. The time evolution of such a system is shown in Figure 6.2.

From Figures 6.1 and 6.2 it is clear that upon activation, self-propelled particles accumulate at the grain boundaries. This accumulation of self-propelled particles enables the rearrangement of many particles at the surface of the grains leading to significant motion of the boundary over time. In the process, the grain boundaries essentially disappear, and what remains is a single-domain crystal which now contains many local defects as the active particles are constantly perturbing the crystal lattice. The active particles have thus restructured the solid and annealed out the otherwise persistent grain boundaries, at the expense of creating other local defects.

While the removal of grain boundaries is itself an important step in developing single crystals, it is also highly desirable to remove these local defects. It turns out that this comes almost for free. Specifically, if we switch the activity off, i.e. making all particles

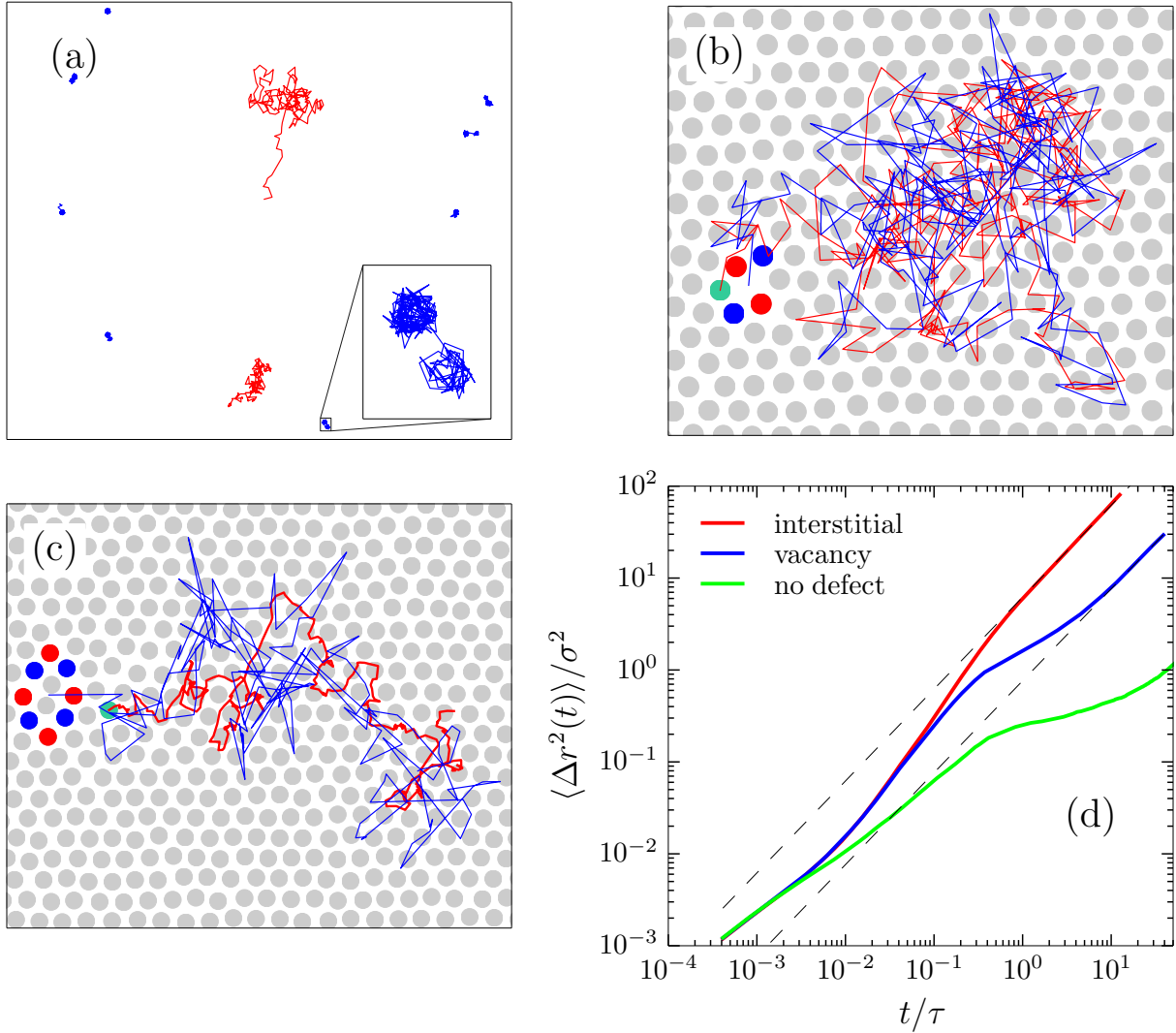


**Figure 6.3:** (a) Trajectories of active particles with  $f\sigma/k_B T = 50$  at  $\rho\sigma^2 = 0.825$  integrated over  $t/\tau = 100$ . Red and blue trajectories indicate mobile and caged particles, respectively. (b,c) The trajectories of mobile self-propelled particles that are carrying a vacancy (b) or an interstitial (c) for  $f\sigma/k_B T = 50$  at  $\rho\sigma^2 = 0.825$ . In the configurations in (b) and (c) the active particle is highlighted in green. Defected particles are shown in red and blue, for seven-fold and five-fold coordination, respectively. Particles are shown slightly smaller for visual purposes. (b) The active particle trajectory (red) and vacancy trajectory (blue) integrated over  $t/\tau=606$ . (c) The active particle trajectory (red) and interstitial trajectory (blue) integrated over  $t/\tau=45.6$ . (d) Mean square displacement  $\langle \Delta r^2(t) \rangle$  for a self-propelled particle  $f\sigma/k_B T = 50$  with a vacancy, an interstitial, and no point defect at  $\rho\sigma^2 = 0.825$ .

passive again ( $f = 0$ ) [Figure 6.1(i)], most of the local defects disappear yielding an almost defect-free single crystal. Importantly, this is not simply a simulation trick, experimentally one may switch off the active particles by using particles that are responsive to certain stimuli (e.g. light-activated colloids) or simply by letting all the fuel be consumed.

An important question that arises in looking at Figures 6.1 and 6.2 is how active particles that are located within a domain migrate to the grain boundaries to mediate the active grain growth. Hence, to better understand the dynamics of the active dopants within the grains, we now focus on the behaviour of active particles in a single crystal. In Figure 6.3(a), we plot the trajectories of active particles in such a single crystal domain. We clearly observe two distinct types of trajectories: some active particles migrate large distances over extended periods of time (red trajectories), while other active particles remain caged by their passive neighbours (blue trajectories).

To disentangle this mobile/immobile duality we follow the topological structure of the solid over time using a Voronoi construction which allows us to locate, in addition to the active particles, point defects in the crystals. From studying the topological structure of various snapshots, we observe that the immobile self-propelled particles are trapped inside defect-free hexagonal cages while the mobile self-propelled particles migrate by carrying a vacancy or interstitial. In Figure 6.3(b,c) we plot the trajectories of a single active particle interacting with a single interstitial and vacancy, respectively. Note that in the configurations displayed in Figure 6.3(b,c) the active particle is highlighted in green and particles with seven-fold and five-fold coordination are shown in red and blue, respectively. Clearly, the active particle and the defects remain in close proximity to each other. The strong overlap between the trajectories suggest that the defect and the active particle are attracted to each other.

Note that these defects form spontaneously due to the activity of the self-propelled particles, even when we start from a perfect single crystal. These defects diffuse along with the active particle as it moves through the crystal, allowing it to remain mobile for long periods of time. Hence, our data illustrate that active particles not only interact very strongly with the grain boundaries, but also with many other types of defects within the crystal such as (multi) vacancies and interstitials. These defects thus play a pivotal role in determining the mobility of the active particles.

To quantify the increase in mobility of self-propelled dopants upon picking up point defects, we consider the mean square displacement  $\langle \Delta r^2(t) \rangle = \langle |\mathbf{r}(t) - \mathbf{r}(0)|^2 \rangle$  of a self-propelled particle carrying a vacancy, an interstitial, and no point defect. Self-propelled particles with no defect are caged resulting in a clear plateau in  $\langle \Delta r^2(t) \rangle$ , while self-propelled particles with a defect exhibit substantial diffusion [Figure 6.3(d)]. These self-propelled particles with point defects exhibit an intermediate super-diffusive regime, scaling as  $\langle \Delta r^2(t) \rangle \sim t^b$  with  $1 < b \lesssim 1.5$ . Such a super-diffusive regime originates from the ballistic motion inside the cage or during cage jumping. While self-propelled particles with interstitials enter a diffusive regime soon after hopping, when  $\langle \Delta r^2(t) \rangle \approx \sigma$ , self-propelled particles with vacancies exhibit sub-diffusive motion after having travelled one lattice spacing. This feature arises from the fact that self-propelled particles with a vacancy become trapped inside the vacancy for a while. As a consequence, self-propelled particles have an enhanced probability of rotating their axis of self-propulsion and jump-

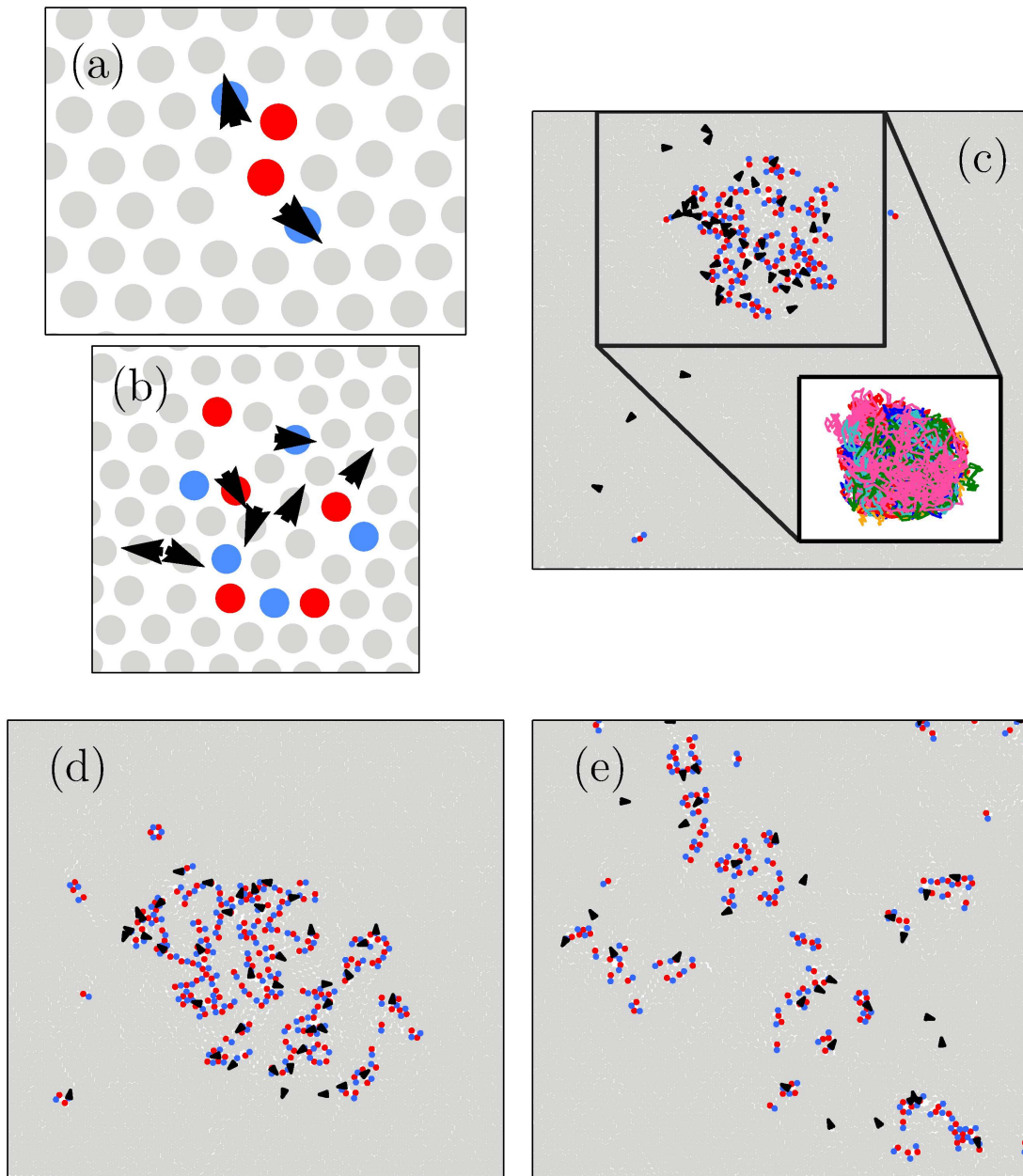


**Figure 6.4:** Snapshots of the system for increasing activity. We color-code non-sixfold coordinated particles with five or less nearest neighbours as blue and particles with seven or more neighbours as red. The black arrows are superimposed on the active particles. (a) Two active particles sharing a single vacancy. (b) Seven active particles at one end of a defect string. (c) At sufficient amounts of active particles  $\alpha = 0.004$  a single, large defect cluster forms that is rich in active particles. (d) Upon increase of the self-propulsion  $f\sigma/k_B T = 70$  the defect cluster starts to grow. (e) At very high activity  $f\sigma/k_B T = 90$  defects and active particles are found throughout the crystal. Note that the density  $\rho\sigma^2 = 0.845$  for (a-e) and the fraction of active particles  $\alpha = 0.002$  for (a,b) and  $\alpha = 0.004$  for (c-e). Particles are shown slightly smaller or bigger for visual purposes.

ing back into the vacancy, thus leading to a sub-diffusive regime. Eventually, the diffusion mediated by the vacancies also becomes Fickian, scaling as  $\langle \Delta r^2(t) \rangle \sim t$ .

The interactions between active particles and crystal defects can also generate attractive interactions between the active particles themselves. For instance, in Figure 6.4(a,b), we show a few snapshots where active particles share defects for  $f\sigma/k_B T = 50$  and  $\alpha = 0.002$ . Here, the active particles are marked with superimposed arrows that point in the direction of their self-propulsion axis. We observe that single vacancies or interstitials are often shared between two active particles, as shown in Figure 6.4(a) leading to attractions.

The attractive interactions between point defects in all combinations (vacancy-vacancy, interstitial-interstitial, and vacancy-interstitial) can lead to the formation of linear defect strings [118, 119]. We find that active particles typically accumulate at the end of these defect strings and we show one such example in Figure 6.4(b). Here many additional defects have formed a small cluster at the end of the string, owing to the fact that the active particles are constantly exciting the end of the defect string. If we increase the fraction of active particles  $\alpha = 0.004$  we observe that these defect clusters grow and eventually coalesce to form one large defect cluster that is rich in active particles, as shown in Figure 6.4(c). The attractive interactions between point defects thus drives the system to “phase separate” into a hexagonal crystal and a complex defect cluster which is rich in active particles. We plot the trajectories of some active particles that are inside the big defect cluster in the inset of Figure 6.4(c). Clearly, the active particles become trapped inside the defect cluster and are unlikely to leave the defect area. Nonetheless, they can move throughout the whole defect zone, migrating from one side of the cluster to the other. The size of the defect zone increases with increasing self-propulsion [Figure 6.4(d)]. However, upon increasing the self-propulsion  $f$  further this cluster breaks up, as shown in Figure 6.4(e).

To further explore the attraction between active particles, we determine the fraction of active neighbours of an active particle in concentric Voronoi shells. Specifically, for each active particle  $i$ , we assign each other particle in the neighbourhood of particle  $i$  to a shell  $s$ , based on the shortest path to particle  $i$  within the Voronoi construction (see Figure 6.5(a)). We then calculate the fraction of active particles within each shell, normalized by the remaining fraction of active particles in the system, i.e.  $C_{aa}(s) = g_{aa}(s)/g_{ideal}$ , where  $g_{aa}(s)$  is the average fraction of active particles in shell  $s$  around an active particle, and  $g_{ideal} = \frac{N_a - 1}{N - 1}$  which in the thermodynamic limit equals  $\alpha$ . We plot  $C_{aa}(s)$  for various self-propulsion forces  $f$  in Figure 6.5(b). For low self-propulsion  $f\sigma/k_B T \leq 30$  the active particles are distributed (almost) ideally, i.e.  $C_{aa} \approx 1$  for all  $s$ . At  $f\sigma/k_B T = 50$  we observe a large peak in  $C_{aa}$  at small  $s$ , showing that active particles are preferentially found in close proximity: active particles cluster, in agreement with Figure 6.4(c). Upon further increasing the self-propulsion we find that the peak in  $C_{aa}$  lowers and starts to decay more slowly. This corresponds to an expansion of the defect clusters which distributes the active particles over a larger area. At high self-propulsion  $f\sigma/k_B T \geq 80$  we see that the clustering becomes much less pronounced, as can also be seen from Figure 6.4(e).

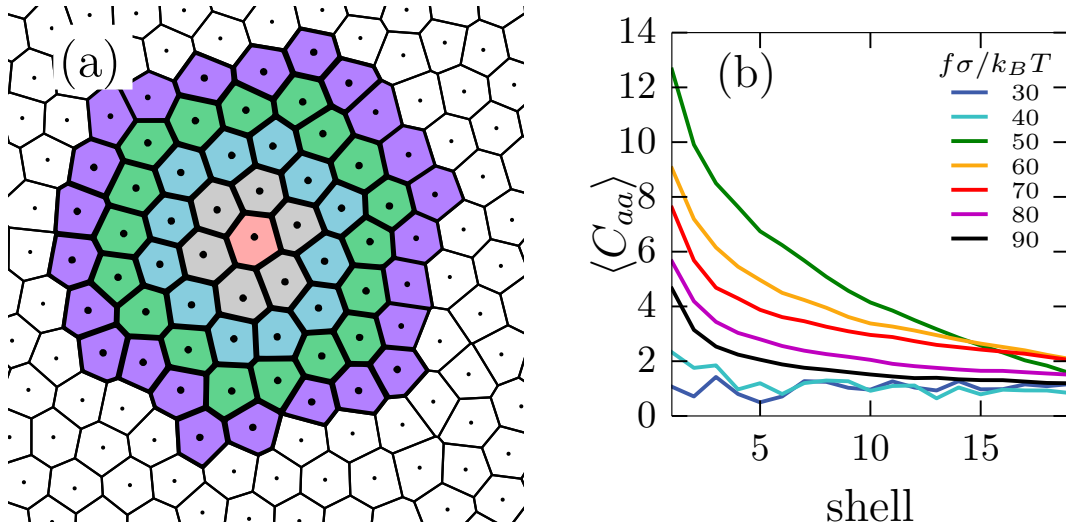


**Figure 6.5:** (a) Concentric shells of Voronoi cells around a central particle. Here particles in the same shell have the same minimal path length within the Voronoi construction. (b) Normalized fraction of active neighbours of an active particle in concentric Voronoi shells  $\langle C_{aa} \rangle$  for different amounts of self-propulsion  $f\sigma/k_B T$ .

Intuitively, one may expect that at low self-propulsion all self-propelled particles are caged. On the other hand, if the self-propulsion is high we expect active particles to be mobile. To examine the presence or absence of this dynamical transition we calculate the fraction of mobile active particles  $\langle p_m \rangle$ , defined as particles that have moved more than one lattice spacing  $\Delta r \geq a$  within a sufficiently long time interval  $\Delta t = 2.5\tau$  \*. In Figure 6.6(a) we plot  $\langle p_m \rangle$  as a function of  $f$  for varying densities. While at low self-propulsions  $f$  all active particles remain caged  $\langle p_m \rangle = 0$ , we observe a sudden increase in the average number of mobile active particles beyond some critical  $f$ , indicating a sudden onset of cage breaking [Figure 6.6(a)]. With increasing density  $\rho$  the lattice becomes more rigid, making the jump in  $\langle p_m \rangle$  shift to higher  $f$  as the active particles require more force in order to break from their cage.

We further quantify the dynamics of self-propelled particles for various self-propulsions, we calculate the mean square displacement, see Figure 6.7 for  $\alpha = 0.004$  at  $\rho\sigma^2 = 0.845$ . While, at very short time scales ( $t/\tau \lesssim 10^{-3}$ ) all mean square displacements overlap, we can see that at longer time scales the dynamics of active particles are separated into two groups. Clearly, at low self-propulsions  $f\sigma/k_B T \leq 40$  particles remain (more or less) caged, while at higher self-propulsion the mean square displacement of the active particles exhibits a strong increase over time. Such an increase of the long-term mean square displacement with increasing activity is in good agreement with the data shown in Figure 6.6(a).

We also observe that the increase in mobility of active particles strongly correlates with the formation of defects, as monitored by the average fraction of defected, non-sixfold coordinated particles  $\langle p_d \rangle$  inside the crystals, shown in Figure 6.6(b). The onset of

\*Note that we checked that our results are robust to variations in both the displacement threshold as well as the time-interval.

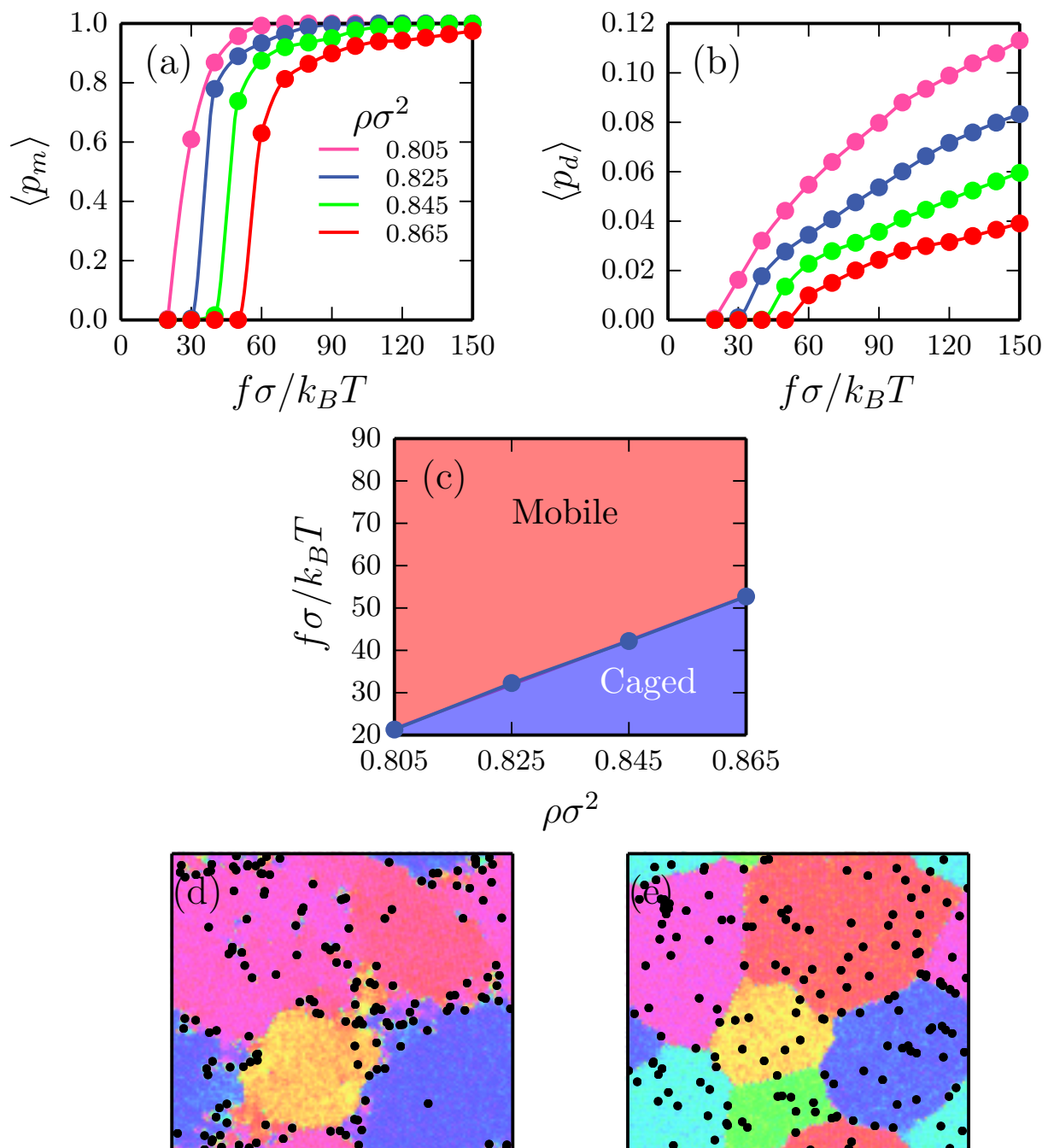


**Figure 6.6:** (a) The average fraction of mobile self-propelled particles  $\langle p_m \rangle$ . (b) The average fraction of defects  $\langle p_d \rangle$ . (c) State diagram indicating the regimes where active particles are caged vs mobile. (d) In the mobile regime,  $\rho\sigma^2 = 0.845$  and  $f\sigma/k_B T = 90$ , we observe significant coarsening of polycrystals. Here active particles accumulate at the grain boundaries. (e) In the caged regime,  $\rho\sigma^2 = 0.845$  and  $f\sigma/k_B T = 30$ , the grain growth occurs very similarly to the purely passive system. Here active particles remain inside the crystal domains and no enhanced grain growth occurs. Color-coding the same as in Figure 6.1.  $\alpha = 0.004$  in all plots.

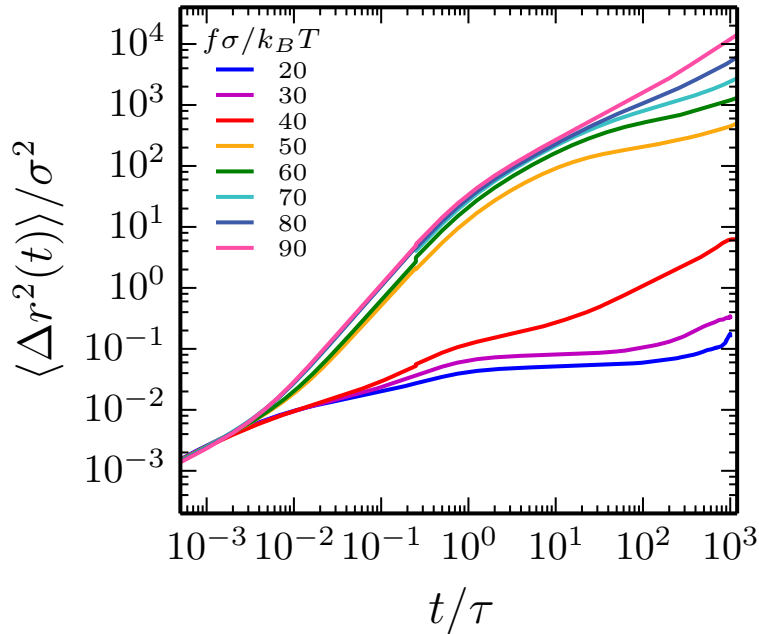


**Figure 6.7:** Mean square displacement  $\langle \Delta r^2(t) \rangle$  of self-propelled particles at  $\rho\sigma^2 = 0.845$  with an active fraction of  $\alpha = 0.004$  for different strengths of self-propulsion  $f\sigma/k_B T$ .

defect formation ( $\langle p_d \rangle > 0$ ) coincides perfectly with the large jump observed in  $\langle p_m \rangle$ . With increasing density  $\rho$ , the crystal becomes stiffer and defects form at higher self-propulsions. The interplay between the self-propulsion  $f$  and the density  $\rho$ , which respectively promote and restrict diffusion of active particles, is captured in a state diagram, as shown in Figure 6.6(c). Here we used the average fraction of mobile active particles as a cutoff  $\langle p_m^* \rangle > 0.1$  to differentiate between the two regimes where active particles are caged or mobile.

This cage-breaking transition plays a crucial role in active grain growth. Specifically we only observe significant active grain growth in systems in which the active particles are mobile. Upon activation, self-propelled particles accumulate at the grain boundaries, causing many particles at the surface of the grains to rearrange, thus leading to significant grain boundary motion over time [Figure 6.6(d)]. However, in systems where active particles are caged, the active particles cannot diffuse to the grain boundaries [Figure 6.6(e)] and we observe no such enhancement in the grain growth; the grain growth is very similar to a purely passive system. Hence, active particles enhance grain growth only when they can easily diffuse to the grain boundaries.

## 6.4 Discussion and Conclusions

In conclusion, we have explored the doping of two-dimensional colloidal (poly)crystals with sparse active particles. We find that active particles enhance the mobility of grain boundaries, leading to large-scale single-domain crystals containing local defect clusters rich in active particles. Further analysis on single crystals revealed an intricate relation

between the dynamics of active particles and the formation, and motion of defects in two-dimensional colloidal crystals. Not only do defects play a pivotal role in determining the mobility of active particles, they also generate attractions between active particles, which eventually drive the system to “phase separate” into mostly passive hexagonal crystal domains and complex defect clusters that are rich in active particles.

Our study demonstrates a novel avenue for removing grain boundaries - simply turning on and off the self-propulsion of the active particles. Hence by simply controlling the energy source for the active particles, via e.g. the availability of fuel or an external light source, active particles can be used to grow large-scale single-domain crystals.

## 6.5 Acknowledgements

I would like to thank Vasileios Prymidis, Frank Smallenburg and Sela Samin for careful reading of the corresponding manuscript.



---

## Removing grain boundaries from three-dimensional colloidal crystals using active dopants

---

Using computer simulations we explore how grain boundaries can be removed from three-dimensional colloidal crystals by doping with a small fraction of active colloids. We show that for sufficient self-propulsion, the system is driven into a crystal-fluid coexistence. In this phase separated regime, the active dopants become mobile and spontaneously gather at the grain boundaries. The resulting surface melting and recrystallization of domains result in the motion of the grain boundaries over time and lead to the formation of a large single crystal. However, when the self-propulsion is too low to cause a phase separation, we observe no significant enhancement of grain growth.

## 7.1 Introduction

One of the key challenges in colloidal self-assembly involves circumventing the long time-scales required for systems to reach their equilibrium states. For example, in colloidal systems where a crystalline phase is thermodynamically stable, the self-assembly of such a phase typically requires crossing a high free-energy barrier. Hence, both nucleation of the equilibrium crystalline phase and the annealing out of crystal defects often occur on prohibitively long time-scales [190, 191].

An exciting and promising new avenue to aid colloidal systems in crossing free-energy barriers stems from the recent development of active colloidal particles [64–69, 192]. Such particles actively use energy from their environment to generate directed motion and, as such, systems containing active particles are inherently out of equilibrium. Recent experimental and simulation studies have shown that the dynamics of passive systems can be altered dramatically by the incorporation of active particles [187–189, 193]. Interestingly, even for very low concentrations ( $< 1\%$ ), where the self-propelled particles can be viewed as active “dopants”, they can help the underlying passive system to equilibrate by facilitating the crossing of free-energy barriers. Specifically, it has been shown that active dopants can both assist in the nucleation of crystalline domains in high-density hard-sphere glasses [187], as well as in the removal of grain boundaries in two-dimensional colloidal crystals [Chapter 6].

Here we return to the question of grain boundary removal, and explore whether active dopants can also speed up the removal of grain boundaries in *three dimensions*. In comparison to the 2d case, particles in 3d colloidal crystals are typically more strongly caged, because the coordination number is higher, and as a result the free-energy barriers involved in annealing out grain boundaries and other defects are expected to be significantly higher. Hence, it is interesting to determine whether active dopants can successfully overcome these higher barriers, and thus assist in coarsening a 3d colloidal polycrystal.

It should be noted that large, defect-free colloidal crystals have important photonic uses [194], and that the growth of such crystals is typically challenging, depending on methods based on, e.g. epitaxial growth from a template [125, 178–181], the application of external fields [182–184, 195], or temperature gradients [177, 196]. Hence, the possibility of actively removing grain boundaries by the addition of active particles shows great promise in future applications.

## 7.2 Model and Methods

### 7.2.1 Model

We consider a three-dimensional system consisting of  $N$  particles that interact via the purely repulsive Weeks-Chandler-Andersen (WCA) potential

$$\beta U_{WCA}(r) = \begin{cases} 4\beta\epsilon \left[ \left(\frac{\sigma}{r}\right)^{12} - \left(\frac{\sigma}{r}\right)^6 + \frac{1}{4} \right], & r/\sigma \leq 2^{1/6} \\ 0, & r/\sigma > 2^{1/6} \end{cases} \quad (7.1)$$

with  $\sigma$  the particle diameter,  $\beta\epsilon = 40$  the energy scale, and  $\beta = 1/k_B T$ , where  $k_B$  is the Boltzmann constant and  $T$  is the temperature. From the  $N$  particles, we identify a subset of particles  $N_a$  which we “activate” by applying a constant self-propulsion force  $f$  along the self-propulsion axis  $\hat{\mathbf{u}}_i$ . We denote the fraction of active particles by  $\alpha = N_a/N$ .

We simulate the system using overdamped Brownian dynamics. Thus, the equations of motion for particle  $i$  read:

$$\dot{\mathbf{r}}_i(t) = \beta D_0 [-\nabla_i U(t) + f \hat{\mathbf{u}}_i(t)] + \sqrt{2D_0} \boldsymbol{\xi}_i(t) \quad (7.2)$$

$$\dot{\hat{\mathbf{u}}}_i(t) = \sqrt{2D_r} \hat{\mathbf{u}}_i(t) \times \boldsymbol{\eta}_i(t), \quad (7.3)$$

where the translational diffusion coefficient  $D_0$  and the rotational diffusion constant  $D_r$  are linked via the Stokes-Einstein relation  $D_r = 3D_0/\sigma^2$ . Additionally,  $\boldsymbol{\xi}_i(t)$  and  $\boldsymbol{\eta}_i(t)$  are stochastic noise terms with zero mean and unit variance. Note that for passive particles  $f = 0$ . We measure time in units of the short-time diffusion  $\tau = \sigma^2/D_0$ .

## 7.2.2 Formation of initial polycrystals

We create starting configurations that are polycrystalline by breaking up the simulation box into polyhedral Voronoi cells which we fill with randomly oriented crystal domains [197]. Specifically, we generate a set of randomly placed grain centers, and fill all space closer to a specific center than to any other center with a randomly oriented face-centered cubic crystal domain. In these configurations, it is still possible that two particles are too close to each other. To avoid these “overlaps”, we remove one of the particles if the center of masses are separated by less than the effective hard-sphere diameter, as extracted from the coexistence densities in Ref. [198]. Finally, the polycrystal is annealed for  $\sim 50\tau$  to ensure that the grain boundary structure is relaxed.

## 7.2.3 Fluid-crystal coexistence simulations

We use direct coexistence simulations to determine the fluid-crystal coexistence densities. More specifically, the coexistence between the crystal and the fluid is studied in an elongated box of  $L_x = L_y \approx L_z/4$  containing  $N = 16000$  particles. At the start of the simulation, the entire box is filled with a crystal of uniform density. A fraction  $\alpha$  of the particles are then labelled as “active” particles. To speed up equilibration, the active particles are chosen in a narrow slab in the box \*. During the simulation, the crystal partially melts near the region rich in active particles. As a result, the system forms a crystal-fluid coexistence, with the two interfaces perpendicular to  $\hat{\mathbf{z}}$ . As the fluid phase has a lower density than the overall system, the density of the crystal region increases. As a result, the crystal becomes compressed along the  $z$ -direction introducing undesirable stresses in the crystal. To allow these stresses to relax, we developed a simple algorithm to reshape the box during equilibration. Specifically, we measure the virial stress tensor

---

\*Note that we have also performed simulations where the active particles are initially distributed randomly throughout the box, but over the course of the simulations they are excluded from the crystal region and migrate to the fluid region. Hence, starting in this manner reduces the time needed to reach the steady state.

in the bulk of the crystal region. Note that in this region, the fraction of active particles is negligible, and thus the virial stress is expected to be a good approximation of the true stress. We then average the stress in the crystal region over  $0.2\tau$ , and subsequently make a small adjustment to the aspect ratio of the box which reduces the stress, while keeping the total volume constant. We then continue the simulation and repeat this process until the system is in a steady state and the stress in the crystal phase is effectively zero. We then further equilibrate for  $100\tau$  with a constant box shape, and finally start measuring the coexistence densities.

### 7.2.4 Cluster algorithm

To distinguish different crystalline domains, we use a cluster algorithm based on the local bond-order parameter  $q_6$  [199]. As a first step, we identify the neighbours for each particle, defined as all particles located within a distance  $r_c = 1.5\sigma$  of the particle in question. We denote the number of neighbours for particle  $i$  as  $\mathcal{N}(i)$ . The bond orientational order parameter of a particle  $i$  is then calculated using

$$q_{6,m}(i) = \frac{1}{\mathcal{N}(i)} \sum_{j=1}^{\mathcal{N}(i)} Y_{6,m}(\theta_{ij}, \phi_{ij}), \quad (7.4)$$

where  $Y_{6,m}(\theta, \phi)$  are spherical harmonics,  $\theta_{ij}$  and  $\phi_{ij}$  denote the polar and azimuthal angles associated with the center-of-mass distance vector  $\mathbf{r}_{ij} = \mathbf{r}_j - \mathbf{r}_i$ , and  $m \in [-6, 6]$ . We then quantify the degree of correlation in the environment of two particles  $i$  and  $j$  using

$$d_6(i, j) = \frac{\sum_{m=-6}^6 q_{6,m}(i) q_{6,m}^*(j)}{\left( \sum_{m=-6}^6 |q_{6,m}(i)|^2 \right)^{1/2} \left( \sum_{m=-6}^6 |q_{6,m}(j)|^2 \right)^{1/2}}. \quad (7.5)$$

Particles within the same domain exhibit  $d_6(i, j) \approx 1$  as a result of the translational symmetry within the local crystal lattice. On the other hand, for pairs of particles at the grain boundary  $d_6(i, j) < 1$ , as the translational symmetry is broken due to the different crystallographic orientations of the domains.

We define the number of crystalline neighbours  $\xi(i)$  of a particle  $i$  as the number of neighbours  $j$  with  $d_6(i, j) > 0.95$ . Subsequently, we consider a particle as being part of the crystal phase when  $\xi(i) \geq 9$ . Finally, we consider two particles to be part of the same domain when they are crystalline neighbours.

## 7.3 Results

In Chapter 6, we showed that it was possible to anneal out grain boundaries in two-dimensional crystals through doping with active particles. Here, we explore whether this approach is also applicable to three-dimensional systems, where the particles are more strongly caged. To this end, we explore the evolution of a polycrystal both in the case of a purely passive system ( $\alpha = 0$ ), and when a small fraction ( $\alpha = 0.01$ ) of the particles

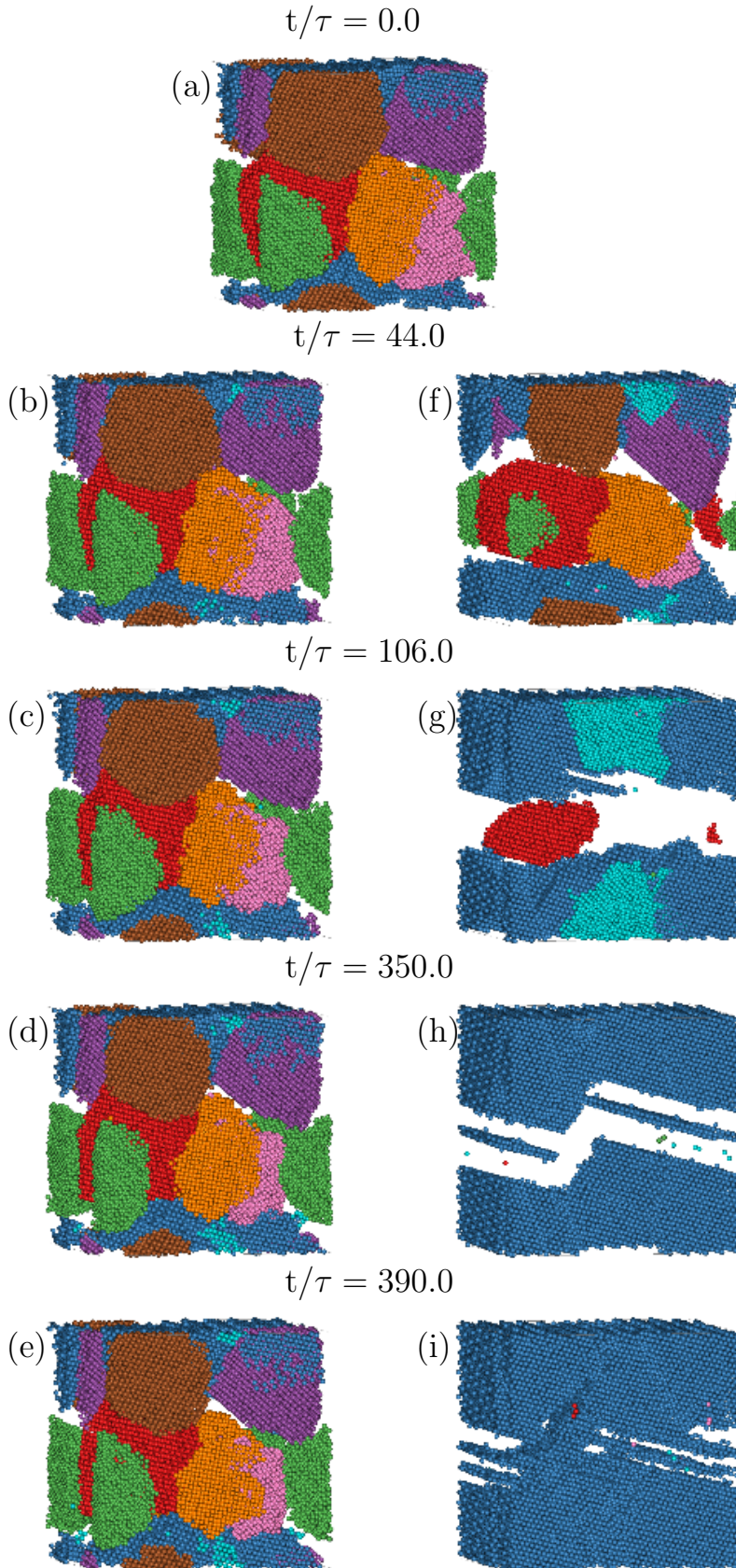


**Figure 7.1:** Grain growth in a passive system (a-e) vs a doped system (a,f-i) starting from initial configuration (a), showing significant coarsening of crystal domains in the doped system, compared to its purely passive counterpart. In the right panels we activate a fraction  $\alpha = 0.01$  of particles for  $0 < t/\tau < 350$  with a self-propulsion of  $f\sigma/k_B T = 90$ . After the activity of the self-propelled particles is switched off we can clearly see that the polycrystal has coarsened. The disordered particles are not depicted. The system contains  $N = 83481$  particles and the density is  $\rho_s \sigma^3 = 0.86$ .

is active. A series of snapshots from both scenarios is shown in Figure 7.1. Note that in these snapshots, the cluster algorithm described in Section 7.2.4 was used to identify the crystalline domains in the system, and that particles identified as disordered are not depicted. As can be seen clearly from the time-series, after  $t = 350\tau$ , the passive system still exhibits the same grain structure as in the initial configuration: the polycrystal is trapped in a metastable state and does not evolve to its single-crystal equilibrium state [Figure 7.1(a-e)]. In contrast, when a small fraction of the particles is active, we observe substantial grain boundary mobility, leading to the rapid coarsening of domains over time [Figure 7.1(f-h)]. In this case, when  $t = 350\tau$ , we are left with a single-domain crystal in coexistence with a fluid. Thus, similar to the scenario in two dimensions, active dopants help the polycrystal evolve to a large-scale single crystal. Moreover, again similar to the 2d case, upon turning off the activity [Figure 7.1(i)], the fluid region recrystallizes using the existing crystal as a template. We are left with a single domain crystal with a large stacking fault. Note that this stacking fault is the result of the finite size of our periodic simulation box, as the crystal typically chooses a random orientation incommensurate with the box shape.

We now turn our attention to the mechanism responsible for the increased mobility of the crystal grain boundaries. To explore this mechanism, we study the dynamics of the active particles during the coarsening process. In Figure 7.2 we show the time evolution of a slice of the crystal a short time after the activity is turned on. In this figure, disordered and crystalline particles are coloured grey and red, respectively, and the active particles are highlighted in black. We note that at  $t = 0$ , the active particles are randomly distributed throughout the system. However, it is clear from Figure 7.2 that by  $t = 100\tau$  almost all the active particles are located inside the grain boundaries, which have broadened into thick fluid layers. Particles located in these fluid layers exhibit high diffusion rates due to the presence of the active particles, which act like local “stirrers”. As time progresses, the domain in the center gradually melts from the outside inwards, while the adjacent domains grow. This continual surface melting and recrystallization of domains is responsible for the motion of the grain boundaries and leads to the formation of the large single crystal in Figure 7.1(h).

The appearance of a substantial fluid region, as in Figure 7.1(h), suggests that the presence of active particles shifts the phase boundaries in this system. To confirm this, we studied the coexistence between the crystal and fluid using simulations of  $N = 16000$  particles in an elongated box as discussed in Section 7.2.3. In Figure 7.3(a), we show an example snapshot, where we highlight active particles in red. Clearly, the system depicted in this snapshot has separated into a crystal containing (almost) no active particles and a fluid rich in active particles. To analyse this coexistence in detail we measure the density profile  $\rho(z)$  and active particle fraction  $\alpha(z)$  along the long axis of the box. Specifically, we divide our system into slabs of length  $dz = a$  in the long direction of the box, with  $a$  the lattice spacing of the crystal. To calculate the active particle fraction and density, we then determine the mean Voronoi volume per particle in each slab. The resulting profiles, corresponding to the system depicted in Figure 7.3(a), are shown in Figure 7.3(b). Here, two distinct densities are visible, namely a high-density crystal phase largely free of active particles and a low-density fluid phase rich in active particles. One might further ask whether the active particles accumulate at the fluid-solid interface, as they are known to

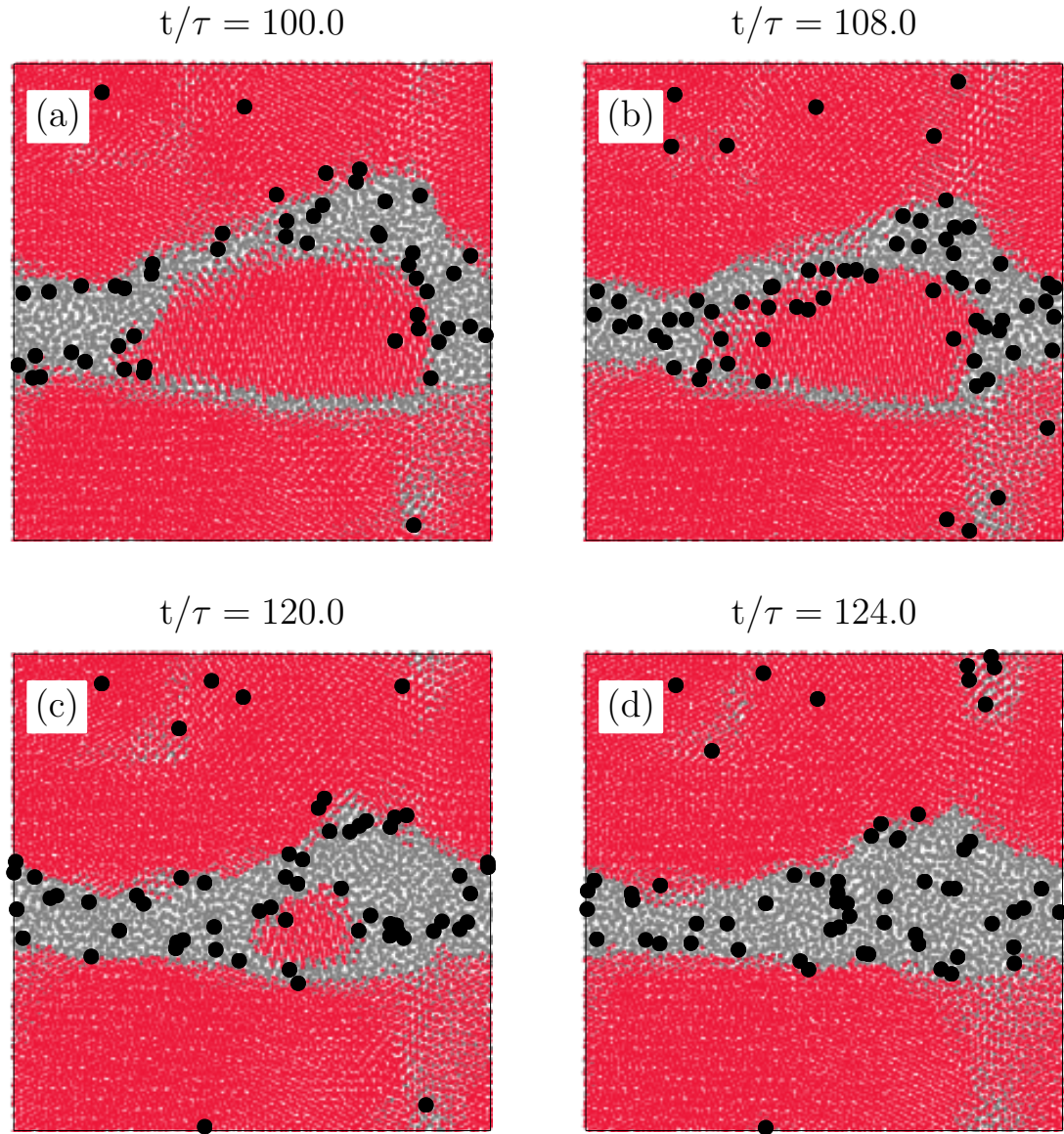


**Figure 7.2:** Activity-induced surface melting of polycrystalline domains. We color-code disordered and crystalline particles with grey and red, respectively. Active particles are highlighted in black at many times their own diameter. (a)-(d) Over time we can clearly see that the central grain melts from the surface inwards, until it is completely removed. The active particle fraction is  $\alpha = 0.01$  with a self-propulsion of  $f\sigma/k_B T = 90$ . The system size is  $N = 83481$  and the density is  $\rho_s \sigma^3 = 0.86$ .

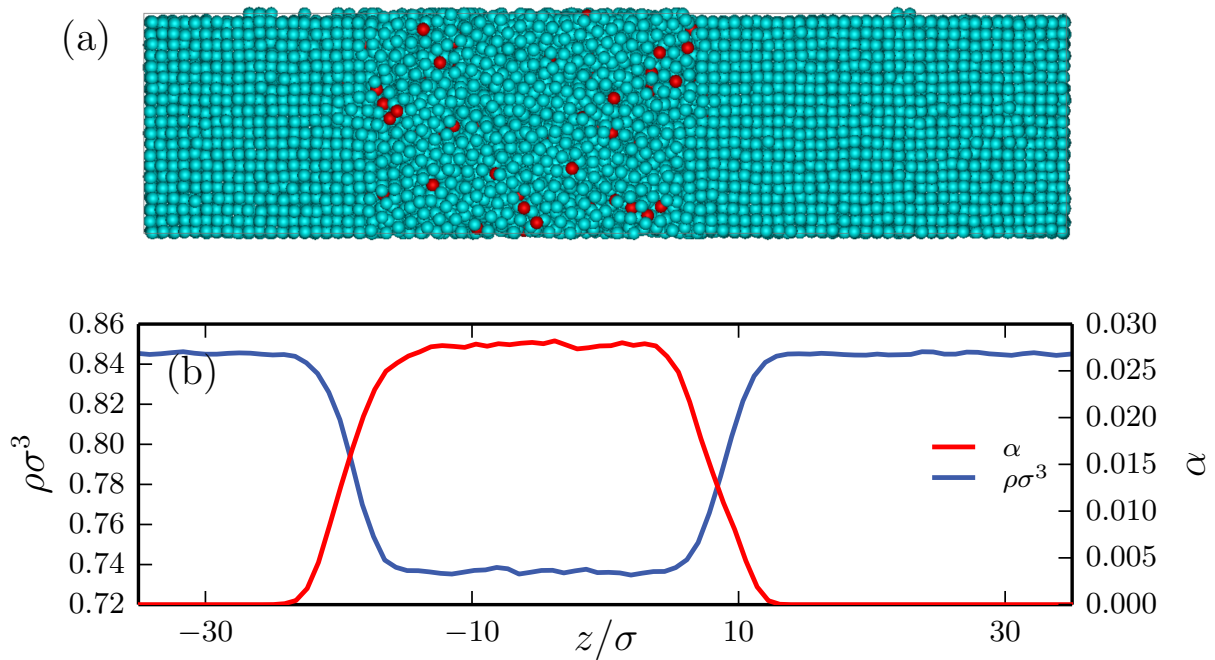


**Figure 7.3:** (a) Direct coexistence between a crystal and a fluid phase at overall density  $\rho_s\sigma^3 = 0.80$  and an active particle fraction  $\alpha = 0.01$  and self-propulsion  $f\sigma/k_B T = 50$ . (b) The corresponding density profile (blue) and the local fraction of active particles (red).

accumulate at walls [200, 201]. However, the smooth decay in active particle fraction (red line in Figure 7.3(b)) between the high and low density phases clearly indicates that the active particles do not specifically adsorb to the crystal-fluid interface.

Density profiles, like the one shown in Figure 7.3(b) can be used to map out the coexistence regions in our system. The results, for a range of overall system densities  $\rho_s$ , are summarized in Figure 7.4. From this figure, we first note that for different overall densities the coexistence curves do not collapse in the  $\rho\sigma^3$  vs  $f\sigma/k_B T$  representation when the fraction of active particles is kept fixed at  $\alpha = 0.01$ . This feature arises from the fact that our system is in fact a binary mixture and hence should not collapse in this representation. We also see from Figure 7.4 that for low activity, the system does not phase separate for any of the densities we examined. This was to be expected, since we always chose the overall system density to be higher than the predicted crystal coexistence density for the passive system ( $\rho_c\sigma^3 = 0.785$  [198]) as we were interested in removing grain boundaries from crystals. Importantly, we also see that both the crystal and fluid coexistence densities increase monotonically as a function of the activity of the dopants. Hence, when the activity is sufficiently strong, the melting density is increased beyond the overall system density, and as a result the system partially melts into a dopant-rich fluid and a nearly undoped crystal. We identify this partial melting as the driving mechanism behind the broadening of the grain boundaries observed in e.g. Figure 7.2(a). Subsequently, these fluid regions, which display high diffusion rates due to the relatively high concentration of active dopants, enable the fast annealing of the grain boundaries.

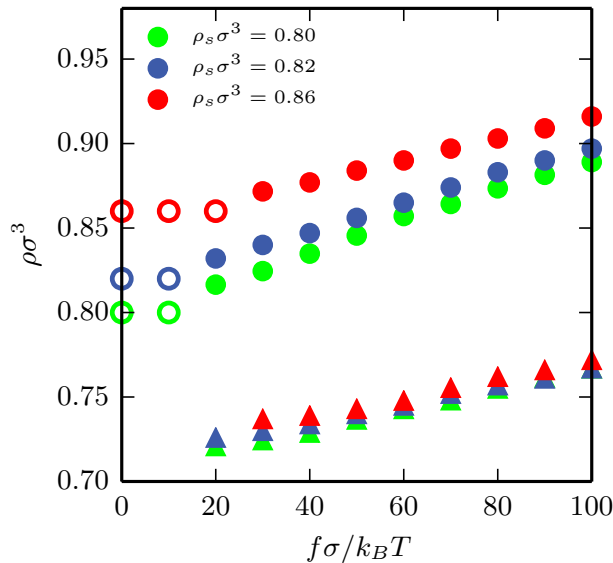


**Figure 7.4:** Coexistence densities as a function of self-propulsion  $f\sigma/k_B T$ , with a fixed active particle fraction  $\alpha = 0.01$  for three different overall system densities  $\rho_s\sigma^3$ . Open circles indicate the absence of phase coexistence (pure crystal phase). Closed circles indicate the densities of the coexisting crystal phase, and triangles indicate the coexisting fluid densities. System size:  $N = 16000$ .

Hence, we identify phase separation into a passive crystal and a fluid rich in active particles as the key mechanism behind active grain growth. To further illustrate this we will now return to the study of polycrystalline systems and follow the evolution of grain sizes over time for polycrystals of overall system density  $\rho_s\sigma^3 = 0.86$  upon the activation of a fraction of  $\alpha = 0.01$  of the particles. We now define a time scale  $t_a$  associated with the growth of a large domain by calculating the mean time required to form a crystal domain comprising at least a fraction  $X_c^* = 0.4$  of all the crystalline particles. This cutoff ensures that the domain has formed at the expense of at least three neighbouring domains. Note that we have checked that the results are robust to variation in  $X_c^*$ . We plot the time scale of annealing  $t_a$  in Figure 7.5. At low self-propulsion  $f\sigma/k_B T \lesssim 30$ , in the region where no phase separation occurs according to Figure 7.4, we observe no significant grain growth and thus  $t_a$  is far beyond our simulation-time. Only at sufficiently high self-propulsion  $f\sigma/k_B T \geq 30$ , where the system phase-separates, do we observe a huge increase in grain growth, leading to lower values of  $t_a$ . In this regime, we find that increasing the self-propulsion leads to faster annealing of polycrystalline domains. Depending on the self-propulsion  $f$ , we also observe that a large fraction of active particles remains kinetically arrested within the crystal phase.

To quantify the extent of dynamic arrest we calculate the fraction of mobile active particles  $p_m$ , defined as particles that have moved more than one lattice spacing  $\Delta r \geq a$  within a time interval  $\Delta t = 2.5\tau$ <sup>†</sup>. Clearly, at self-propulsions  $f\sigma/k_B T < 30$  where we

<sup>†</sup>We have checked that our results are robust to variations in both the displacement threshold as well as the time-interval.

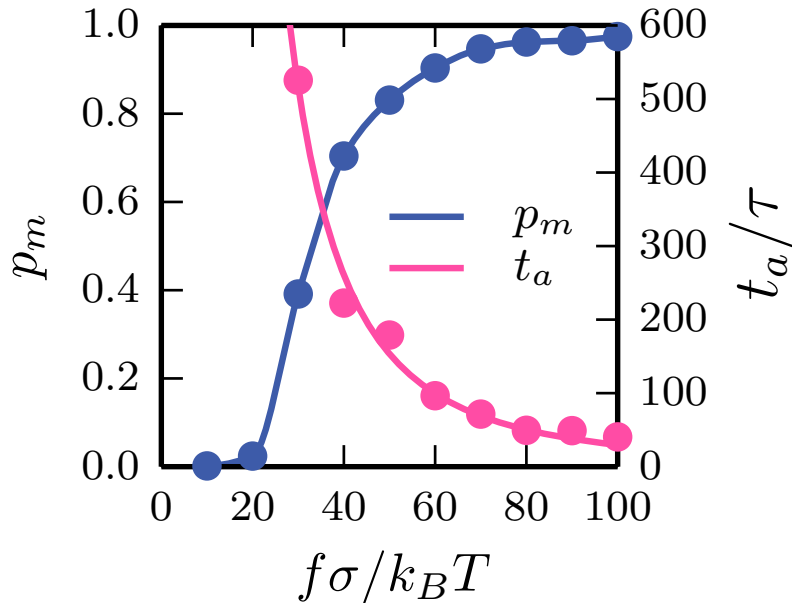


**Figure 7.5:** Time scale associated with formation of a large domain  $t_a$  and the fraction of mobile active particles  $p_m$  as a function of the self-propulsion  $f$  for a density  $\rho_s\sigma^3 = 0.86$ .

expect no phase separation, the fraction of mobile active particles  $p_m \approx 0$ : all the active particles remain caged inside the domains. At the minimal amount of self-propulsion required for phase separation,  $f\sigma/k_B T \approx 30$ , we observe a large increase in  $p_m$ , as the active particles manage to escape the crystal and create a fluid. However, near this increase only a fraction of active particles become mobile and participate in the active grain growth process. With increasing self-propulsion the fraction of active particles that partake in the process increases until it approaches unity, thus leading to lower values of  $t_a$ .

## 7.4 Discussion and Conclusions

In conclusion, we have explored how grain boundaries can be removed from three-dimensional colloidal crystals by doping with a small fraction of active colloids. We show that at sufficient self-propulsion, the system is driven into a crystal-fluid coexistence. In this case, active dopants become mobile and spontaneously gather at the grain boundaries. The resulting surface melting and recrystallization of domains is responsible for the motion of the grain boundaries and leads to the formation of a large single crystal. However, if the self-propulsion is too low to cause a phase separation, we observe no significant enhancement of grain growth.

Our study thus demonstrates that, similar to the 2d case [Chapter 6], doping with active particles provides an elegant new route to removing grain boundaries in 3d colloidal polycrystals. In both cases, we observe that the active particles are attracted to the grain boundaries. This implies that the active particles autonomously find the location inside the sample where their active properties are most helpful. Therefore, the removal of grain

boundaries via active doping is in stark contrast to more conventional methods based on external fields, which act uniformly on all the particles in the sample [182–184, 195].

Interestingly, in the 2d case we observed that the active particles do not interact solely with the grain boundaries, but also exhibit strong interactions with many other types of crystal defects [Chapter 6]. This raises the interesting question of what role these other defects, such as for example vacancies and interstitials, will play in this system.

We also show that after a single large domain has formed, the activity can be switched off at any time to recrystallize the fluid regions, using the existing crystal as a template. The required time will depend strongly on the system (and system size) in question. Note that experimentally one may switch off the activity by using active particles that are responsive to certain stimuli (e.g. light-activated colloids) or simply by letting all the fuel be consumed.

Our results, combined with the recent simulation study of active particles aiding crystal nucleation in hard-sphere glasses [187], raise the question whether active dopants can be used in other, hard to equilibrate passive systems. For instance, it will be interesting to discover whether active dopants can help nucleate long sought-after crystals, such as a colloidal diamond phase [202], or the Laves phases [53].

## 7.5 Acknowledgements

I would like to thank Vasileios Prymidis, Frank Smallenburg, Simone Dussi, and Siddharth Paliwal for many useful discussions and carefully reading the corresponding manuscript.



---

## Predicting phase behaviour of mixtures of active spherical particles

---

To date, it remains unclear whether or not it is possible to predict the phase behaviour of active particle systems. Here, we show using Brownian dynamics simulations that phase coexistences can be *predicted* quantitatively for torque-free active systems by measuring the pressure and the “reservoir densities”. More specifically, we confirm that two phases that coexist are in mechanical equilibrium by measuring the pressure in the coexisting phases. Additionally, we demonstrate that the coexisting phases are in chemical equilibrium by bringing each phase into contact with particle reservoirs, and showing that for each species these reservoirs are characterized by the same density for both phases. Using this requirement of mechanical and chemical equilibrium we accurately construct the phase boundaries from properties which can be measured purely from the individual coexisting phases. This result highlights that torque-free active systems follow simple coexistence rules, thus shedding new light on their thermodynamics.

## 8.1 Introduction

Recent experimental realizations of “active” colloidal particles, i.e. colloidal particles that self-propel, have opened the door to exploiting active building blocks in new colloidal systems (see e.g. [203–206]). These active particles incessantly convert energy into self-propulsion and, as such, systems containing active particles are inherently out-of-equilibrium.

Intriguingly, while active systems often exhibit behaviour fully prohibited in equilibrium systems, such as gas-liquid phase separation in purely repulsive systems (see e.g. [75, 207]) and symmetry-breaking motion [208, 209], the steady-state behaviour of active systems can often be summarized by phase diagrams similar to their passive counterparts, i.e. consisting of single-phase regions and coexistence regions where the lever rule holds. For instance, fairly classic phase diagrams have recently been observed in the attraction-induced liquid-gas phase coexistence of active Lennard-Jones particles [210, 211], the motility-induced phase separation observed in repulsive, self-propelled spheres [75], and even squares [212], as well as binary mixtures [213]. In equilibrium, phase boundaries and coexistences are inherently tied to bulk thermodynamic properties. Since coexisting phases have equal pressures and equal chemical potentials, the bulk properties of the individual phases provide a direct route to predicting phase coexistences - a strategy commonly used to draw phase diagrams. However, for active particles no such rules exist and a complete thermodynamic framework that describes their phase boundaries is still under construction [78, 214–221].

Early attempts to perform such a task include the work of Takatori and Brady [214] and the work of Solon *et al.* [78]. These attempts were motivated by the existence of a mechanical pressure for spherical active particles [215–220] but led to only qualitative predictions of the phase diagrams of the systems under study. In the former work, phase coexistences were predicted using an approximate generalized free energy for the system, while in the latter work it was predicted by means of a Maxwell construction, which was ultimately found to not apply to active matter systems. A different approach was adopted by Krinninger *et al.* [222], where the phase diagram of a motility-induced phase separated system was predicted by use of power functional theory, a generalization of dynamic density functional theory. This theory provided promising, yet still not quantitative agreement between the predicted and the measured phase diagram. Even more recently, Solon *et al.* [221] developed a theory of phase-separating active particles starting from a generalized Cahn-Hilliard description. Interestingly, in this description, their prediction of the binodals requires information not only on the bulk coexisting phases, but also on the interface between them.

In this Chapter, we attack the problem from a new angle, and try and address the possibility of chemical and mechanical equilibrium in these systems as directly as possible using computer simulations. Specifically, we take the existence of a mechanical pressure for torque-free spherical active particles as a starting point [78, 216] and introduce a numerical method to probe the possibility of chemical equilibrium in the system. Ideally, we would like to directly measure the chemical potential. However, currently we are unaware of an

approximation-free method for numerically accessing the chemical potential \*. Instead, we develop a simulation method which lets us to measure a quantity which is analogous to the chemical potential in equilibrium systems, namely a reservoir density. In classical statistical physics the chemical potential arises when we connect a system to a particle reservoir. The chemical potential is then directly related to the density of the reservoir. Here, we copy this idea, and develop a simulation method that measures these reservoir densities instead of the chemical potential. We then explore the possibility of chemical and mechanical equilibrium in active systems by examining two different systems: an out-of-equilibrium mixture of passive and active attractive particles, and an active-active mixture of purely repulsive particles. In agreement with Ref. [216] we find mechanical equilibrium for the coexisting phases. More importantly, we show for the first time that the reservoirs of both species are characterized by the same density for coexisting phases. Finally, we show explicitly that the phase coexistence can be *predicted* quantitatively by measuring the pressure and the reservoir densities.

## 8.2 Model and Methods

### 8.2.1 Model systems

In this Chapter we investigate phase coexistence in two different types of active systems. The first system consists of a mixture of active and passive attractive particles. Here, phase separation is induced by the attractions. Thus at mild activity, we are simply perturbing the attraction-dominated liquid-gas phase separation. In the second system, we study a purely out-of-equilibrium phenomenon, namely motility-induced phase separation in a mixture of repulsive particle with different amounts of self-propulsion.

#### Lennard-Jones active-passive mixture

For the mixture of active and passive attractive particles we consider a three-dimensional system of  $N$  spherical particles that interact via the well-known Lennard-Jones potential:

$$\beta U(r) = 4\beta\epsilon_{LJ} \left( \left( \frac{\sigma}{r} \right)^{12} - \left( \frac{\sigma}{r} \right)^6 \right) \quad (8.1)$$

truncated and shifted at  $r_c = 2.5\sigma$  with  $\sigma$  the particle diameter,  $\beta\epsilon_{LJ} = 1.2$  the energy scale, and  $\beta = 1/k_B T$ , where  $k_B$  is the Boltzmann constant and  $T$  is the temperature. Out of the  $N$  particles, we “activate” a subset of  $N_a$  particles by introducing a constant self-propulsion force  $f_a = 10k_B T/\sigma$  along the self-propulsion axis  $\hat{\mathbf{u}}_i$ . We denote the fraction of active particles by  $x = N_a/N$ . The total density of the system is given by  $\rho = N/V$ , where  $V$  is the volume of the system.

---

\*Note that the existence of a chemical potential has been assumed in several approximate theoretical treatments of active matter (see e.g. [71, 73, 223–226]).

### Weeks-Chandler-Andersen active-active mixture

For the active-active mixture of repulsive particles we consider a two-dimensional system of  $N$  particles interacting via the Weeks-Chandler-Andersen potential:

$$\beta U(r) = 4\beta\epsilon_{WCA} \left( \left( \frac{\sigma}{r} \right)^{12} - \left( \frac{\sigma}{r} \right)^6 + \frac{1}{4} \right), \quad (8.2)$$

with the interaction cutoff radius  $r_c = 2^{1/6}\sigma$  and the energy scale  $\beta\epsilon_{WCA} = 6.67$ . Specifically, we consider an active-active mixture with the self-propulsions of fast and slow species being  $f_f = 160k_B T/\sigma$  and  $f_s = 120k_B T/\sigma$ , respectively. We denote the fraction of fast particles by  $x = N_f/N$  with  $N_f$  the number of fast particles. The total density of the system is given by  $\rho = N/A$ , where  $A$  is the area of the system. Note that in this case we find a phase separation between a high density ‘‘crystal’’ phase and a low density gas phase.

### 8.2.2 Dynamics

These systems are simulated using overdamped Brownian dynamics. Specifically, the equations of motion for particle  $i$  are:

$$\dot{\mathbf{r}}_i(t) = \beta D_0 [-\nabla_i U(t) + f_i \hat{\mathbf{u}}_i(t)] + \sqrt{2D_0} \boldsymbol{\xi}_i(t) \quad (8.3)$$

$$\dot{\hat{\mathbf{u}}}_i(t) = \sqrt{2D_r} \hat{\mathbf{u}}_i(t) \times \boldsymbol{\eta}_i(t), \quad (8.4)$$

where  $\boldsymbol{\xi}_i(t)$  and  $\boldsymbol{\eta}_i(t)$  are stochastic noise terms with zero mean and unit variance, and  $f_i$  is the self-propulsion force. Note that for passive particles  $f_i = 0$ . The translational diffusion coefficient  $D_0$  and the rotational diffusion constant  $D_r$  are linked via the Stokes-Einstein relation  $D_r = 3D_0/\sigma^2$ . We measure time in units of the short-time diffusion  $\tau = \sigma^2/D_0$ .

### 8.2.3 The normal component of the local pressure tensor

Recent theoretical work has established that the mechanical pressure is a state function for systems of self-propelled particles that do not experience torque [216]. Moreover, it was recently demonstrated that when such a system undergoes phase separation, the coexisting phases have the same bulk pressure [217]. Here, we use an expression for the local pressure of an active system with only isotropic interactions [227], which we generalize to binary systems. Our expression reproduces the pressure for systems of a single species [78], and, when spatially averaged over the whole system, also amounts to the known expressions for the pressure of non-confined systems [218, 220].

Consider a binary system in  $d$  dimensions with  $N_1$  particles of species 1 and  $N_2$  particles of species 2, whose equations of motion are given by Equations 8.3 and 8.4. These equations should be now viewed with the appropriate generalization in  $d$  dimensions and with  $U(r)$  being an arbitrary pair-wise potential, with  $r = |\mathbf{r}_i - \mathbf{r}_j|$  the center-of-mass distance between particle  $i$  and  $j$ . The only difference between the two species is the value of the self-propulsion force, such that  $f_i = f^{(1)}$  for  $i \in N_1$  and  $f_j = f^{(2)}$  for  $j \in N_2$ , with

$f^{(1)} \neq f^{(2)}$ . We also define the (solid) angle between the axis of self-propulsion  $\hat{\mathbf{u}}(t)$  and a fixed coordinate system as  $\Omega(t)$ .

Let us now define the microscopic density field for the two species, which we denote as  $\Psi^{(1)}(\mathbf{r}, \Omega)$  and  $\Psi^{(2)}(\mathbf{r}, \Omega)$ , such that

$$\Psi^{(1)}(\mathbf{r}, \Omega) = \sum_{i=1}^{N_1} \delta(\mathbf{r} - \mathbf{r}_i) \delta(\Omega - \Omega_i), \quad (8.5)$$

$$\Psi^{(2)}(\mathbf{r}, \Omega) = \sum_{i=1}^{N_2} \delta(\mathbf{r} - \mathbf{r}_i) \delta(\Omega - \Omega_i). \quad (8.6)$$

For later convenience, we define the moments

$$\rho^{(\alpha)}(\mathbf{r}) = \int d\Omega \Psi^{(\alpha)}(\mathbf{r}, \Omega), \quad (8.7)$$

$$\mathbf{m}^{(\alpha)}(\mathbf{r}) = \int d\Omega \hat{\mathbf{u}}(\Omega) \Psi^{(\alpha)}(\mathbf{r}, \Omega), \quad (8.8)$$

$$\mathbf{s}_{ij}^{(\alpha)}(\mathbf{r}) = \int d\Omega \hat{\mathbf{u}}_i(\Omega) \hat{\mathbf{u}}_j(\Omega) \Psi^{(\alpha)}(\mathbf{r}, \Omega), \quad (8.9)$$

where  $i, j$  denote the spatial components of the corresponding vectors and tensors. The field  $\rho^{(\alpha)}(\mathbf{r})$  is the local density of species  $\alpha$  while the field  $\mathbf{m}^{(\alpha)}(\mathbf{r})$  is the corresponding local polarization.

We assume that the system is confined in the  $\hat{z}$  direction by a wall while it is translationally invariant in the dimensions perpendicular to  $\hat{z}$ , *i.e.* periodic boundary conditions are applied. Following Refs. [78, 216], the pressure felt by the wall can be written as

$$P_{\text{wall}} = P_{\text{id}}(z) + P_{\text{vir}, \hat{z}}(z) + \sum_{\alpha} P_{\text{swim}, \hat{z}}^{(\alpha)}(z), \quad (8.10)$$

where  $z$  denotes any point in the bulk of the system,

$$P_{\text{id}}(z) = \langle \rho(z) \rangle k_B T = \frac{1}{L^{d-1}} \int d\mathbf{r}^{d-1} \langle \rho(\mathbf{r}) \rangle k_B T, \quad (8.11)$$

is the ideal component of the pressure, where we have spatially integrated over the dimensions that are perpendicular to the  $\hat{z}$  dimension and divided by the surface  $L^{d-1}$  that we integrated over,  $\rho(\mathbf{r}) = \sum_{\alpha} \rho^{(\alpha)}(\mathbf{r})$  is the total density at point  $\mathbf{r}$ , and brackets denote an average at the steady state over noise realizations,

$$P_{\text{vir}, \hat{z}}(z) = \frac{1}{L^{d-1}} \int_{z'' < z} d\mathbf{r}'' \int_{z' > z} d\mathbf{r}' \langle \rho(\mathbf{r}'') \rho(\mathbf{r}') \rangle \partial_{\hat{z}} U(|\mathbf{r}' - \mathbf{r}''|), \quad (8.12)$$

is the standard local virial term, and

$$P_{\text{swim}, \hat{z}}^{(\alpha)}(z) = \frac{D_0 f^{(\alpha)}}{(d-1)D_r} \left[ -\beta \partial_{\hat{z}} U(z) \langle \mathbf{m}_{\hat{z}}^{(\alpha)}(z) \rangle + \beta f^{(\alpha)} \langle \mathbf{s}_{\hat{z}\hat{z}}^{(\alpha)}(z) \rangle - \partial_{\hat{z}} \langle \mathbf{m}_{\hat{z}}^{(\alpha)}(z) \rangle \right] \quad (8.13)$$

is the local swim pressure of species  $\alpha$ . In Equation 8.13  $U(z)$ ,  $\mathbf{m}_{\hat{z}}^{(\alpha)}(z)$  and  $\mathbf{s}_{\hat{z}\hat{z}}^{(\alpha)}(z)$  have been averaged similarly to Equation 8.11.

Now, since the right-hand-side of Equation 8.10 is a local quantity that does not depend on any wall properties, we straightforwardly define the normal component of the local pressure of the system as

$$P_N(z) = P_{\text{id}}(z) + P_{\text{vir},\hat{z}}(z) + \sum_{\alpha} P_{\text{swim},\hat{z}}^{(\alpha)}(z). \quad (8.14)$$

In our particle simulations, we divide the simulation box into slabs, and measure the normal component of the pressure for each slab. The contributions to each slab of the ideal and swim components of the pressure can be calculated straightforwardly, while for the virial component we follow Ref. [228].

### 8.2.4 Reservoir simulations

The standard method for showing chemical equilibrium in passive systems is to measure the chemical potential in both phases, for both species. For a passive system, this can be done in a number of different ways depending on the exact circumstance - ranging from e.g. grand canonical simulations to thermodynamic integration [87]. However, for systems containing active particles the situation is much more complex as various methods yield inconsistent results, thereby casting doubts on whether or not the chemical potential is a state function.

Here, we follow a different route and go back to more basic definitions of the chemical potential. In a textbook derivation of the chemical potential, one typically attaches the system in question to a large particle reservoir, and allows the particles of a given species to travel between the subsystem in question, and the particle reservoir. The subsystem is then in a grand-canonical ( $\mu VT$ ) ensemble, with  $\mu$  set by the chemical potential of the reservoir. Hence, if two systems have the same chemical potential, one must be able to connect them to the same particle reservoir, i.e. one with the same particle density. Here, we follow a similar procedure with our simulations.

Specifically, we connect a binary phase to particle reservoirs that only contain a single species. To this end, we divide our simulation box into two sections, one which contains the “bulk” binary phase, with the other part of the box acting as a passive (or active) particle reservoir (see Figure 8.1). We place a semi-permeable membrane at the division which only allows one of the two species, which we call species  $R$ , to pass through at no energy cost. For the other species, the wall is impenetrable with the wall-particle interaction given by the purely repulsive Weeks-Chandler-Andersen-like wall potential:

$$\beta U(z) = 4\beta\epsilon_{WCA} \left( \left( \frac{\sigma}{z} \right)^{12} - \left( \frac{\sigma}{z} \right)^6 + \frac{1}{4} \right), \quad (8.15)$$

where  $z$  is the distance of a particle in the bulk to the nearest semi-permeable wall,  $\beta\epsilon_{WCA} = 40$ , and the interaction is cut off at a distance  $z = 2^{1/6}\sigma$ .

At the start of the reservoir simulation, the bulk binary phase in the middle section of the box has the desired partial densities of the two different species, and the reservoir is initialized with a gas of species  $R$  of arbitrary density. Over the course of the simulation, particles of species  $R$  will exchange between the bulk binary phase and the reservoir. Hence, the density of this species will change in both the bulk phase, as well as in reservoir.

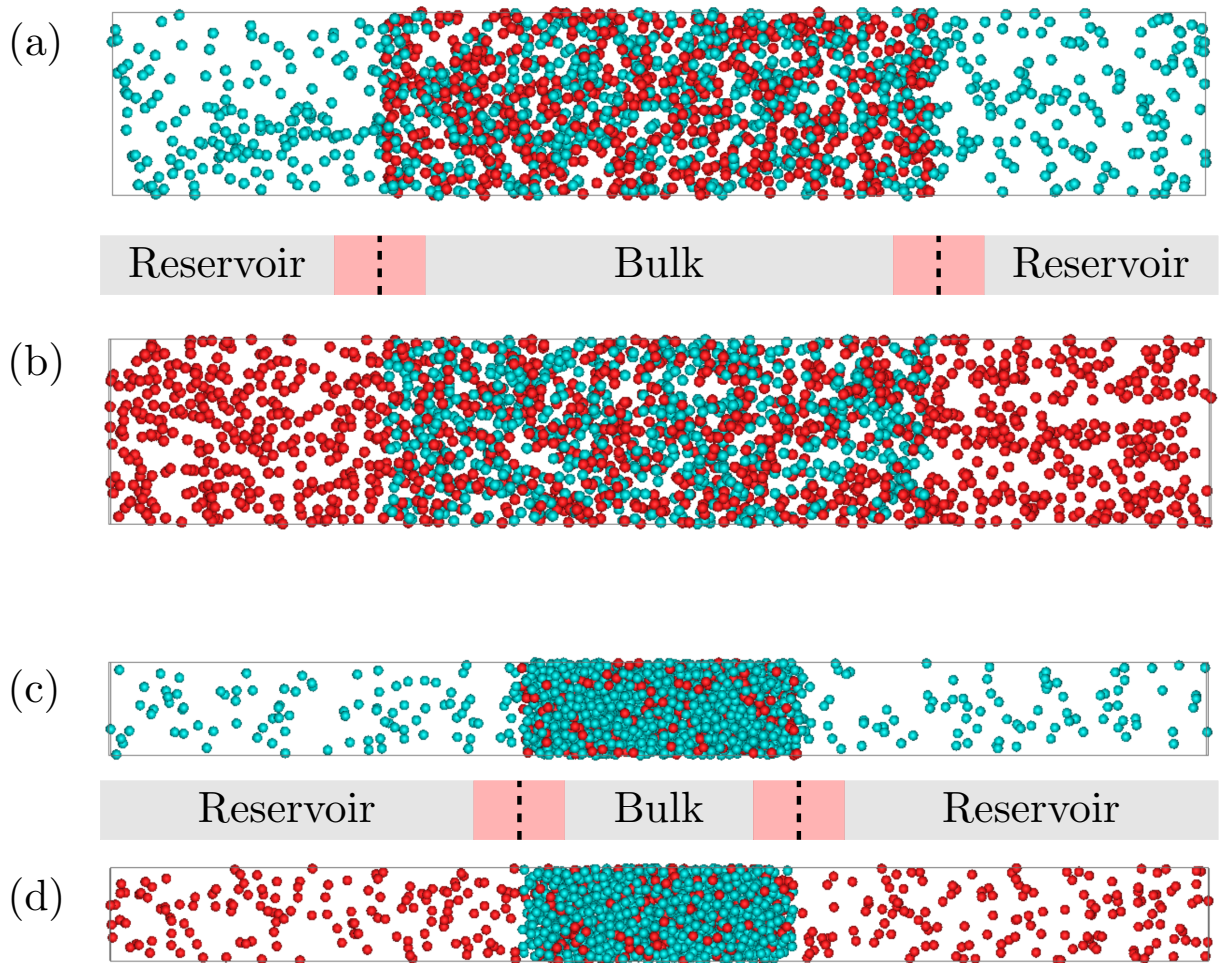


**Figure 8.1:** (a) The gas in contact with a passive particle reservoir. (b) The gas in contact with an active particle reservoir. (c) The liquid in contact with a passive particle reservoir. (d) The liquid in contact with an active particle reservoir. Note that the reservoirs associated with the gas (a,b) and liquid (c,d) phase have different cross-sections, making the reservoir densities in (a,b) seem a lot higher compared to those in (c,d) – even though they are equal.

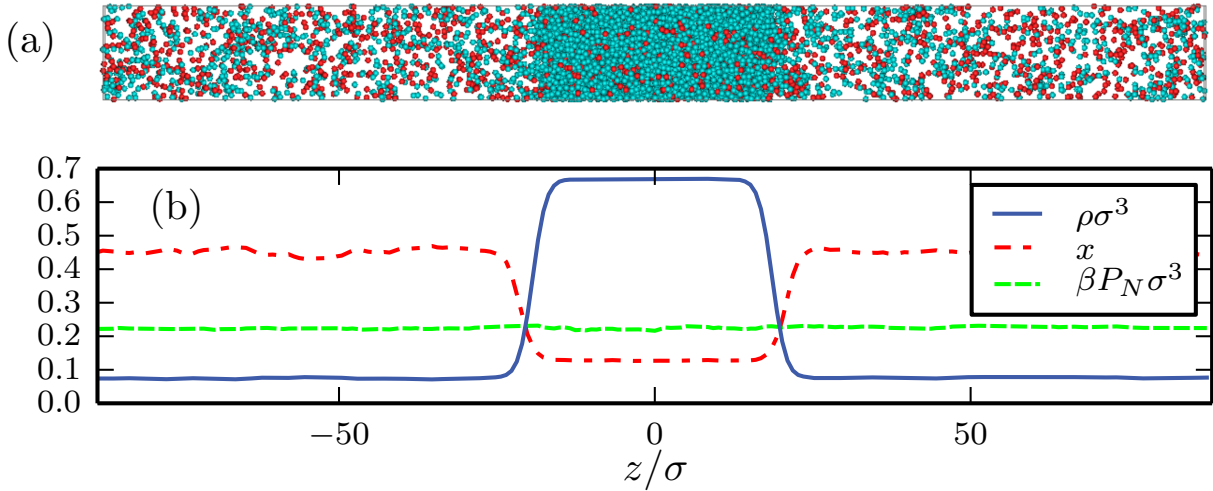


**Figure 8.2:** (a) Liquid-gas coexistence of an active-passive mixture with an overall active fraction  $x = 0.22$  at an overall density  $\rho\sigma^3 = 0.20$ . For the active particles the self-propulsion force equals  $f_a = 10k_B T/\sigma$ . (b) The corresponding density, composition, and pressure profile along the long direction  $z$  of the box. The system contains  $N = 8192$  particles.

Additionally, a small fraction of the bulk phase typically builds up on the semi-permeable membrane, and sometimes depletes the bulk region of the confined species.

To counteract such deviations from the desired partial densities in the bulk phase we “tune” the density of both species during the equilibration of the simulation. This tuning is realized by either adding or removing particles. Specifically, we measure at fixed intervals the partial densities of each species in the center of the bulk phases (i.e. away from the semi-permeable membrane). If the partial density of one of the species is too high, particles of this species are removed randomly. If the partial density of one of the species is too low, particles of this species are added randomly. Eventually, after repeating this procedure many times, the average partial densities of both species in the bulk region reach their desired constant, and a steady state reservoir density is obtained. At this point, we stop removing and adding particles, and check that the reservoir density remains constant. In this way we have checked that the binary phase and the particle reservoir are in chemical equilibrium.

## 8.3 Results

### 8.3.1 Lennard-Jones active-passive mixture

To start our investigation we construct a liquid-gas coexistence in an active-passive mixture, in the regime where the system phase separates due to attractions [210]. To this end, we set the interaction cutoff radius  $r_c = 2.5\sigma$  and the energy scale  $\beta\epsilon_{LJ} = 1.2$ , which for a purely passive system ( $x = 0$ ) results in a well-characterized liquid-gas coexistence at intermediate densities [229]. In the following we fix the self-propulsion force  $f_a = 10k_B T/\sigma$  for all active particles, and perform simulations for a range of values of the active fraction  $x$  and overall system density  $\rho$  in an elongated simulation box.

We study the phase diagram for this mixture via direct coexistence simulations. We simulated approximately 8000 particles in a three-dimensional elongated box with dimensions  $L_z = 12L_y = 12L_x$ . This choice for the dimensions of the box ensures that two flat interfaces form that span the shorter dimension [217]. For the highest density (smallest simulation box) we consider, the dimensions of the box are approximately  $12\sigma \times 12\sigma \times 144\sigma$ . Thus, the short axis of the box is much larger than the persistence length of the active particles, which is  $\beta D_0 f / 2D_r \approx 1.67\sigma$ . Note that we performed direct coexistence simulations for system compositions  $x \in (0 - 0.4)$ , and total densities  $\rho\sigma^3 = 0.20, 0.30$  and  $0.40$ . These simulations were initiated from a configuration where all particles are located within a dense slab and ran for approximately  $3500\tau$ . We collected data only for the last  $500\tau$ .

In Figure 8.2(a), we show a typical snapshot of an active-passive mixture exhibiting a liquid-gas coexistence. Here, the active and passive particles are plotted as red and blue, respectively. In Figure 8.2(b), we plot the corresponding density  $\rho(z)$ , active particle fraction  $x(z)$ , and the normal pressure  $P_N(z)$  along the long axis of the box. Note that in the bulk regime of either phase, this normal pressure  $P_N$  will be equal to the bulk pressure  $P$  of the phase in question. Figure 8.2(b) shows that, in this case, the system exhibits a gas-liquid coexistence with the gas characterized by density  $\rho^G$  and composition  $x^G$ , and the liquid characterized by density  $\rho^L$  and composition  $x^L$ . We always find the gas phase to be more rich in active particles, which is reminiscent of segregation phenomena seen in other studies of active mixtures [189, 230]. Note that in all of our simulations, the pressure is the same in both coexisting phases indicating that the system is in mechanical equilibrium.

Using composition and pressure profiles, similar to those shown in Figure 8.2(b), we map out the coexisting compositions and pressures of our active-passive mixtures, for a wide range of overall system densities  $\rho$  and compositions  $x$ . The results are plotted in Figure 8.3(a). Similar to passive systems, we find that the phase behaviour collapses in this representation, i.e. the lever rule holds within the coexistence region.

The validity of the lever rule is also evident when plotting the phase diagram in the active density - passive density ( $\rho_a - \rho_p$ ) representation, as shown Figure 8.3(b). This is consistent with the recent simulation results of Ref. [213] where they summarized the phase behaviour of a different active-passive mixture in the  $\rho_a - \rho_p$  representation. We also investigate the pressure dependence of the partial densities of each species in the coexisting liquid and gas phases. In Figure 8.3(c) we plot these partial densities  $\rho_i^\gamma$  vs. pressure  $P$  with  $i$  denoting the species (active or passive) and  $\gamma$  denoting the phase (liquid(L) or gas(G)).

Our results so far clearly demonstrate that the pressure is a key variable in controlling phase coexistences in our active-passive mixture: all phase coexistences are characterized by equal bulk pressures in the two phases. However, phase coexistence in an equilibrium binary system requires not only equal pressures between the two phases, but also equal chemical potentials for both species. This raises the question whether we can identify a quantity analogous to the chemical potential in active-passive mixtures which similarly controls the phase coexistence.

To this end, we perform reservoir simulations on these liquid and gas phases, with the other part of the box acting as a passive (or active) particle reservoir (see Figure 8.1), as

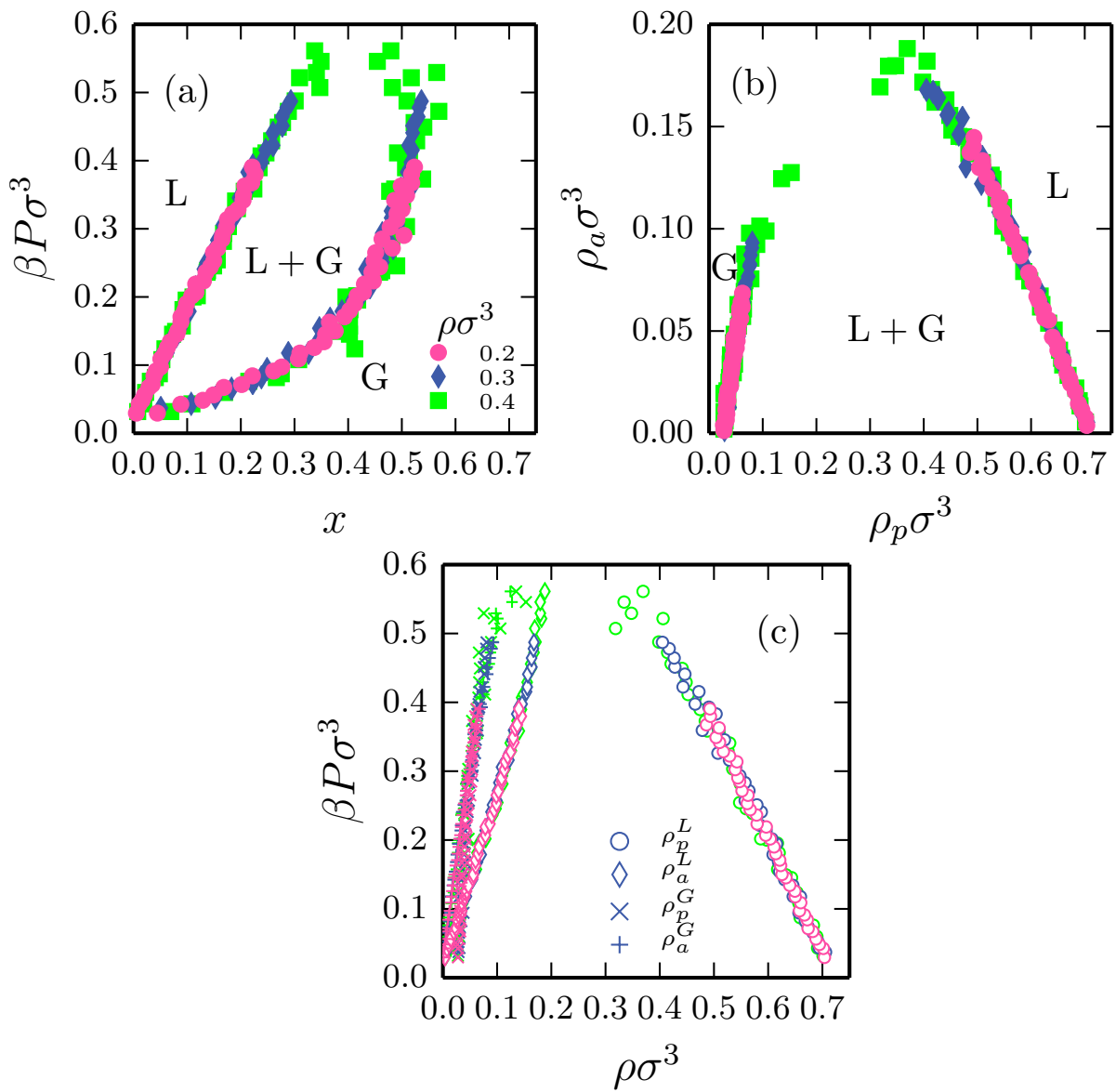


**Figure 8.3:** (a) Phase diagram of the Lennard-Jones active-passive mixture in the  $P$ - $x$  representation. (b) The same phase diagram in the  $\rho_a$ - $\rho_p$  representation. (c) Coexistence lines in the  $P$ - $\rho_a$  and  $P$ - $\rho_p$  representations.

described in Section 8.2.4. Specifically, we select a binary gas and liquid that coexist, and connect them to particle reservoirs that only contain a single species. Note that in total we will need four simulations per coexistence point, namely: the gas in contact with a passive particle reservoir, the gas in contact with an active particle reservoir, the liquid in contact with a passive particle reservoir, and the liquid in contact with an active particle reservoir. This is shown in Figure 8.1. The goal will be to determine whether the active (and passive) reservoirs associated with the coexisting phases are the same. If they are, then we can infer that there exists a chemical potential-like variable that governs the coexistence.

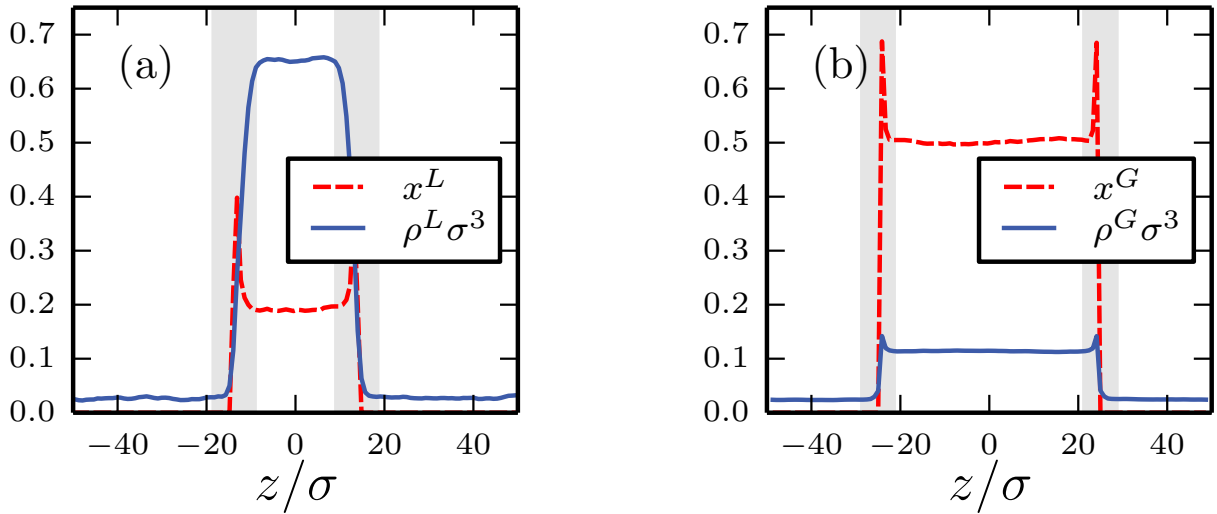


**Figure 8.4:** (a,b) Density and composition profiles of the liquid (a) and gas (b) in contact with a passive reservoir. The partial densities of the binary phases were chosen to correspond to the coexistence at pressure  $\beta P\sigma^3 = 0.34$ . Note that some active particles adsorb at the wall. We thus exclude these interfacial regions (shaded areas) in the determination of the bulk density and composition, as well as in the determination of the reservoir density.

During the equilibration of these simulations, typically a small fraction of the bulk phase builds up on the semi-permeable membrane, and sometimes depletes the bulk region of the confined species. To counteract this adsorption (see Figure 8.4) and ensure that the bulk phase has the correct density and composition far away from the semi-permeable membrane, we tune the number of particles of both species during equilibration. Eventually, the average partial densities of both species in the bulk region reach their desired constant, and also the density of the reservoir reaches a constant value.

In Figure 8.5(a), we show the time evolution of the densities in the active particle reservoirs for the coexisting liquid and gas phases at  $\beta P\sigma^3 = 0.34$ . Note that although we chose a high initial density of the reservoirs in both cases, both reservoir densities quickly converged to the same density. In Figure 8.5(b), we plot the densities of both the active and passive reservoirs as a function of the coexistence pressure  $P_{\text{coex}}$ . Clearly, for all coexisting liquid-gas pairs we find the same reservoir densities:  $\rho_p^{\text{res},L} = \rho_p^{\text{res},G}$  and  $\rho_a^{\text{res},L} = \rho_a^{\text{res},G}$ . Hence, while we still cannot directly measure the chemical potential of our active systems, this demonstrates the existence of a variable that is conjugate to the number of particles in these active systems, thereby providing clear simulation evidence of an active chemical potential.

### 8.3.2 Weeks-Chandler-Andersen active-active mixture

So far, we have shown that gas-liquid coexistence for an active-passive mixture of Lennard-Jones particles is entirely controlled by the local normal pressure and the reservoir densities. This of course raises the interesting question whether or not such phase coexistence

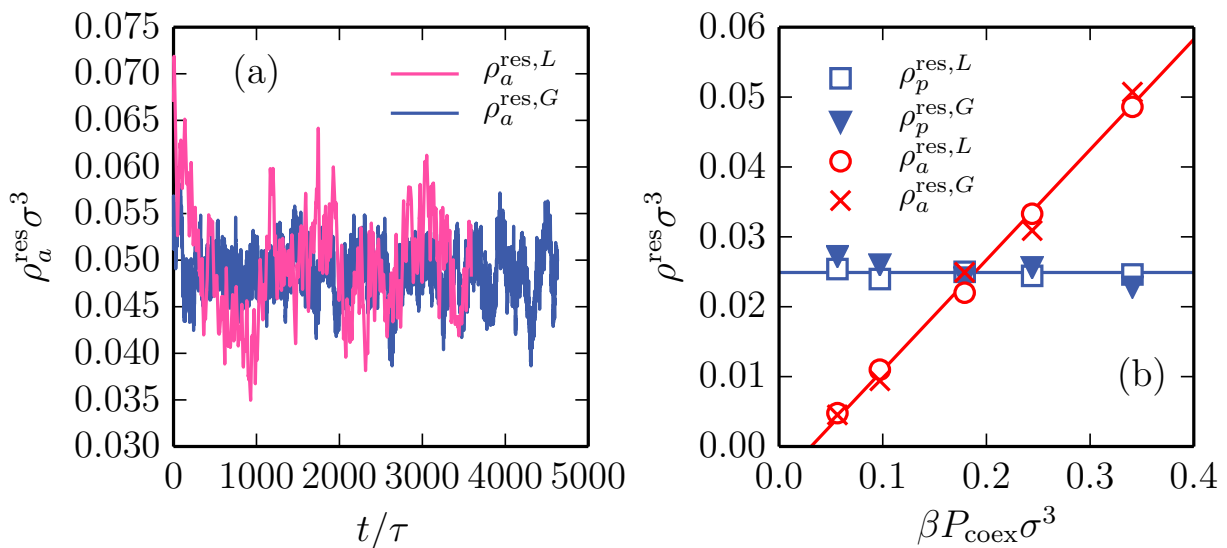


**Figure 8.5:** (a) The density in the active particle reservoir over time for both the liquid and the gas. Both phases converge to the same reservoir density of active particles. (b) The reservoir densities as a function of the coexistence pressure  $P_{\text{coex}}$ . The liquid and gas phase are in contact with the same reservoirs, showing that there is chemical equilibrium between the phases, for each species. Please note that while the passive particle reservoir density is essentially constant, the active particle reservoir density increases rapidly with increasing coexistence pressure. This hints that for this system the bulk properties of the system are essentially dictated by the active particles.

rules can also be found for systems undergoing a motility-induced phase separation, and whether or not they can be used to *predict* the phase diagram.

To this end, we use the Weeks-Chandler-Andersen potential with the interaction cut-off radius  $r_c = 2^{1/6}\sigma$  and the energy scale  $\beta\epsilon_{WCA} = 6.67$ . Here, we consider a two dimensional active-active mixture with the self-propulsions of fast and slow species being  $f_f = 160k_B T/\sigma$  and  $f_s = 120k_B T/\sigma$ , respectively. We chose such a set of forces for two reasons. First of all, such a choice ensures that even the slow species undergoes motility-induced phase separation into a gas and a crystal phase (see e.g. the state diagram in Ref. [75]). As a result, we can probe the full spectrum of compositions of the binary mixture. Secondly and more importantly, such high self-propulsions result in relatively fast dynamics for the system, so that our reservoir simulations can access a large number of configurations within reasonable computational time.

We start off by performing direct coexistence simulations between the gas and the crystal phases, where we simulated approximately 30000 particles in a two-dimensional elongated box with dimensions  $L_z = 5L_y$ . This choice for the dimensions of the box was done such that two flat interfaces are created that span the box perpendicular to its long axis [217]. Note that we also observe the formation of gas bubbles in the crystal phase, which have been reported in Ref. [217]. We performed direct coexistence simulations for system compositions  $x \in (0-1)$  with an interval of 0.1, and total densities  $\rho\sigma^2 = 0.45, 0.6$  and 0.75. For the highest density we consider, the dimensions of the box are approximately  $90\sigma \times 450\sigma$ . Thus, the short axis of the box is larger than the persistence lengths of the

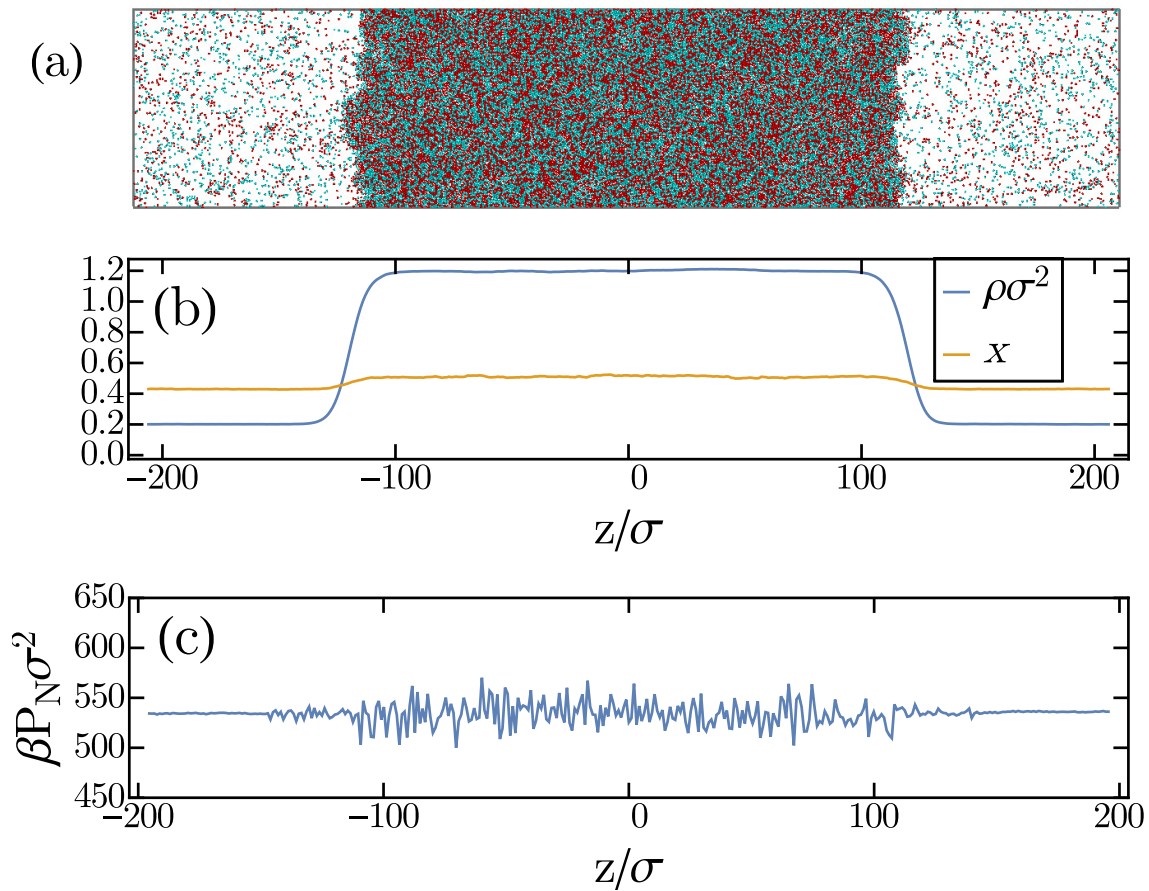


**Figure 8.6:** (a) Motility-induced phase separation of an active-active binary mixture with overall fraction  $x = 0.5$  and overall density  $\rho\sigma^2 = 0.75$ . Red particles are “fast” swimmers with self-propulsion force  $f_f = 160k_B T/\sigma$  and blue particles are “slow” swimmers with self-propulsion force  $f_s = 120k_B T/\sigma$ . The system contains approximately 30000 particles. (b) The corresponding density ( $\rho$ ) and composition profile ( $x$ ) along the long direction  $z$ . (c) The corresponding normal pressure profile along the long direction  $z$ .

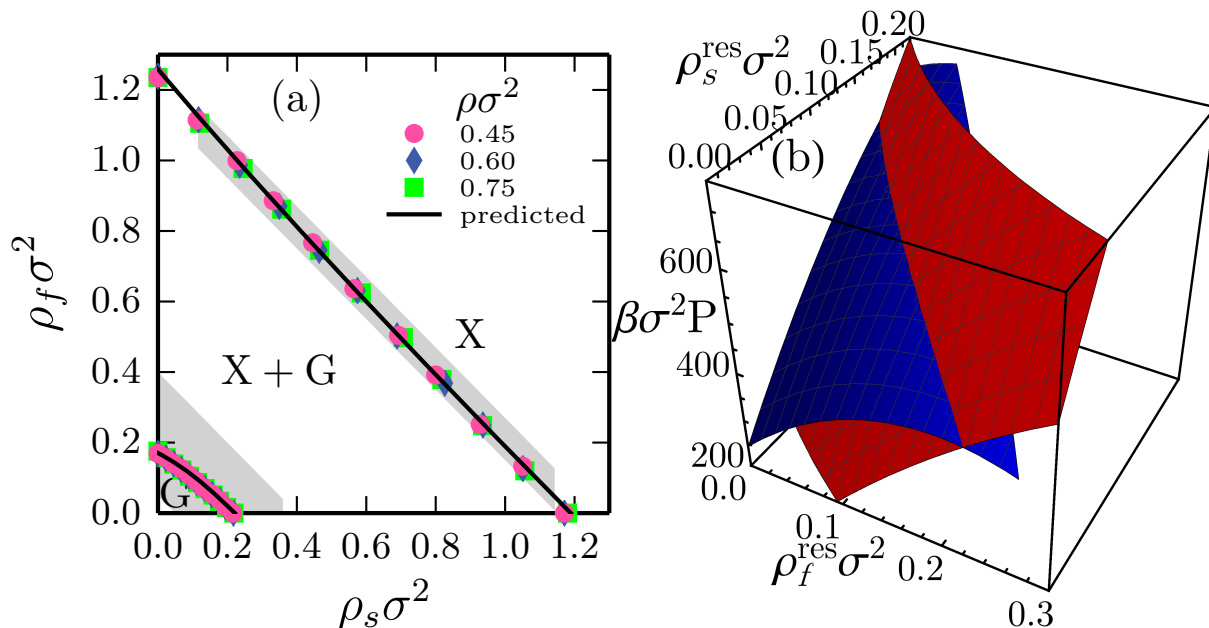


**Figure 8.7:** (a) Direct coexistence results for the phase diagram of the active-active mixture of WCA particles (markers), and the predicted phase diagram (line) in the density-density representation for fast and slow swimmers, as denoted by  $\rho_f$  and  $\rho_s$ , respectively. To predict the binodals we calculated the pressure  $P$  and reservoir densities for the fast and slow species, denoted by  $\rho_f^{\text{res}}$  and  $\rho_s^{\text{res}}$ , for a wide range of binary crystal and gas phases (shaded area). Note that X denotes the crystal phase while G denotes the gas phase. (b) Surface plots of the gas (red) and crystal (blue) reservoir densities vs the pressure. From the intersection between the two surfaces we obtain the predicted binodals in (a).

active particles, which are  $\beta D_0 f_f / D_r \approx 53.3\sigma$  and  $\beta D_0 f_s / D_r = 40\sigma$ , for the fast and slow species respectively. The simulations were initiated from a configuration where all particles are part of a hexagonal crystal and ran for approximately  $1500\tau$ . We collected data only for the last  $500\tau$ . The long running times are necessary for the relaxation of the compositions of the coexisting phases.

We then measured the local densities of the two species and the normal component of the pressure by dividing the box into slabs of length  $\sigma$  across the long  $z$ -axis and measuring the corresponding quantities for each slab. Typical results for such measurements as well as a snapshot of the system in direct coexistence are shown in Figure 8.6. The results of these direct coexistence simulations are summarized in the phase diagram, as shown in Figure 8.7(a). Clearly, also for this active-active mixture, we observe a collapse of the direct coexistence data onto a single binodal.

As a next step, we predict the phase boundaries by calculating the pressure  $P$  and reservoir densities  $\rho_f^{\text{res}}$  and  $\rho_s^{\text{res}}$  for a wide range of binary crystal and gas phases (shaded area in Figure 8.7(a)). This involves putting the binary bulk phase in contact with a reservoir of slow and fast particles separately, for both the crystal and the gas phase.

To construct the surface that corresponds to the gas in Figure 8.7(b), we ran simulations of a gas phase in contact with a reservoir in order to acquire the reservoir densities for fast and slow swimmers. The gas phases we considered had compositions in the regime

$x \in (0.1 - 0.9)$  and densities  $\rho\sigma^2 \in (0.05 - 0.5)$  (see shaded area in Figure 8.7(a)). The interval between the points we considered was 0.1 for the composition and 0.02 – 0.05 for the density. We find that for total density  $\rho\sigma^2 > 0.4$  the system spontaneously phase separates so we cannot probe this high-density regime. For each gas phase, which corresponds to a point in the  $(x, \rho\sigma^2)$  grid, we ran two simulations, one in contact with a reservoir of fast swimmers and one in contact with a reservoir of slow swimmers. Each simulation provided us with a value for the density of the corresponding reservoir and also a value for the local normal pressure in the binary gas. The values for the pressures were reassuringly in close agreement, since we simulated the same binary phase in both simulations. Thus a pair of such simulations provided us with a hypersurface  $(\rho_f^{\text{res}}, \rho_s^{\text{res}}, \beta P\sigma^2)$ , which is a function of the variables  $x$  and  $\rho\sigma^2$ . As the value of the pressure  $\beta P\sigma^2$  we take the average from the two simulations. This surface can be well fitted by a second degree polynomial. The red surface shown in Figure 8.7(b) is the fitted polynomial.

For the crystal phase we followed a similar approach. We simulate the binary crystal in contact with a reservoir of slow and fast particles separately. The points we simulated were in the interval of compositions  $x \in (0.1 - 0.9)$  and densities  $\rho\sigma^2 \in (1 - 1.30)$ , with intervals 0.1 for the composition and 0.02 for the density (see shaded area in Figure 8.7(a)). Again, the results of the simulations give us a hypersurface which we again fit with a second degree polynomial. This polynomial is the blue surface shown in Figure 8.7(b).

Note that in these reservoir simulations, we also applied a torque to the particles of the confined species that reorients these particles away from the wall. This torque was applied in order to minimize the accumulation of particles on the wall. Reassuringly, we find that the applied torque has no effects on the bulk part of the binary phase, as the orientation of the particles relaxes rapidly as we move away from the wall.

Using the requirement of mechanical and chemical equilibrium we accurately construct the phase boundaries from these properties. The intersection of the two surfaces in Figure 8.7(b) is the line where the reservoir densities of both species and pressures of the binary crystal and gas phases are equal. Thus, it should correspond to the binodals of the phase diagram. The lines on each of the two  $(\rho_f^{\text{res}}, \rho_s^{\text{res}}, P\beta\sigma^2)$  surfaces can be converted back into lines in the  $x, \rho\sigma^2$  and subsequently the  $\rho_f\sigma^2, \rho_s\sigma^2$  representation of the phase diagram. The resulting phase boundaries are drawn in Figure 8.7(a) in order to compare them with the results from the direct coexistence simulations. These “predicted” binodals are in good agreement with the direct coexistence data. We thus have predicted *quantitatively* the phase diagram for an active-active mixture undergoing motility-induced phase separation. This result highlights that also for these systems, which are extremely far from equilibrium, simple coexistence rules are satisfied. Therefore, this result sheds new light on the thermodynamics of systems of active spherical particles.

## 8.4 Discussion and Conclusions

In conclusion, we have demonstrated, for the first time, that the phase coexistence of active spherical particles is fully governed by mechanical and chemical equilibrium. We have highlighted the generality of our results by applying our technique to two very different

active systems. Our results clearly show that phase coexistence for mixtures of active particles is entirely controlled by the local normal pressure and the reservoir densities per species. Using this requirement of three sets of equal thermodynamic quantities we have quantitatively *predicted* phase coexistences for torque-free active systems.

We would like to emphasize that we have introduced a purely numerical method which allows one to construct phase diagrams from chemical and mechanical equilibrium without making approximations and without requiring a priori knowledge of the interface between the coexisting phases. We hope that this work will inspire new theoretical investigations in this direction.

## 8.5 Acknowledgements

This work was carried out in collaboration with Vasileios Prymidis. Vasileios performed the simulations on the active-active mixture of repulsive particles and derived the expression for the local pressure. I would like to thank Jeroen Rodenburg and René van Roij for useful discussions. I would also like to thank Frank Smalenburg for many useful discussions and carefully reading the manuscript.

# References

- [1] R. Brown, *A brief account of microscopical observations made in the months of June, July and August 1827, on the particles contained in the pollen of plants; and on the general existence of active molecules in organic and inorganic bodies.* Philos. Mag., 4(21):161–173, 1828.
- [2] A. Einstein, *Über die von der molekularkinetischen Theorie der Wärme geforderte Bewegung von in ruhenden Flüssigkeiten suspendierten Teilchen.* Ann. Phys., 322(8):549–560, 1905.
- [3] W. Sutherland, *A dynamical theory of diffusion for non-electrolytes and the molecular mass of albumin.* Philos. Mag., 9(54):781–785, 1905.
- [4] J. Perrin, *Mouvement brownien et réalité moléculaire.* Ann. Chim. Phys., 18:5–114, 1909.
- [5] J. Perrin. *Les atomes.* Alcan, Paris, 1913.
- [6] D. Frenkel, *Playing tricks with designer “atoms”.* Science, 296(5565):65–66, 2002.
- [7] W. Poon, *Colloids as big atoms.* Science, 304(5672):830–831, 2004.
- [8] W. Bollmann. *Crystal defects and crystalline interfaces.* Springer, Berlin, 2012.
- [9] R. J. D. Tilley. *Defects in solids.* Wiley, New York, 2008.
- [10] G. I. Taylor, *The mechanism of plastic deformation of crystals. Part I. Theoretical.* Proc. R. Soc. Lond. A, 145(855):362–387, 1934.
- [11] E. Orowan, *Zur Kristallplastizität. I.* Z. Phys., 89(9-10):605–613, 1934.
- [12] M. Polanyi, *Über eine Art Gitterstörung, die einen Kristall plastisch machen könnte.* Z. Phys., 89(9-10):660–664, 1934.
- [13] M. Polanyi, *Über die Natur des Zerreivorganges.* Z. Phys., 7(1):323–327, 1921.
- [14] J. Frenkel, *Zur Theorie der Elastizitätsgrenze und der Festigkeit kristallinischer Körper.* Z. Phys., 37(7-8):572–609, 1926.
- [15] F. R. S. Sir Lawrence Bragg and J. F. Nye, *A dynamical model of a crystal structure.* Proc. R. Soc. Lond. A, 190(1023):474–481, 1947.
- [16] P. B. Hirsch, R. W. Horne, and M. J. Whelan, *Direct observations of the arrangement and motion of dislocations in aluminium.* Philos. Mag., 1(7):677–684, 1956.
- [17] W. Bollmann, *Interference effects in the electron microscopy of thin crystal foils.* Phys. Rev., 103(5):1588, 1956.
- [18] J. W. Menter, *The direct study by electron microscopy of crystal lattices and their imperfections.* Proc. R. Soc. Lond. A, 236(1204):119–135, 1956.
- [19] E. Hall, *The deformation and ageing of mild steel: III discussion of results.* Proc. Phys. Soc. B, 64(9):747, 1951.
- [20] N. J. Petch, *The cleavage strength of polycrystals.* J. Iron Steel Inst., 174:25–28, 1953.
- [21] A. H. Chokshi, A. Rosen, J. Karch, and H. Gleiter, *On the validity of the Hall-Petch relationship in nanocrystalline materials.* Scripta Metallurgica, 23(10):1679–1683, 1989.

- [22] J. Schiøtz, F. D. Di Tolla, and K. W. Jacobsen, *Softening of nanocrystalline metals at very small grain sizes*. *Nature*, 391(6667):561, 1998.
- [23] P. N. Pusey and W. van Meegen, *Phase behaviour of concentrated suspensions of nearly hard colloidal spheres*. *Nature*, 320(6060):340, 1986.
- [24] B. J. Alder and T. E. Wainwright, *Phase transition for a hard sphere system*. *J. Chem. Phys.*, 27(5):1208–1209, 1957.
- [25] W. W. Wood and J. D. Jacobson, *Preliminary results from a recalculation of the monte carlo equation of state of hard spheres*. *J. Chem. Phys.*, 27(5):1207–1208, 1957.
- [26] G. E. Uhlenbeck. *The many-body problem*. page 498, New York, 1963. Interscience.
- [27] D. Frenkel and A. J. C. Ladd, *New monte carlo method to compute the free energy of arbitrary solids. Application to the fcc and hcp phases of hard spheres*. *J. Chem. Phys.*, 81(7):3188–3193, 1984.
- [28] T. Biben and J.-P. Hansen, *Phase separation of asymmetric binary hard-sphere fluids*. *Phys. Rev. Lett.*, 66(17):2215, 1991.
- [29] M. Dijkstra, R. van Roij, and R. Evans, *Phase behavior and structure of binary hard-sphere mixtures*. *Phys. Rev. Lett.*, 81(11):2268, 1998.
- [30] M. Dijkstra, R. van Roij, and R. Evans, *Phase diagram of highly asymmetric binary hard-sphere mixtures*. *Phys. Rev. E*, 59(5):5744, 1999.
- [31] M. Dijkstra, R. van Roij, and R. Evans, *Direct simulation of the phase behavior of binary hard-sphere mixtures: test of the depletion potential description*. *Phys. Rev. Lett.*, 82(1):117, 1999.
- [32] A. D. Dinsmore, A. G. Yodh, and D. J. Pine, *Phase diagrams of nearly-hard-sphere binary colloids*. *Phys. Rev. E*, 52(4):4045, 1995.
- [33] A. Imhof and J. K. G. Dhont, *Experimental phase diagram of a binary colloidal hard-sphere mixture with a large size ratio*. *Phys. Rev. Lett.*, 75(8):1662, 1995.
- [34] J. L. Barrat, M. Baus, and J. P. Hansen, *Density-functional theory of freezing of hard-sphere mixtures into substitutional solid solutions*. *Phys. Rev. Lett.*, 56(10):1063, 1986.
- [35] J. L. Barrat, M. Baus, and J. P. Hansen, *Freezing of binary hard-sphere mixtures into disordered crystals: a density functional approach*. *J. Phys. C*, 20(10):1413, 1987.
- [36] W. G. T. Kranendonk and D. Frenkel, *Computer simulation of solid-liquid coexistence in binary hard-sphere mixtures*. *J. Phys.: Condens. Matter*, 1(41):7735, 1989.
- [37] D. A. Kofke, *Solid-fluid coexistence in binary hard sphere mixtures by semigrand monte carlo simulation*. *Molecular Simulation*, 7(5-6):285–302, 1991.
- [38] W. G. T. Kranendonk and D. Frenkel, *Free energy calculations for solid solutions by computer simulations*. *Mol. Phys.*, 72(3):699–713, 1991.
- [39] W. G. T. Kranendonk and D. Frenkel, *Computer simulation of solid-liquid coexistence in binary hard sphere mixtures*. *Mol. Phys.*, 72(3):679–697, 1991.
- [40] X. Cottin and P. A. Monson, *A cell theory for solid solutions: Application to hard sphere mixtures*. *J. Chem. Phys.*, 99(11):8914–8921, 1993.
- [41] L. Filion, M. Hermes, R. Ni, E. C. M. Vermolen, A. Kuijk, C. G. Christova, J. C. P. Stiefelhagen, T. Vissers, A. van Blaaderen, and M. Dijkstra, *Self-assembly of a colloidal interstitial solid with tunable sublattice doping*. *Phys. Rev. Lett.*, 107(16):168302, 2011.

- [42] I. Rios de Anda, F. Turci, R. P. Sear, and C. P. Royall, *Long-lived non-equilibrium interstitial solid solutions in binary mixtures*. J. Chem. Phys., 147(12):124504, 2017.
- [43] P. Bartlett, R. H. Ottewill, and P. N. Pusey, *Freezing of binary mixtures of colloidal hard spheres*. J. Chem. Phys., 93(2):1299–1312, 1990.
- [44] P. Bartlett, R. H. Ottewill, and P. N. Pusey, *Superlattice formation in binary mixtures of hard-sphere colloids*. Phys. Rev. Lett., 68(25):3801, 1992.
- [45] M. D. Eldridge, P. A. Madden, and D. Frenkel, *A computer simulation investigation into the stability of the  $AB_2$  superlattice in a binary hard sphere system*. Mol. Phys., 80(4):987–995, 1993.
- [46] M. D. Eldridge, P. A. Madden, and D. Frenkel, *Entropy-driven formation of a superlattice in a hard-sphere binary mixture*. Nature, 365(6441):35, 1993.
- [47] M. D. Eldridge, P. A. Madden, and D. Frenkel, *The stability of the  $AB_{13}$  crystal in a binary hard sphere system*. Mol. Phys., 79(1):105–120, 1993.
- [48] M. D. Eldridge, P. A. Madden, P. N. Pusey, and P. Bartlett, *Binary hard-sphere mixtures: a comparison between computer simulation and experiment*. Mol. Phys., 84(2):395–420, 1995.
- [49] X. Cottin and P. A. Monson, *Substitutionally ordered solid solutions of hard spheres*. J. Chem. Phys., 102(8):3354–3360, 1995.
- [50] E. Trizac, M. D. Eldridge, and P. A. Madden, *Stability of the  $AB$  crystal for asymmetric binary hard sphere mixtures*. Mol. Phys., 90(4):675–678, 1997.
- [51] N. Hunt, R. Jardine, and P. Bartlett, *Superlattice formation in mixtures of hard-sphere colloids*. Phys. Rev. E, 62(1):900, 2000.
- [52] A. B. Schofield, P. N. Pusey, and P. Radcliffe, *Stability of the binary colloidal crystals  $AB_2$  and  $AB_{13}$* . Phys. Rev. E, 72(3):031407, 2005.
- [53] A.-P. Hynninen, J. H. J. Thijssen, E. C. M. Vermolen, M. Dijkstra, and A. van Blaaderen, *Self-assembly route for photonic crystals with a bandgap in the visible region*. Nat. Mater., 6(3):202, 2007.
- [54] P. M. Johnson, C. M. van Kats, and A. van Blaaderen, *Synthesis of colloidal silica dumbbells*. Langmuir, 21(24):11510–11517, 2005.
- [55] H. Maeda and Y. Maeda, *Liquid crystal formation in suspensions of hard rodlike colloidal particles: direct observation of particle arrangement and self-ordering behavior*. Phys. Rev. Lett., 90(1):018303, 2003.
- [56] A. Kuijk, A. van Blaaderen, and A. Imhof, *Synthesis of monodisperse, rodlike silica colloids with tunable aspect ratio*. J. Am. Chem. Soc., 133(8):2346–2349, 2011.
- [57] K. Zhao and T. G. Mason, *Frustrated rotator crystals and glasses of Brownian pentagons*. Phys. Rev. Lett., 103(20):208302, 2009.
- [58] K. Zhao, R. Bruinsma, and T. G. Mason, *Entropic crystal–crystal transitions of Brownian squares*. Proc. Natl. Acad. Sci. U.S.A., 108(7):2684–2687, 2011.
- [59] K. Zhao, R. Bruinsma, and T. G. Mason, *Local chiral symmetry breaking in triatic liquid crystals*. Nat. Commun., 3:801, 2012.
- [60] J.-M. Meijer, A. Pal, S. Ouhajji, H. N. Lekkerkerker, A. P. Philipse, and A. V. Petukhov, *Observation of solid–solid transitions in 3d crystals of colloidal superballs*. Nat. Commun., 8:14352, 2017.

- [61] U. Agarwal and F. A. Escobedo, *Mesophase behaviour of polyhedral particles*. Nat. Mater., 10(3):230, 2011.
- [62] P. F. Damasceno, M. Engel, and S. C. Glotzer, *Predictive self-assembly of polyhedra into complex structures*. Science, 337(6093):453–457, 2012.
- [63] M. Dijkstra, *Entropy-driven phase transitions in colloids: From spheres to anisotropic particles*. Adv. Chem. Phys., 156:35–71, 2014.
- [64] W. F. Paxton, K. C. Kistler, C. C. Olmeda, A. Sen, S. K. St. Angelo, Y. Cao, T. E. Mallouk, P. E. Lammert, and V. H. Crespi, *Catalytic nanomotors: autonomous movement of striped nanorods*. J. Am. Chem. Soc., 126(41):13424–13431, 2004.
- [65] R. Dreyfus, J. Baudry, M. L. Roper, M. Fermigier, H. A. Stone, and J. Bibette, *Microscopic artificial swimmers*. Nature, 437(7060):862–865, 2005.
- [66] J. R. Howse, R. A. L. Jones, A. J. Ryan, T. Gough, R. Vafabakhsh, and R. Golestanian, *Self-motile colloidal particles: from directed propulsion to random walk*. Phys. Rev. Lett., 99(4):048102, 2007.
- [67] I. Theurkauff, C. Cottin-Bizonne, J. Palacci, C. Ybert, and L. Bocquet, *Dynamic clustering in active colloidal suspensions with chemical signaling*. Phys. Rev. Lett., 108(26):268303, 2012.
- [68] I. Buttinoni, J. Bialké, F. Kümmel, H. Löwen, C. Bechinger, and T. Speck, *Dynamical clustering and phase separation in suspensions of self-propelled colloidal particles*. Phys. Rev. Lett., 110(23):238301, 2013.
- [69] J. Palacci, S. Sacanna, A. P. Steinberg, D. J. Pine, and P. M. Chaikin, *Living crystals of light-activated colloidal surfers*. Science, 339(6122):936–940, 2013.
- [70] Y. Fily and M. C. Marchetti, *Athermal phase separation of self-propelled particles with no alignment*. Phys. Rev. Lett., 108(23):235702, 2012.
- [71] J. Stenhammar, A. Tiribocchi, R. J. Allen, D. Marenduzzo, and M. E. Cates, *Continuum theory of phase separation kinetics for active Brownian particles*. Phys. Rev. Lett., 111(14):145702, 2013.
- [72] J. Stenhammar, D. Marenduzzo, R. J. Allen, and M. E. Cates, *Phase behaviour of active Brownian particles: the role of dimensionality*. Soft Matter, 10(10):1489–1499, 2014.
- [73] R. Wittkowski, A. Tiribocchi, J. Stenhammar, R. J. Allen, D. Marenduzzo, and M. E. Cates, *Scalar  $\varphi^4$  field theory for active-particle phase separation*. Nat. Commun., 5:4351, 2014.
- [74] J. Bialké, H. Löwen, and T. Speck, *Microscopic theory for the phase separation of self-propelled repulsive disks*. EPL, 103(3):30008, 2013.
- [75] G. S. Redner, M. F. Hagan, and A. Baskaran, *Structure and dynamics of a phase-separating active colloidal fluid*. Phys. Rev. Lett., 110(5):055701, 2013.
- [76] T. Speck, J. Bialké, A. M. Menzel, and H. Löwen, *Effective Cahn-Hilliard equation for the phase separation of active Brownian particles*. Phys. Rev. Lett., 112(21):218304, 2014.
- [77] Y. Fily, S. Henkes, and M. C. Marchetti, *Freezing and phase separation of self-propelled disks*. Soft Matter, 10(13):2132–2140, 2014.
- [78] A. P. Solon, J. Stenhammar, R. Wittkowski, M. Kardar, Y. Kafri, M. E. Cates, and J. Tailleur, *Pressure and phase equilibria in interacting active Brownian spheres*. Phys. Rev. Lett., 114(19):198301, 2015.

- [79] V. Narayan, S. Ramaswamy, and N. Menon, *Long-lived giant number fluctuations in a swarming granular nematic*. *Science*, 317(5834):105–108, 2007.
- [80] J. Deseigne, O. Dauchot, and H. Chaté, *Collective motion of vibrated polar disks*. *Phys. Rev. Lett.*, 105(9):098001, 2010.
- [81] V. Schaller, C. Weber, C. Semmrich, E. Frey, and A. R. Bausch, *Polar patterns of driven filaments*. *Nature*, 467(7311):73–77, 2010.
- [82] L. Baraban, M. Tasinkevych, M. N. Popescu, S. Sanchez, S. Dietrich, and O. G. Schmidt, *Transport of cargo by catalytic Janus micro-motors*. *Soft Matter*, 8(1):48–52, 2012.
- [83] N. Koumakis, A. Lepore, C. Maggi, and R. Di Leonardo, *Targeted delivery of colloids by swimming bacteria*. *Nat. Commun.*, 4:2588, 2013.
- [84] F. Martinez-Pedrero and P. Tierno, *Magnetic propulsion of self-assembled colloidal carpets: efficient cargo transport via a conveyor-belt effect*. *Phys. Rev. Appl.*, 3(5):051003, 2015.
- [85] L. Soler, V. Magdanz, V. M. Fomin, S. Sanchez, and O. G. Schmidt, *Self-propelled micro-motors for cleaning polluted water*. *ACS Nano*, 7(11):9611–9620, 2013.
- [86] F. C. Keber, E. Loiseau, T. Sanchez, S. J. DeCamp, L. Giomi, M. J. Bowick, M. C. Marchetti, Z. Dogic, and A. R. Bausch, *Topology and dynamics of active nematic vesicles*. *Science*, 345(6201):1135–1139, 2014.
- [87] D. Frenkel and B. Smit. *Understanding molecular simulation: from algorithms to applications*. Academic Press, California, 2002.
- [88] M. P. Allen and D. J. Tildesley. *Computer simulation of liquids*. Oxford University Press, Oxford, 1989.
- [89] P. Langevin, *Sur la théorie du mouvement brownien*. *Compt. Rendus*, 146:530–533, 1908.
- [90] D. J. Higham, *An algorithmic introduction to numerical simulation of stochastic differential equations*. *SIAM Rev.*, 43(3):525–546, 2001.
- [91] B. J. Alder and T. E. Wainwright, *Studies in molecular dynamics. I. General method*. *J. Chem. Phys.*, 31(2):459–466, 1959.
- [92] M. P. Allen, D. Frenkel, and J. Talbot, *Molecular dynamics simulation using hard particles*. *Comp. Phys. Rep.*, 9(6):301–353, 1989.
- [93] J. P. Hirth and J. Lothe. *Theory of dislocations*. Wiley, New York, 1982.
- [94] A. van Blaaderen and P. Wiltzius, *Real-space structure of colloidal hard-sphere glasses*. *Science*, 270(5239):1177–1179, 1995.
- [95] E. R. Weeks, J. C. Crocker, A. C. Levitt, A. Schofield, and D. A. Weitz, *Three-dimensional direct imaging of structural relaxation near the colloidal glass transition*. *Science*, 287(5453):627–631, 2000.
- [96] W. K. Kegel and A. van Blaaderen, *Direct observation of dynamical heterogeneities in colloidal hard-sphere suspensions*. *Science*, 287(5451):290–293, 2000.
- [97] U. Gasser, E. R. Weeks, A. Schofield, P. N. Pusey, and D. A. Weitz, *Real-space imaging of nucleation and growth in colloidal crystallization*. *Science*, 292(5515):258–262, 2001.
- [98] S. Auer and D. Frenkel, *Prediction of absolute crystal-nucleation rate in hard-sphere colloids*. *Nature*, 409(6823):1020–1023, 2001.
- [99] S. Auer and D. Frenkel, *Line tension controls wall-induced crystal nucleation in hard-sphere colloids*. *Phys. Rev. Lett.*, 91(1):015703, 2003.

- [100] A. Cacciuto, S. Auer, and D. Frenkel, *Onset of heterogeneous crystal nucleation in colloidal suspensions*. *Nature*, 428(6981):404–406, 2004.
- [101] V. W. A. de Villeneuve, D. Verboekend, R. P. A. Dullens, D. G. A. L. Aarts, W. K. Kegels, and H. N. W. Lekkerkerker, *Hard sphere crystal nucleation and growth near large spherical impurities*. *J. Phys. Condens. Matter*, 17(45):S3371, 2005.
- [102] E. Allahyarov, K. Sandomirski, S. U. Egelhaaf, and H. Löwen, *Crystallization seeds favour crystallization only during initial growth*. *Nat. Commun.*, 6:7110, 2015.
- [103] L. Fillion and M. Dijkstra, *Prediction of binary hard-sphere crystal structures*. *Phys. Rev. E*, 79(4):046714, 2009.
- [104] J. K. Kummerfeld, T. S. Hudson, and P. Harrowell, *The densest packing of AB binary hard-sphere homogeneous compounds across all size ratios*. *J. Phys. Chem. B*, 112(35):10773–10776, 2008.
- [105] P. I. O’Toole and T. S. Hudson, *New high-density packings of similarly sized binary spheres*. *J. Phys. Chem. C*, 115(39):19037–19040, 2011.
- [106] A. B. Hopkins, Y. Jiao, F. H. Stillinger, and S. Torquato, *Phase diagram and structural diversity of the densest binary sphere packings*. *Phys. Rev. Lett.*, 107(12):125501, 2011.
- [107] S. Pronk and D. Frenkel, *Point defects in hard-sphere crystals*. *J. Phys. Chem. B*, 105(28):6722–6727, 2001.
- [108] S. Pronk and D. Frenkel, *Large effect of polydispersity on defect concentrations in colloidal crystals*. *J. Chem. Phys.*, 120(14):6764–6768, 2004.
- [109] S. K. Kwak, Y. Cahyana, and J. K. Singh, *Characterization of mono-and divacancy in fcc and hcp hard-sphere crystals*. *J. Chem. Phys.*, 128(13):134514, 2008.
- [110] M. Mortazavifar and M. Oettel, *Thermal vacancies in close-packing solids*. *EPL*, 105(5):56005, 2014.
- [111] P. Schall, I. Cohen, D. A. Weitz, and F. Spaepen, *Visualization of dislocation dynamics in colloidal crystals*. *Science*, 305(5692):1944–1948, 2004.
- [112] P. Schall, I. Cohen, D. A. Weitz, and F. Spaepen, *Visualizing dislocation nucleation by indenting colloidal crystals*. *Nature*, 440(7082):319–323, 2006.
- [113] N. Y. C. Lin, M. Bierbaum, P. Schall, J. P. Sethna, and I. Cohen, *Measuring nonlinear stresses generated by defects in 3d colloidal crystals*. *Nat. Mater.*, 15(11):1172, 2016.
- [114] T. O. E. Skinner, D. G. A. L. Aarts, and R. P. A. Dullens, *Grain-boundary fluctuations in two-dimensional colloidal crystals*. *Phys. Rev. Lett.*, 105(16):168301, 2010.
- [115] E. Maire, E. Redston, M. P. Gulda, D. A. Weitz, and F. Spaepen, *Imaging grain boundary grooves in hard-sphere colloidal bicrystals*. *Phys. Rev. E*, 94(4):042604, 2016.
- [116] F. A. Lavergne, S. Diana, D. G. A. L. Aarts, and R. P. A. Dullens, *Equilibrium grain boundary segregation and clustering of impurities in colloidal polycrystalline monolayers*. *Langmuir*, 32(48):12716–12724, 2016.
- [117] C. H. Bennett and B. J. Alder, *Studies in molecular dynamics. IX. Vacancies in hard sphere crystals*. *J. Chem. Phys.*, 54(11):4796–4808, 1971.
- [118] W. Lechner and C. Dellago, *Defect interactions in two-dimensional colloidal crystals: vacancy and interstitial strings*. *Soft Matter*, 5(14):2752–2758, 2009.

- [119] W. Lechner, D. Polster, G. Maret, P. Keim, and C. Dellago, *Self-organized defect strings in two-dimensional crystals*. Phys. Rev. E, 88:060402, 2013.
- [120] C. Vega and E. G. Noya, *Revisiting the Frenkel-Ladd method to compute the free energy of solids: The Einstein molecule approach*. J. Chem. Phys., 127(15):154113, 2007.
- [121] M. Marechal, U. Zimmermann, and H. Löwen, *Freezing of parallel hard cubes with rounded edges*. J. Chem. Phys., 136(14):144506, 2012.
- [122] W. Lechner, F. Cinti, and G. Pupillo, *Tunable defect interactions and supersolidity in dipolar quantum gases on a lattice potential*. Phys. Rev. A, 92(5):053625, 2015.
- [123] W. Lechner, E. Schöll-Paschinger, and C. Dellago, *Displacement fields of point defects in two-dimensional colloidal crystals*. J. Phys. Condens. Matter, 20(40):404202, 2008.
- [124] W. Lechner and C. Dellago, *Point defects in two-dimensional colloidal crystals: simulation vs. elasticity theory*. Soft Matter, 5(3):646–659, 2008.
- [125] K. E. Jensen, D. Pennachio, D. Recht, D. A. Weitz, and F. Spaepen, *Rapid growth of large, defect-free colloidal crystals*. Soft Matter, 9(1):320–328, 2013.
- [126] T. Dasgupta, J. R. Edison, and M. Dijkstra, *Growth of defect-free colloidal hard-sphere crystals using colloidal epitaxy*. J. Chem. Phys., 146(7):074903, 2017.
- [127] A. Pertsinidis and X. S. Ling, *Diffusion of point defects in two-dimensional colloidal crystals*. Nature, 413(6852):147–150, 2001.
- [128] A. Pertsinidis and X. S. Ling, *Equilibrium configurations and energetics of point defects in two-dimensional colloidal crystals*. Phys. Rev. Lett., 87(9):098303, 2001.
- [129] A. Libal, C. Reichhardt, and C. J. O. Reichhardt, *Point-defect dynamics in two-dimensional colloidal crystals*. Phys. Rev. E, 75(1):011403, 2007.
- [130] W. Lechner, D. Polster, G. Maret, C. Dellago, and P. Keim, *Entropy and kinetics of point defects in two-dimensional dipolar crystals*. Phys. Rev. E, 91(3):032304, 2015.
- [131] W. Hume-Rothery. *The structures of alloys of iron: an elementary introduction*. Elsevier, Amsterdam, 2013.
- [132] J. Tauber, R. Higler, and J. Sprakel, *Anomalous dynamics of interstitial dopants in soft crystals*. Proc. Natl. Acad. Sci. U.S.A., 113(48):13660–13665, 2016.
- [133] R. Higler and J. Sprakel, *Doping colloidal bcc crystals-interstitial solids and meta-stable clusters*. Scientific Reports, 7(1):12634, 2017.
- [134] C. A. Wert, *Diffusion coefficient of C in  $\alpha$ -iron*. Phys. Rev., 79(4):601, 1950.
- [135] D. C. Rapaport, R. L. Blumberg, S. R. McKay, W. Christian, et al., *The art of molecular dynamics simulation*. Computers in Physics, 10(5):456–456, 1996.
- [136] C. A. M. J. Wert and C. Zener, *Interstitial atomic diffusion coefficients*. Phys. Rev., 76(8):1169, 1949.
- [137] M. Plischke and B. Bergersen. *Equilibrium statistical physics*. World Scientific Publishing Co Inc, Singapore, 1994.
- [138] H. A. Al-Chalabi and E. McLaughlin, *Mutual and self-diffusion in binary mixtures*. Mol. Phys., 19(5):703–715, 1970.
- [139] A.-P. Hynninen, L. Filion, and M. Dijkstra, *Stability of LS and LS<sub>2</sub> crystal structures in binary mixtures of hard and charged spheres*. J. Chem. Phys., 131(6):064902, 2009.

- [140] S. R. Ganagalla and S. N. Punnathanam, *Free energy barriers for homogeneous crystal nucleation in a eutectic system of binary hard spheres*. J. Chem. Phys., 138(17):174503, 2013.
- [141] T. Dasgupta and M. Dijkstra, *Towards the colloidal Laves phase from binary hard-sphere mixtures via sedimentation*. Soft Matter, 14(13):2465, 2018.
- [142] E. C. M. Vermolen, J. H. J. Thijssen, A. Moroz, M. Megens, and A. van Blaaderen, *Comparing photonic band structure calculation methods for diamond and pyrochlore crystals*. Opt. Express, 17(9):6952–6961, 2009.
- [143] J. M. Polson, E. Trizac, S. Pronk, and D. Frenkel, *Finite-size corrections to the free energies of crystalline solids*. J. Chem. Phys., 112(12):5339–5342, 2000.
- [144] R. J. Speedy, *Pressure and entropy of hard-sphere crystals*. J. Phys.: Condens. Matter, 10(20):4387, 1998.
- [145] F. Wang and D. P. Landau, *Efficient, multiple-range random walk algorithm to calculate the density of states*. Phys. Rev. Lett., 86(10):2050, 2001.
- [146] G. A. Mansoori, N. F. Carnahan, K. E. Starling, and T. W. Leland Jr, *Equilibrium thermodynamic properties of the mixture of hard spheres*. J. Chem. Phys., 54(4):1523–1525, 1971.
- [147] H. Mehrer. *Diffusion in solids: fundamentals, methods, materials, diffusion-controlled processes*. Springer, Berlin, 2007.
- [148] H. R. Paneth, *The mechanism of self-diffusion in alkali metals*. Phys. Rev., 80(4):708, 1950.
- [149] L. A. Zepeda-Ruiz, J. Rottler, S. Han, G. J. Ackland, R. Car, and D. J. Srolovitz, *Strongly non-Arrhenius self-interstitial diffusion in vanadium*. Phys. Rev. B, 70(6):060102, 2004.
- [150] P. M. Derlet, D. Nguyen-Manh, and S. L. Dudarev, *Multiscale modeling of crowdion and vacancy defects in body-centered-cubic transition metals*. Phys. Rev. B, 76(5):054107, 2007.
- [151] T. Kontorova and J. Frenkel, *On the theory of plastic deformation and twinning. II*. Zh. Eksp. Teor. Fiz., 8:1340–1348, 1938.
- [152] A. I. Landau, A. S. Kovalev, and A. D. Kondratyuk, *Model of interacting atomic chains and its application to the description of the crowdion in an anisotropic crystal*. Phys. Status Solidi B, 179(2):373, 1993.
- [153] A. S. Kovalev, A. D. Kondratyuk, A. M. Kosevich, and A. I. Landau, *Theoretical description of the crowdion in an anisotropic crystal based on the Frenkel-Kontorova model including an elastic three-dimensional medium*. Phys. Status Solidi B, 177(1):117, 1993.
- [154] O. M. Braun and Y. S. Kivshar, *Nonlinear dynamics of the Frenkel-Kontorova model*. Phys. Rep., 306(1-2):1–108, 1998.
- [155] S. L. Dudarev, *Coherent motion of interstitial defects in a crystalline material*. Philos. Mag., 83(31-34):3577–3597, 2003.
- [156] Y. Matsukawa and S. J. Zinkle, *One-dimensional fast migration of vacancy clusters in metals*. Science, 318(5852):959–962, 2007.
- [157] P. Bolhuis and D. Frenkel, *Tracing the phase boundaries of hard spherocylinders*. J. Chem. Phys., 106(2):666–687, 1997.
- [158] C. Vega and P. A. Monson, *Plastic crystal phases of hard dumbbells and hard spherocylinders*. J. Chem. Phys., 107(7):2696, 1997.

- [159] E. Zaccarelli, C. Valeriani, E. Sanz, W. C. K. Poon, M. E. Cates, and P. N. Pusey, *Crystallization of hard-sphere glasses*. Phys. Rev. Lett., 103(13):135704, 2009.
- [160] A. Haji-Akbari, M. Engel, A. S. Keys, X. Zheng, R. G. Petschek, P. Palfy-Muhoray, and S. C. Glotzer, *Disordered, quasicrystalline and crystalline phases of densely packed tetrahedra*. Nature, 462(7274):773, 2009.
- [161] A. L. Thorneywork, J. L. Abbott, D. G. A. L. Aarts, and R. P. A. Dullens, *Two-dimensional melting of colloidal hard spheres*. Phys. Rev. Lett., 118(15):158001, 2017.
- [162] F. A. Lavergne, D. G. A. L. Aarts, and R. P. A. Dullens, *Anomalous grain growth in a polycrystalline monolayer of colloidal hard spheres*. Phys. Rev. X, 7(4):041064, 2017.
- [163] S. Torquato and Y. Jiao, *Dense packings of polyhedra: Platonic and Archimedean solids*. Phys. Rev. E, 80(4):041104, 2009.
- [164] S. Torquato and Y. Jiao, *Dense packings of the Platonic and Archimedean solids*. Nature, 460(7257):876, 2009.
- [165] R. D. Batten, F. H. Stillinger, and S. Torquato, *Phase behavior of colloidal superballs: Shape interpolation from spheres to cubes*. Phys. Rev. E, 81(6):061105, 2010.
- [166] R. Ni, A. P. Gantapara, J. de Graaf, R. van Roij, and M. Dijkstra, *Phase diagram of colloidal hard superballs: from cubes via spheres to octahedra*. Soft Matter, 8(34):8826–8834, 2012.
- [167] S. Dussi and M. Dijkstra, *Entropy-driven formation of chiral nematic phases by computer simulations*. Nat. Commun., 7:11175, 2016.
- [168] N. Tasios and M. Dijkstra, *A simulation study on the phase behavior of hard rhombic platelets*. J. Chem. Phys., 146(14):144901, 2017.
- [169] F. Smallenburg, L. Filion, M. Marechal, and M. Dijkstra, *Vacancy-stabilized crystalline order in hard cubes*. Proc. Natl. Acad. Sci. U.S.A., 109(44):17886–17890, 2012.
- [170] A. P. Gantapara, J. de Graaf, R. van Roij, and M. Dijkstra, *Phase diagram and structural diversity of a family of truncated cubes: Degenerate close-packed structures and vacancy-rich states*. Phys. Rev. Lett., 111(1):015501, 2013.
- [171] R. van Damme, B. van der Meer, J. J. van den Broeke, F. Smallenburg, and L. Filion, *Phase and vacancy behaviour of hard “slanted” cubes*. J. Chem. Phys., 147(12):124501, 2017.
- [172] L. Hernández de la Peña, R. van Zon, J. Schofield, and S. B. Opps, *Discontinuous molecular dynamics for semiflexible and rigid bodies*. J. Chem. Phys., 126(7):074105, 2007.
- [173] A. Jain, J. R. Errington, and T. M. Truskett, *Inverse design of simple pairwise interactions with low-coordinated 3d lattice ground states*. Soft Matter, 9(14):3866, 2013.
- [174] A. Jain, J. R. Errington, and T. M. Truskett, *Communication: Phase behavior of materials with isotropic interactions designed by inverse strategies to favor diamond and simple cubic lattice ground states*. J. Chem. Phys., 139(14):141102, 2013.
- [175] S. Gokhale, K. H. Nagamanasa, R. Ganapathy, and A. K. Sood, *Grain growth and grain boundary dynamics in colloidal polycrystals*. Soft Matter, 9(29):6634–6644, 2013.
- [176] Y.-H. Ye, F. LeBlanc, A. Haché, and V.-V. Truong, *Self-assembling three-dimensional colloidal photonic crystal structure with high crystalline quality*. Appl. Phys. Lett., 78(1):52–54, 2001.

- [177] Z. Cheng, W. B. Russel, and P. M. Chaikin, *Controlled growth of hard-sphere colloidal crystals*. Nature, 401(6756):893–895, 1999.
- [178] A. van Blaaderen, R. Ruel, and P. Wiltzius, *Template-directed colloidal crystallization*. Nature, 385(6614):321–324, 1997.
- [179] K.-h. Lin, J. C. Crocker, V. Prasad, A. Schofield, D. A. Weitz, T. C. Lubensky, and A. G. Yodh, *Entropically driven colloidal crystallization on patterned surfaces*. Phys. Rev. Lett., 85(8):1770, 2000.
- [180] P. V. Braun, R. W. Zehner, C. A. White, M. K. Weldon, C. Kloc, S. S. Patel, and P. Wiltzius, *Epitaxial growth of high dielectric contrast three-dimensional photonic crystals*. Adv. Mater., 13(10):721–724, 2001.
- [181] M. Allard, E. H. Sargent, P. C. Lewis, and E. Kumacheva, *Colloidal crystals grown on patterned surfaces*. Adv. Mater., 16(15):1360–1364, 2004.
- [182] T. Palberg, W. Mönch, J. Schwarz, and P. Leiderer, *Grain size control in polycrystalline colloidal solids*. J. Chem. Phys., 102(12):5082–5087, 1995.
- [183] R. M. Amos, J. G. Rarity, P. R. Tapster, T. J. Shepherd, and S. C. Kitson, *Fabrication of large-area face-centered-cubic hard-sphere colloidal crystals by shear alignment*. Phys. Rev. E, 61(3):2929, 2000.
- [184] S. Gokhale, K. H. Nagamanasa, V. Santhosh, A. K. Sood, and R. Ganapathy, *Directional grain growth from anisotropic kinetic roughening of grain boundaries in sheared colloidal crystals*. Proc. Natl. Acad. Sci. U.S.A., 109(50):20314–20319, 2012.
- [185] A. Sokolov and I. S. Aranson, *Physical properties of collective motion in suspensions of bacteria*. Phys. Rev. Lett., 109(24):248109, 2012.
- [186] J. Schwarz-Linek, C. Valeriani, A. Cacciuto, M. E. Cates, D. Marenduzzo, A. N. Morozov, and W. C. K. Poon, *Phase separation and rotor self-assembly in active particle suspensions*. Proc. Natl. Acad. Sci. U.S.A., 109(11):4052–4057, 2012.
- [187] R. Ni, M. A. C. Stuart, M. Dijkstra, and P. G. Bolhuis, *Crystallizing hard-sphere glasses by doping with active particles*. Soft Matter, 10(35):6609–6613, 2014.
- [188] F. Kümmel, P. Shabestari, C. Lozano, G. Volpe, and C. Bechinger, *Formation, compression and surface melting of colloidal clusters by active particles*. Soft Matter, 11(31):6187–6191, 2015.
- [189] J. Stenhammar, R. Wittkowski, D. Marenduzzo, and M. E. Cates, *Activity-induced phase separation and self-assembly in mixtures of active and passive particles*. Phys. Rev. Lett., 114(1):018301, 2015.
- [190] P. G. Debenedetti. *Metastable liquids: concepts and principles*. Princeton University Press, Princeton, 1996.
- [191] K. Kelton and A. L. Greer. *Nucleation in condensed matter: applications in materials and biology*. Elsevier, Oxford, 2010.
- [192] C. Bechinger, R. Di Leonardo, H. Löwen, C. Reichhardt, G. Volpe, and G. Volpe, *Active particles in complex and crowded environments*. Rev. Mod. Phys., 88(4):045006, 2016.
- [193] A. Wysocki, R. G. Winkler, and G. Gompper, *Propagating interfaces in mixtures of active and passive Brownian particles*. New J. Phys., 18(12):123030, 2016.
- [194] V. L. Colvin, *From opals to optics: Colloidal photonic crystals*. MRS Bull., 26(08):637–641, 2001.

- [195] P. T. Korda and D. G. Grier, *Annealing thin colloidal crystals with optical gradient forces*. J. Chem. Phys., 114(17):7570–7573, 2001.
- [196] X. Sun, Y. Li, T. H. Zhang, Y.-q. Ma, and Z. Zhang, *Fabrication of large two-dimensional colloidal crystals via self-assembly in an attractive force gradient*. Langmuir, 29(24):7216–7220, 2013.
- [197] J. Schiøtz, T. Vegge, F. D. Di Tolla, and K. W. Jacobsen, *Atomic-scale simulations of the mechanical deformation of nanocrystalline metals*. Phys. Rev. B, 60(17):11971, 1999.
- [198] L. Filion, R. Ni, D. Frenkel, and M. Dijkstra, *Simulation of nucleation in almost hard-sphere colloids: The discrepancy between experiment and simulation persists*. J. Chem. Phys., 134(13):134901, 2011.
- [199] P.-R. Wolde et al., *Simulation of homogeneous crystal nucleation close to coexistence*. Farad. Discuss., 104:93–110, 1996.
- [200] J. Elgeti and G. Gompper, *Wall accumulation of self-propelled spheres*. EPL, 101(4):48003, 2013.
- [201] X. Yang, M. L. Manning, and M. C. Marchetti, *Aggregation and segregation of confined active particles*. Soft Matter, 10(34):6477–6484, 2014.
- [202] F. Romano, E. Sanz, and F. Sciortino, *Crystallization of tetrahedral patchy particles in silico*. J. Chem. Phys., 134(17):174502, 2011.
- [203] M. C. Marchetti, J. F. Joanny, S. Ramaswamy, T. B. Liverpool, J. Prost, M. Rao, and R. A. Simha, *Hydrodynamics of soft active matter*. Rev. Mod. Phys., 85(3):1143, 2013.
- [204] I. S. Aranson, *Active colloids*. Phys. Usp., 56(1):79, 2013.
- [205] J. Elgeti, R. G. Winkler, and G. Gompper, *Physics of microswimmers – single particle motion and collective behavior: a review*. Rep. Prog. Phys., 78(5):056601, 2015.
- [206] J. Bialké, T. Speck, and H. Löwen, *Active colloidal suspensions: Clustering and phase behavior*. J. Non-Cryst. Solids, 407:367–375, 2015.
- [207] M. E. Cates and J. Tailleur, *Motility-induced phase separation*. Annu. Rev. Condens. Matter Phys., 6(1):219–244, 2015.
- [208] C. Reichardt and C. J. O. Reichardt, *Active matter ratchets with an external drift*. Phys. Rev. E, 88(6):062310, 2013.
- [209] R. Di Leonardo, L. Angelani, D. Dell’Arciprete, G. Ruocco, V. Iebba, S. Schippa, M. P. Conte, F. Mecarini, F. De Angelis, and E. Di Fabrizio, *Bacterial ratchet motors*. Proc. Natl. Acad. Sci. U.S.A., 107(21):9541–9545, 2010.
- [210] V. Prymidis, H. Sielcken, and L. Filion, *Self-assembly of active attractive spheres*. Soft Matter, 11(21):4158–4166, 2015.
- [211] V. Prymidis, S. Paliwal, M. Dijkstra, and L. Filion, *Vapour-liquid coexistence of an active Lennard-Jones fluid*. J. Chem. Phys., 145(12):124904, 2016.
- [212] V. Prymidis, S. Samin, and L. Filion, *State behaviour and dynamics of self-propelled Brownian squares: a simulation study*. Soft Matter, 12(19):4309–4317, 2016.
- [213] B. Trefz, S. K. Das, S. A. Egorov, P. Virnau, and K. Binder, *Activity mediated phase separation: Can we understand phase behavior of the nonequilibrium problem from an equilibrium approach?* J. Chem. Phys., 144(14):144902, 2016.

- [214] S. C. Takatori and J. F. Brady, *Towards a thermodynamics of active matter*. Phys. Rev. E, 91:032117, 2015.
- [215] S. C. Takatori, W. Yan, and J. F. Brady, *Swim pressure: stress generation in active matter*. Phys. Rev. Lett., 113(2):028103, 2014.
- [216] A. P. Solon, Y. Fily, A. Baskaran, M. E. Cates, Y. Kafri, M. Kardar, and J. Tailleur, *Pressure is not a state function for generic active fluids*. Nat. Phys., 11:673, 2015.
- [217] J. Bialké, J. T. Siebert, H. Löwen, and T. Speck, *Negative interfacial tension in phase-separated active Brownian particles*. Phys. Rev. Lett., 115(9):098301, 2015.
- [218] G. Falasco, F. Baldovin, K. Kroy, and M. Baiesi, *Mesoscopic virial equation for nonequilibrium statistical mechanics*. New J. Phys., 18(9):093043, 2016.
- [219] T. Speck and R. L. Jack, *Ideal bulk pressure of active Brownian particles*. Phys. Rev. E, 93(6):062605, 2016.
- [220] R. G. Winkler, A. Wysocki, and G. Gompper, *Virial pressure in systems of spherical active Brownian particles*. Soft Matter, 11(33):6680–6691, 2015.
- [221] A. P. Solon, J. Stenhammar, M. E. Cates, Y. Kafri, and J. Tailleur, *Generalized thermodynamics of phase equilibria in scalar active matter*. Phys. Rev. E, 97(2):020602, 2018.
- [222] P. Krinninger, M. Schmidt, and J. M. Brader, *Nonequilibrium phase behavior from minimization of free power dissipation*. Phys. Rev. Lett., 117:208003, 2016.
- [223] J. Tailleur and M. E. Cates, *Statistical mechanics of interacting run-and-tumble bacteria*. Phys. Rev. Lett., 100(21):218103, 2008.
- [224] U. M. B. Marconi and C. Maggi, *Towards a statistical mechanical theory of active fluids*. Soft Matter, 11(45):8768–8781, 2015.
- [225] S. C. Takatori and J. F. Brady, *A theory for the phase behavior of mixtures of active particles*. Soft Matter, 11(40):7920–7931, 2015.
- [226] S. Paliwal, J. Rodenburg, R. van Roij, and M. Dijkstra, *Chemical potential in active systems: predicting phase equilibrium from bulk equations of state?* New J. Phys., 20(1):015003, 2018.
- [227] S. Paliwal, V. Prymidis, L. Filion, and M. Dijkstra, *Non-equilibrium surface tension of the vapour-liquid interface of active Lennard-Jones particles*. J. Chem. Phys., 147(8):084902, 2017.
- [228] T. Ikeshoji, B. Hafskjold, and H. Furuholt, *Molecular-level calculation scheme for pressure in inhomogeneous systems of flat and spherical layers*. Molecular Simulation, 29(2):101–109, 2003.
- [229] B. Smit, *Phase diagrams of Lennard-Jones fluids*. J. Chem. Phys., 96(11):8639–8640, 1992.
- [230] S. R. McCandlish, A. Baskaran, and M. F. Hagan, *Spontaneous segregation of self-propelled particles with different motilities*. Soft Matter, 8(8):2527–2534, 2012.

# Summary

Colloids are microscopic particles whose size ranges from a nanometer to several micrometers, that are dispersed in a solvent. One striking characteristic of colloidal systems is that their constituent particles are in a constant state of random motion due to incessant collisions with the fast-moving molecules of the solvent. This allows colloids to spontaneously explore all space available to them, and self-assemble, i.e. organize themselves, into a wide range of phases, such as gases, liquids, crystals, and even quasicrystals – just like atoms and molecules. Hence, to some extent colloids behave like “big atoms”.

In this thesis we focus on crystalline phases formed by colloids, often referred to as “colloidal crystals”, and in particular on their crystallographic defects. Specifically, we examine crystal defects in a wide variety of systems, ranging from the archetypical model system of hard spheres to hard cubes, to also mixtures of active and passive particles.

We start our investigation in Chapter 2 by studying vacancies and interstitials in the face-centered-cubic crystal phase of hard spheres. We locate these defects in the crystal and follow their motion over time, allowing us characterize their strain fields, interactions and dynamics. We show that the vacancy diffusion decreases rapidly as the density is increased, while the interstitial diffusion exhibits a much weaker density-dependence. To better understand this rapid slowing down of vacancy diffusion with increasing density, we calculate the free-energy barriers associated with vacancy hopping and find that the increasing height of the free-energy barrier is solely responsible for the slowing down of vacancy diffusion. The interactions between vacancies are shown to be weakly attractive and short-ranged, while the interactions between interstitials are found to be strongly attractive and are felt over long distances. As such, we find that vacancies do not form vacancy-clusters, while interstitials do form long-lived interstitial-clusters. Considering the strain field of vacancies and interstitials, we argue that vacancies hardly feel each other, as they do not substantially perturb the crystal, and as such exhibit weak interactions. Two interstitials, on the other hand, interact with each other over long distances, and start to interact (attractively) when their strain fields start to overlap.

In Chapter 3, we study the diffusion and interactions of interstitials in hard-sphere interstitial solid solutions. We calculate the free-energy barriers associated with interstitial diffusion for a range of size ratios and densities. For very small interstitials we find that the barrier height depends only on the density of the large particles, and does not depend on the stoichiometry. For interstitials of intermediate size ratio, we observe that for increasing stoichiometry the barrier height decreases. For large interstitials we observe a more intricate dependence of the barrier height on the stoichiometry, where the barrier transitions from decreasing to increasing in height with stoichiometry, as the large-sphere density is increased. One important open question we attempted to address is whether or not transition state theory can capture the interstitial dynamics in the hard-sphere model system. To test this, we apply classical transition state theory on the calculated free-energy barriers in order to predict the diffusion coefficients of interstitials, and obtained good agreement with diffusion coefficients as measured directly using event-driven molecular dynamics simulations. Hence our data suggests that transition

state theory can predict the interstitial dynamics correctly from the free-energy barriers for the hard-sphere model system. Additionally, we quantify the interactions between interstitials. Apart from excluded volume interactions when two interstitials occupy the same hole, we find these interactions to be almost ideal in our system. Lastly, we show that the interstitial diffusivity can be inferred from the large-particle fluctuations alone, thus providing an empirical relationship between the large-particle fluctuations and the interstitial diffusivity.

In Chapter 4, we have re-calculated the phase diagram for binary hard spheres with a size ratio of 0.82 by taking into consideration antisite defects in the  $\text{MgZn}_2$  Laves phase and substitutional defects in the face-centered-cubic crystals. The topology of this new phase diagram differs significantly from that of the phase diagram calculated previously where defects were not taken into account: while in the defect-free phase diagram, the Laves phase could only occur at its ideal composition, in the new phase diagram, the Laves phase covers a range of compositions, all of which are higher than its ideal composition at intermediate pressures. This correction arises from a significant concentration of antisite defects. In fact, we find stable regions where up to 2% of the large-particle lattice sites are occupied by a small particle. This defect concentration is orders of magnitude higher than the vacancy and interstitial defect concentrations found in monodisperse hard-sphere crystals.

Our data illustrate that the commonly made assumption in the calculation of phase diagrams, namely that the crystal composition is ideal, is not valid here. To date, these type of defects have not been considered in any of the binary hard-sphere phase behaviour studies, nor in any colloidal binary phase diagram studies that we are aware of. We also provide a more approximate method to take into account the effect of defects on the phase diagram. We show that this simple approach captures the essential traits of the “updated” phase diagram. Specifically, it predicts a similarly high concentration of defects. It also captures the atypical defect concentration that increased with pressure in the fluid-Laves region, as well as the pressure range over which the Laves phase is unstable at its ideal composition. The fact that the approximate phase diagram agrees well with our phase diagram suggests that this method would be an excellent starting point for future studies when it comes to correcting the phase diagrams which show regions of stability for other binary crystal structures.

Importantly, much of the research on the Laves phases in colloidal crystals has been motivated by the possibility of a complete band gap in the visible part of the spectrum, associated with the sublattices in the  $\text{MgCu}_2$  crystal. The high concentration of antisite defects we have found in the Laves phase with the  $\text{MgZn}_2$  structure, is also very likely to play an important role in the other, metastable Laves phases with the  $\text{MgCu}_2$  and  $\text{MgNi}_2$  structures. Hence, high defect concentrations may affect the photonic band gap of  $\text{MgCu}_2$ , as it is well known that already low concentrations of defects can deteriorate the performance of band-gap materials. As these defects are an inherent part of the crystal phase behavior, removing them may be a considerable challenge.

In Chapter 5, we explore the structure and dynamics of point defects in crystals of hard cubes and “slanted” cubes. The vacancies observed in these crystals clearly show strong similarities to crowdions in atomic systems, both in terms of structure, and in terms of their diffusive behavior. Specifically, their deformation fields closely follow the

Frenkel-Kontorova model, and their diffusion exhibits the behavior of a persistent random walk. Hence, we argue that these vacancies are a vacancy-analogue of crowdions.

Furthermore, our investigation has led to a number of other intriguing observations. First, the structure of the vacancies appears to be extremely robust to changes to the model system, in terms of packing fraction, defect concentration, and particle shape. Second, using an isotropic potential we show that hard flat faces are clearly not a requirement for the formation of delocalized vacancies. We hypothesize that delocalized vacancies are an inherent feature of simple cubic crystals of repulsive particles. Third, in contrast to the structure, the diffusion of the defects strongly depends on the packing fraction, but does so in an unexpected way: higher packing fractions lead to faster defect diffusion. Finally, we showed that the vacancies in our systems exhibit almost ideal interactions. Together with the method we introduced for pinning defects, this opens the door to a fast check on whether vacancies in a given system are capable of delocalizing: one can simply perform a simulation of a crystal with a single defect, and investigate its structure. We expect that this method will be helpful in the future in identifying whether defects may play an important role in determining the phase behavior.

In Chapter 6, we explore the doping of two-dimensional colloidal (poly)crystals with sparse active particles. We find that active particles enhance the mobility of grain boundaries, leading to large-scale single-domain crystals containing local defect clusters rich in active particles. Further analysis on single crystals revealed an intricate relation between the dynamics of active particles and the formation, and motion of defects in two-dimensional colloidal crystals. Not only do defects play a pivotal role in determining the mobility of active particles, they also generate attractions between active particles, which eventually drive the system to “phase separate” into mostly passive hexagonal crystal domains and complex defect clusters that are rich in active particles.

In Chapter 7, we explore whether active dopants can also speed up the removal of grain boundaries in *three dimensions*. In comparison to the two-dimensional case, particles in three-dimensional colloidal crystals are typically more strongly caged, because the coordination number is higher, and as a result the free-energy barriers involved in annealing out grain boundaries and other defects are expected to be significantly higher. Hence, it is interesting to determine whether active dopants can successfully overcome these higher barriers, and thus assist in coarsening a three-dimensional colloidal polycrystal. Our study demonstrates that, similar to the two-dimensional case, doping with sparse active particles provides an elegant new route to removing grain boundaries in three-dimensional colloidal polycrystals. We show that at sufficient self-propulsion, the system is driven into a crystal-fluid coexistence. In this case, active dopants become mobile and spontaneously gather at the grain boundaries. The resulting surface melting and recrystallization of domains is responsible for the motion of the grain boundaries and leads to the formation of a large single crystal. However, if the self-propulsion is too low to cause a phase separation, we observe no significant enhancement of grain growth.

Our studies presented in Chapters 6 and 7 demonstrates a novel avenue for removing grain boundaries - simply turning on and off the self-propulsion of the active particles. Hence by simply controlling the energy source for the active particles, via e.g. the availability of fuel or an external light source, active particles can be used to grow large-scale single-domain crystals. In both cases, we observe that the active particles are attracted

to the grain boundaries. This implies that the active particles autonomously find the location inside the sample where their active properties are most helpful. Therefore, the removal of grain boundaries via active doping is in contrast to more conventional methods based on external fields, which act uniformly on all the particles in the sample.

Finally, in Chapter 8 we address the question whether one can predict the phase behavior of active systems. Previous attempts at making such predictions either relied on an analytic definition of the chemical potential, free energy, or other thermodynamic quantities but led to only qualitative predictions of the phase diagram. Here, we attack the problem from a new angle, and try and address the possibility of chemical and mechanical equilibrium in these systems as directly as possible using computer simulations. Specifically, we take the existence of a mechanical pressure for torque-free spherical active particles as a starting point and introduce a numerical method to probe the possibility of chemical equilibrium in the system. Ideally, one would like to directly measure the chemical potential. However, currently we are unaware of an approximation-free method for numerically accessing the chemical potential. Instead, we develop a simulation method which lets us to measure a quantity which is analogous to the chemical potential in equilibrium systems, namely a reservoir density. In classical statistical physics the chemical potential arises when we connect a system to a particle reservoir. The chemical potential is then directly related to the density of the reservoir. Here, we copy this idea, and develop a simulation method that measures these reservoir densities instead of the chemical potential. We then explore the possibility of chemical and mechanical equilibrium in active systems by examining two different systems: an out-of-equilibrium mixture of passive and active attractive particles, and an active-active mixture of purely repulsive particles. In agreement with previous work we find mechanical equilibrium for the coexisting phases. More importantly, we show for the first time that the reservoirs of both species are characterized by the same density for coexisting phases. Finally, we show explicitly that the phase coexistence can be *predicted* quantitatively by measuring the pressure and the reservoir densities.

# Samenvatting

Colloïden zijn microscopisch kleine deeltjes met een grootte van tussen een nanometer en enkele micrometers die in een oplosmiddel gesuspendeerd zijn. Een opmerkelijke eigenschap van colloïdale systemen is dat de deeltjes in deze systemen voortdurend in beweging zijn door de botsingen die ze ondergaan met de moleculen van het oplosmiddel. Hierdoor kunnen colloïden zich zelfstandig organiseren in verschillende soorten fasen, bijvoorbeeld gassen, vloeistoffen, kristallen of zelfs quasi-kristallen – net als atomen en moleculen. Daarom kunnen colloïden tot op zekere hoogte beschouwd worden als “grote atomen”.

Het onderzoek in dit proefschrift richt zich op kristallen gevormd door colloïden, ook wel bekend als colloïdale kristallen, en de defecten die in deze kristallen voorkomen. We bestuderen deze defecten in verscheidene systemen, zoals het klassieke modelsysteem van harde bollen, maar ook systemen van harde kubussen en systemen die actieve deeltjes bevatten.

In Hoofdstuk 2 bestuderen we vacatures en interstitiëlen in de kubisch vlakgecentreerde kristalfase van harde bollen. We vinden de posities van deze defecten in het kristal en volgen hun beweging. Dit maakt het mogelijk om de diffusie en de interacties van de defecten te bestuderen. Ook kunnen we kijken naar de lokale vervormingen die deze defecten in het kristal veroorzaken. We laten zien dat de diffusie van vacatures snel afneemt naarmate de volumefractie toeneemt, terwijl de diffusie van interstitiëlen minder afhankelijk is van de volumefractie. Om beter te begrijpen waarom de diffusie van vacatures zo snel afneemt, berekenen we de vrije-energiebarrière voor het bewegen van een vacature van de ene roosterpositie naar een naburige roosterpositie. We laten zien dat de hoogte van deze vrije-energiebarrière de mate waarin vacatures diffunderen bepaalt. De interacties tussen de vacatures zijn attractief, maar zwak en hebben een korte dracht. De interacties tussen interstitiëlen zijn ook attractief, maar zijn sterk en worden gevoeld over veel langere afstanden. Hierdoor vormen vacatures geen clusters, terwijl interstitiëlen dat wel doen. Aan de hand van berekeningen van het verplaatsingsveld van deeltjes rondom de vacatures en interstitiëlen kunnen we deze interacties begrijpen. We laten namelijk zien dat vacatures het kristal nauwelijks verstoren en elkaar dus nauwelijks kunnen “voelen”, terwijl interstitiëlen juist grote verstoringen veroorzaken over lange afstanden, wat leidt tot sterke interacties.

In Hoofdstuk 3 bestuderen we de diffusie en interacties van interstitiëlen in interstitiële vaste oplossingen van harde bollen. We berekenen de vrije-energiebarrière voor diffusie van de interstitiëlen voor verschillende grootteverhoudingen en volumefracties. Voor kleine interstitiëlen is de vrije-energiebarrière onafhankelijk van de concentratie van de interstitiëlen. Voor middelgrote interstitiëlen zien we dat de hoogte van de vrije-energiebarrière afneemt wanneer de concentratie van de interstitiëlen toeneemt. Voor grote interstitiëlen zien we dat de vrije-energiebarrière een meer ingewikkelde afhankelijkheid van de concentratie van de interstitiëlen vertoont. Een belangrijke vraag die we hebben geprobeerd te beantwoorden is of de zogenoemde *theorie van de transitietoestand* de dynamica van de interstitiëlen kan beschrijven in deze systemen van harde bollen. Om dit te testen, hebben we deze klassieke theorie toegepast op de berekende vrije-energiebarrières om

hiermee de diffusiecoëfficiënt van de interstitiëlen te voorspellen. De door de theorie voorspelde diffusiecoëfficiënten zijn in goede overeenstemming met de diffusiecoëfficiënten die direct meetbaar zijn in moleculaire dynamica simulaties. Onze data tonen dus aan dat de theorie van de transitietoestand een goede beschrijving geeft voor de diffusie van interstitiëlen in het klassieke modelsysteem van harde bollen. Daarnaast hebben we ook gekeken naar de interacties tussen de interstitiëlen. We laten zien dat de interacties tussen de interstitiëlen bijna als ideaal beschouwd kunnen worden. Ten slotte laten we zien dat de diffusiecoëfficiënt van de interstitiëlen kan worden afgeschat aan de hand van de grootte van de fluctuaties die de grote deeltjes ondergaan.

In Hoofdstuk 4 hebben we het fasediagram van een binair mengsel van harde bollen met een grootteverhouding van 0.82 herberekend waarbij we verscheidene soorten defecten in ogenschouw hebben genomen, namelijk antipositie defecten in de  $\text{MgZn}_2$ -Lavesfase en substitutionele defecten in de kubisch vlakgecentreerde kristallen. Dit herberekende fasediagram verschilt substantieel van eerdere berekeningen waarin deze defecten zijn genegeerd. In het defectvrije fasediagram kon de Lavesfase alleen voorkomen met een ideale compositie, terwijl in het nieuwe fasediagram de Lavesfase voorkomt voor uiteenlopende composities die allemaal hoger zijn dan de ideale compositie. Deze correctie van het fasediagram wordt veroorzaakt door een hoge concentratie aan antipositie defecten in de Lavesfase, waarbij kleine deeltjes posities hebben ingenomen van grote deeltjes. We laten zien dat de Lavesfase stabiel is tot een maximale antipositie defectconcentratie van 2%. Deze defectconcentratie is veel hoger dan die van vacatures en interstitiëlen in kristallen van monodisperse harde bollen.

Onze data tonen aan dat een veelgemaakte aanname in de berekening van fasediagrammen, namelijk dat de compositie van het kristal ideaal is, in dit geval ongeldig is. Tot op heden zijn dit soort defecten niet meegenomen in berekeningen aan het fasegedrag van harde bollen of andere binaire mengsels van colloïden. We presenteren ook een eenvoudigere methode die het effect van defecten op het fasediagram goed benadert. We laten zien dat deze methode de belangrijkste kenmerken van het nieuwe fasediagram kan voorspellen, met als voornaamste kenmerk een vergelijkbaar hoge concentratie aan defecten. Deze eenvoudigere methode zou een goed uitgangspunt kunnen zijn voor het corrigeren van fasediagrammen van andere systemen waarvoor stabiele kristalstructuren voorspeld zijn.

Het onderzoek naar de Lavesfasen in colloïdale systemen is voornamelijk gemotiveerd door de mogelijkheid om een fotonische bandkloof in het zichtbare gedeelte van het spectrum te realiseren. De hoge defectconcentratie die we hebben aangetoond in de Lavesfase met de  $\text{MgZn}_2$ -structuur speelt zeer waarschijnlijk ook een belangrijke rol in de andere metastabiele Lavesfasen met de  $\text{MgCu}_2$ - en  $\text{MgNi}_2$ -structuren. Deze hoge defectconcentratie in de  $\text{MgCu}_2$ -Lavesfase zou de fotonische bandkloof kunnen aantasten, aangezien het bekend is dat lage defectconcentraties de prestaties van bandkloofmaterialen al kunnen verslechteren. Omdat deze defecten een inherente eigenschap van het kristal zijn, is het waarschijnlijk lastig om ze te verwijderen.

In Hoofdstuk 5 bestuderen we de structuur en dynamica van puntdefecten in kristallen van harde kubussen en “schuine kubussen”. De structuur en dynamica van de vacatures in deze kristallen vertonen sterke gelijkenissen met zogenoemde *crowdions* die in atomaire systemen voorkomen. Net als voor crowdions is het verplaatsingsveld van de deeltjes in

de vacatures in goede overeenstemming met het Frenkel-Kontorova model. Ook lijkt de diffusie van deze vacatures, die gekarakteriseerd wordt door langdurige glijbewegingen die zo nu en dan van richting veranderen door spontane heroriëntaties, op wat voor crowdions bekend is. Hiermee laten we zien dat de vacatures in onze systemen een vacature-analoog zijn van crowdions.

Daarnaast heeft ons onderzoek tot een aantal andere interessante observaties geleid. Ten eerste blijft de structuur van de vacatures vrijwel constant bij veranderingen in de volumefractie, defectconcentratie en de vorm van de deeltjes. Ten tweede laten we door middel van een systeem met een isotrope interactiepotentiaal zien dat deeltjes met platte vlakken geen vereiste zijn voor het vormen van gedelocaliseerde vacatures. Het is mogelijk dat gedelocaliseerde vacatures een inherente eigenschap zijn van kristallen met een primitief kubische kristalstructuur. Ten derde is, in tegenstelling tot hun structuur, de diffusie van de vacatures sterk afhankelijk van de volumefractie, maar op een onverwachte manier: hogere volumefracties leiden tot snellere diffusie. Ten slotte laten we zien dat interacties tussen de vacatures vrijwel als ideaal beschouwd kunnen worden. De methode die we presenteren om geïsoleerde vacatures te bestuderen, maakt het mogelijk om in de toekomst eenvoudigere simulaties te doen om te testen of vacatures in een ander willekeurig systeem kunnen delocaliseren. We verwachten dat dit nuttig zal zijn om een inschatting te maken of defecten een belangrijke rol spelen in het fasegedrag.

In Hoofdstuk 6 bestuderen we tweedimensionale (poly)kristallen waar kleine hoeveelheden actieve deeltjes aan zijn toegevoegd. We laten zien dat de actieve deeltjes de mobiliteit van de korrelgrenzen verhogen, hetgeen leidt tot de formatie van een enkel, groot kristaldomein. De actieve deeltjes en de defecten in het kristal vertonen interessante wisselwerkingen. Zo spelen defecten niet alleen een belangrijke rol in hoe snel de actieve deeltjes door het kristal kunnen bewegen, maar ook veroorzaken ze attracties tussen de actieve deeltjes waardoor het systeem een fasescheiding kan ondergaan.

In Hoofdstuk 7 bestuderen we of actieve deeltjes ook kunnen helpen bij het verwijderen van korrelgrenzen in driedimensionale kristallen. In vergelijking tot tweedimensionale kristallen hebben de deeltjes in driedimensionale kristallen een hoger coördinatiegetal en worden ze vaak sterker op hun plek gehouden door de omliggende deeltjes. Dit zorgt ervoor dat de vrije-energiebarrière voor het verwijderen van defecten in driedimensionale kristallen vaak hoger is. Het is daarom interessant om te bestuderen of de actieve deeltjes deze hogere barrières nog kunnen overkomen en kunnen helpen om korrelgrenzen te verwijderen. We laten zien dat actieve deeltjes ook in driedimensionale kristallen toegepast kunnen worden om grote kristaldomeinen te groeien. Wanneer de actieve deeltjes voldoende voorstuwingskracht hebben, leidt dit tot een kristal-vloeistofcoëxistentie. In dit geval worden de actieve deeltjes mobiel en verzamelen ze zich nabij de korrelgrenzen. Doordat de actieve deeltjes de kristaldomeinen aan het oppervlak continu laten smelten en herkristaliseren, vormt zich uiteindelijk een enkel, groot kristaldomein. Wanneer de actieve deeltjes echter onvoldoende voorstuwingskracht hebben, vindt er geen fasescheiding plaats en kunnen de actieve deeltjes niet bijdragen aan het groeien van grote kristaldomeinen.

De onderzoeken die in Hoofdstukken 6 en 7 beschreven staan, wijzen op een nieuwe methode om korrelgrenzen te verwijderen in colloïdale kristallen door middel van actieve deeltjes. In beide gevallen zien we dat actieve deeltjes worden aangetrokken tot de korrel-

grenzen. Dit houdt in dat de actieve deeltjes zelfstandig de weg vinden naar de plek in het systeem waar hun activiteit nuttig kan zijn. Dit is in tegenstelling tot meer conventionele methoden die gebruik maken van externe velden die op alle deeltjes in het systeem een uniforme werking hebben.

Ten slotte kijken we in Hoofdstuk 8 of het mogelijk is om het fasegedrag te voorspellen voor actieve systemen. Eerdere pogingen om zulke voorspellingen te maken, hebben gebruik gemaakt van een analytische definitie van de chemische potentiaal, de vrije-energie of een andere thermodynamische grootte, maar hebben alleen tot kwalitatieve overeenstemming geleid. In dit hoofdstuk pakken we het probleem op een nieuwe manier aan door de mogelijkheid van chemisch evenwicht en mechanisch evenwicht in deze systemen zo direct mogelijk te bestuderen. We ontwikkelen een numerieke methode die ons in staat stelt een grootte te meten die analoog is aan de chemische potentiaal voor systemen die in thermodynamisch evenwicht zijn. Dit doen we door een binaire fase te koppelen aan een deeltjesreservoir en de dichtheid aan deeltjes in dit reservoir te meten. In overeenstemming met eerder werk vinden we dat coëxistente fasen met elkaar in mechanisch evenwicht zijn, aangezien de druk gelijk is in coëxistente fasen. Belangrijker is dat we nu ook kunnen laten zien dat coëxistente fasen met elkaar in chemisch evenwicht zijn aangezien de deeltjesdichtheid in de reservoirs gelijk is voor coëxistente fasen. Ten slotte laten we zien dat we het fase-diagram accuraat kunnen voorspellen door te vereisen dat coëxistente fasen met elkaar in mechanisch evenwicht en chemisch evenwicht zijn.

# Acknowledgements

At the end of this thesis, I am happy to extend my thanks to all of you who have supported me, in some way or another, in completing my thesis. I am grateful to all of you, not only for helping me finish this thesis, but also for making my time in Utrecht more fun and satisfying.

First and foremost, I would like to thank Laura for her excellent guidance during these four years. It has been a pleasure to work with you. Thank you for all the hours you spent discussing scientific data, providing comments on my manuscripts, and discussing new ideas. I enjoyed the freedom you gave me in pursuing some of my own side projects. Thank you for always being so positive about that and for helping me turn those ideas into a successful project. Throughout these years I have really appreciated that your office door was always open to talk about science, but also about science-unrelated stuff. Thank you for being such a good and supportive supervisor – you were always there to keep me happy and motivated in my work. Of course, I would also like to thank my promotor. Marjolein, thank you for all your input, insights, and ideas. Thank you for your comments and corrections on my manuscripts and thesis chapters. It has been most interesting to be part of such a large group of simulators, and to get to learn so many different things about the field.

I would also like to thank Alfons van Blaaderen, Arnout Imhof, and René van Roij for many useful discussions. I have enjoyed the mix of simulations, experiments and theory very much. Alfons, thank you for your many comments on my presentations at the work discussion meetings, and for pointing out connections (or lack thereof) with experiments. René, thank you for the many insights, and always being so positive about the research that people are undertaking. I would also like to thank the other members of the scientific staff. Marijn van Huis, Freddy Rabouw, Patrick Baesjou, and Krassimir Velikov thank you for your valuable comments and questions during work discussion meetings. Peter Helfferich, thanks for helping me with my pc. Special thanks for replacing the power supply of my computer so quickly when it started to make terrifying noises. Marion, Hester and Dianne thank you for all the help with various forms.

During my PhD I have enjoyed collaborating with many different, talented people that I would like to thank. Special thanks to Frank Smalenburg. Thanks for having been involved in most of my projects. You have been a source of many excellent suggestions and original ideas. Also, thanks for getting me started with event-driven molecular dynamics simulations. Robin van Damme, I have enjoyed collaborating on the vacancies in systems of hard slanted cubes. Vasileios Prymidis, thank you for joining me on an ambitious project, and putting in so much time of your final months as a PhD. Jaco Geuchies and Daniël Vanmaekelbergh, thank you for involving us in a very intriguing project, where we could combine experiments and simulations. Thijs Besseling, thanks for useful discussions on long-ranged repulsive rods.

I would also like to thank my office mates. Tonnishtha, Ravi, Robin, Tom, and Sina thank you very much for a great atmosphere and providing me with the necessary distractions. I thank all former and current colleagues of the SCM group: Carmine, Emanuele,

Frankje, Maarten, Massi(miliano), Gabriele, Robin, Tonnishtha, Giulia, Albert, Somil, Douglas, Stijn, Jessi, Naveed, Chris, Rama(krishna), Pepijn, Srivatssan, Federico, Anna, Siddharth, Sina, Da, Ernest, Tom, Xiaobin, Dnyaneshwar, Xiaodan, Ajoy, Ravi, Yang, Tian-Song, John, Zdenek, Weikai, Wiebke, Guido, Henriëtte, Thijs, Simone, Nina, Anjan, Fabian, Marlous, Rik, Harini, Vasileios, Niko, Wessel, and Rao. Thank you all for contributing to such a nice environment.

I would also like to extend a special thanks to Joris Sprakel and Jasper van der Gucht with whom I had the pleasure of working with as a student. Thank you for getting me hooked on this colloidal playground, and for the great time I had doing my MSc thesis with you. This has motivated me very much to start a PhD.

De afgelopen vier jaar heb ik ook een nieuwe vrienden mogen ontmoeten in het schattige Odijk: Hans Rutger, Mirjam, Stefan, Judith, Marco, Martine, Henk en Karin bedankt voor jullie steun en de nodige afleiding. Aan mijn vrienden met wie ik al langere tijd mag optrekken: Arjon, Daphne, Tim/Wim, Marina, Henno en Mariëlle jullie ook hartelijk dank!

Graag wil ik mijn familie bedanken. Bedankt voor alles wat jullie in de afgelopen jaren voor ons betekend hebben. Ma en Henk, Pa en Jacqueline, Opa en Oma, Leendert en Anouk, Nieske en Arno: bedankt voor al jullie steun en interesse in mijn werk, ook als jullie het niet altijd even goed konden begrijpen. Leendert, jij in het bijzonder ook bedankt voor de vele uren aan nodige afleiding. Schoonfamilie, bedankt voor jullie gezelligheid. Jullie bereidheid om te helpen met de verhuizing en het klussen was hartverwarmend. In het bijzonder wil ik Jaap bedanken voor alle hulp met de vele klusjes in en rondom het huis, waar ik soms minder mee uit de voeten kon. Bedankt voor jullie steun, interesse en de vele leuke spelletjes die we mochten spelen.

Lieve Joanne, bedankt voor al je liefde en steun. In de afgelopen jaren heb jij alles rondom dit proefschrift van heel dichtbij mee mogen maken, zowel de leuke als de minder leuke dingen. Dankjewel voor je optimisme en ook voor het geduld dat je met me hebt gehad. Ik geniet van de vele mooie dagen met jou samen en ik kijk uit naar de toekomst die voor ons ligt.

## About the author

Berend van der Meer was born on February 17, 1991 in Veenendaal, the Netherlands. After graduating from secondary school in 2009, he started his studies at Wageningen University, where he enrolled in the Molecular Life Sciences program. For his master's degree he chose Physical Chemistry as his specialization. In 2014 he obtained his MSc degree *cum laude*. He did his MSc thesis in the Physical Chemistry and Soft Matter group at Wageningen University under the guidance of dr. Joris Sprakel and prof. Jasper van der Gucht. In this project, he studied excitations in colloidal crystals in experiments by means of optical tweezers. For his MSc internship he went to the Soft Condensed Matter group at Utrecht University where he worked under supervision of prof. Marjolein Dijkstra. Here, he studied the same problem as in his MSc thesis but now using computer simulations. For his combined work, featuring both experiments and simulations on the same topic, he received the KNCV (Royal Netherlands Chemical Society) Golden Master Award 2014, a Wageningen University Thesis Award 2014, and the Unilever Research Prize 2014. In September 2014 he started as a PhD candidate at the Soft Condensed Matter group of Utrecht University under the supervision of dr. Laura Filion. This thesis, entitled "Defects and Diffusion in Colloidal Crystals" is the result of his PhD project.

# List of Publications

This thesis is based on the following publications:

- B. van der Meer, M. Dijkstra, L. Filion, *Diffusion and interactions of point defects in hard-sphere crystals*, The Journal of Chemical Physics 146, 244905 (2017). Chapter 2.
- B. van der Meer, E. Lathouwers, F. Smalenburg, and L. Filion, *Diffusion and interactions of interstitials in hard-sphere interstitial solid solutions*, The Journal of Chemical Physics 147, 234903 (2017). Chapter 3.
- B. van der Meer, M. Dijkstra, F. Smalenburg, and L. Filion, *Antisite defects induce non-stoichiometry in the hard-sphere colloidal Laves phase*, manuscript to be submitted for publication. Chapter 4.
- B. van der Meer, R. van Damme, M. Dijkstra, F. Smalenburg, and L. Filion, *Revealing a vacancy analogue of the crowdion interstitial in simple cubic crystals*, manuscript submitted for publication. Chapter 5.
- B. van der Meer, L. Filion, and M. Dijkstra, *Fabricating large two-dimensional single colloidal crystals by doping with active particles*, Soft Matter 12, 3406 (2016). Chapter 6.
- B. van der Meer, M. Dijkstra, and L. Filion, *Removing grain boundaries from three-dimensional colloidal crystals using active dopants*, Soft Matter 12, 5630 (2016). Chapter 7.
- B. van der Meer/V. Prymidis, M. Dijkstra, and L. Filion, *Predicting phase behaviour of mixtures of active spherical particles*, manuscript to be submitted for publication. Chapter 8.

Other publications by the author:

- B. van der Meer, W. Qi, R. G. Fokkink, J. van der Gucht, M. Dijkstra, and J. Sprakel, *Highly cooperative stress relaxation in two-dimensional soft colloidal crystals*, Proceedings of the National Academy of Sciences 111 (43), 15356 (2014).
- B. van der Meer, W. Qi, J. Sprakel, L. Filion and M. Dijkstra, *Dynamical heterogeneities and defects in two-dimensional soft colloidal crystals*, Soft Matter 11, 9385 (2015).
- R. van Damme, B. van der Meer, J. J. van den Broeke, F. Smalenburg, and L. Filion, *Phase and vacancy behaviour of hard “slanted” cubes*, The Journal of Chemical Physics 147, 124501 (2017).

- 
- J. S. van der Burgt, J. J. Geuchies, B. van der Meer, H. Vanrompay, D. Zanaga, Y. Zhang, W. Albrecht, A. Petukhov, L. Filion, S. Bals, I. Swart, and D. Vanmaekelbergh, *Cuboidal Supraparticles Self-Assembled from Cubic CsPbBr<sub>3</sub> Perovskite Nanocrystals*, The Journal of Physical Chemistry C 122, 15706 (2018).